Mathematical and Experimental Analysis of Microbicide Vaginal Gels

BY

Vitaly Oleg Kheyfets

Submitted to the graduate degree program in Mechanical Engineering and the Graduate Faculty of the University of Kansas in partial fulfillment of the requirements for the degree of Doctor of Philosophy.

_____
Chairperson, Sarah L. Kieweg, Ph.D.

_____
Sara E. Wilson, Ph.D.

_____
Elizabeth A. Friis, Ph.D.

_____
Michael Detamore, Ph.D.

_____
Erik Van Vleck, Ph.D.

Date Defended: May 31st, 2011

The Thesis Committee for Vitaly Oleg Kheyfets
Certifies that this is the approved version of the following thesis:

Mathematical and Experimental Analysis of Microbicide Vaginal Gels

_____
Chairperson, Sarah L. Kieweg, Ph.D.

Date Approved: May 31st, 2011

Abstract

HIV is a growing concern worldwide. With slow progress in the development of a vaccine, researchers have turned to alternate methods of preventing the spreading of HIV as a result of unprotected sexual intercourse.

Developing a mechanism capable of protecting the vaginal or rectal epithelium from sexually transmitted pathogens can be an effective tool in the prevention of HIV infection. One such tool can come in the form of a microbicide gel, which provides a physical barrier and acts as a delivery vehicle for its active ingredient. In order for the microbicide to be an effective barrier and delivery vehicle, it must have the capability to coat the epithelium for a specific amount of time and sustain its structural integrity under the influence of gravity and other perturbation forces. In addition, to be used as a drug delivery vehicle the microbicide must serve the following functions: coat the surface completely without leaving any of the surface exposed, stay on the surface while influenced by external forces such as gravity and squeezing, and be able to contain potent concentrations of one or more active microbicidal ingredients.

Many currently available vaginal spermicidal gels are applied using a syringe-like applicator. After vaginal application, several physical forces will perturb the gel: gravity, squeezing, surface tension and shearing.

In this document I will outline the work that has been completed, for an original PhD dissertation, on the mathematical and experimental analysis of microbicide vaginal gels. This document contains an in-depth discussion of the methods taken to satisfy the following engineering goals:

1. An instrument/method for conducting gravity-induced flow experiments and obtaining spreading characteristics along with surface topography.
2. A numerical solution for a non-linear, second-order, partial differential equation that governs the evolution of the free surface of a spreading fluid.
3. A derivation and numerical solution for the 3-D power-law evolution equation.
4. A derivation and numerical solution for the 3-D Ellis evolution equation.

All experimental and computational simulations presented in this study involve a finite bolus of fluid, with non-Newtonian viscous properties, spreading on an inclined plane under the influence of gravity. Using the two numerical models presented in this document, I conducted an in-depth parameter and parameter sensitivity analysis of the power-law model, and a parameter study of the Ellis model. Combining the experimental data with computational simulations allowed me to make the following conclusions:

1. Accounting for lateral slumping in the computational simulation will improve the theory's agreement with experiment.
2. Approximating the initial condition to disregard complex curvatures on the free surface, and only consider gross geometric parameters, will not compromise theoretical model's agreement with experiment.
3. The 3-D power-law model provides a sufficient approximation of Hydroxyethylcellulose (HEC) spreading under the influence of gravity, for gels at 2.4-3.0% HEC concentration. Furthermore, implementing a constitutive equation that accounts for the low-shear Newtonian plateau (Ellis constitutive eq.) does not

improve the models agreement with experiment enough to justify its added complexity.

In conclusion, the following work provides an original experiment and a computational simulation of non-Newtonian fluid spreading. It is my hope that this work can be used by researchers in the field of microbicide development and any other scenario where free surface flow of non-Newtonian fluids is applicable.

Table of Contents

Table of Figures

Table of Tables

Table of Variables

Variable	Meaning	Units	Typical Value Used
α	Angle of inclination	rad	$\pi/6$
μ	Viscosity (Newtonian model)	Poise	500
ρ	Density	grams/cm^2	1
τ	Stress	Dyne/ cm^2	0 - 3000
g	Gravity	cm/s^2	980
$\dot{\gamma}$	Shear rate	1/s	0.1-100
m	Consistency index (power-law model)	Poise s^{n-1}	200-800
n	Shear thinning index (power-law model)	---	0.3-1.0
λ	Measure of shear thinning behavior (Ellis model)	---	1.0-3.0
η_0	Zero shear rate viscosity (Ellis model)	Poise	1000-3000
$\tau_{1/2}$	Stress at: $\eta=1/2\,\eta_0$ (Ellis model)	Dyne/ cm^2	100-500
$h(x,y,t)$	Height as a function of space and time	cm	0.1-1.0
h_i^n	Numerical approximation of height at a discretized point in space, i, and a specific time: n.	cm	0.1-1.0
h_{max}	Maximum height	cm	0.3-1.0
L_{front}	Length of bolus from trailing to leading edge, measured along axial axis	cm	2-100
L_{nose}	Length of bolus from trailing edge to location of maximum height, measure along axial axis	cm	1-80
W	Maximum width, measured along lateral axis	cm	2-50
H	Characteristics height	cm	0.5
x	Axial Dimension	cm	---
y	Lateral dimension	cm	---
Re	Reynold's number	---	
Bo	Bond Number – measure of acceleration of body forces to surface tension	---	38-220
$C.V.$	Coefficient of Variation – ratio of standard deviation to expected return	---	0-1.0
T	Temperature	°C	37.0
$[J]$	Jacobian Matrix	---	---
ε_{NEWT}	Error of Newton's method	---	$> 10^{-10}$
ε_{BiCG}	Error of BiConjugate Gradient method	---	$> 10^{-7}$
$\hat{i}$	Unit vector in the axial direction	---	1
$\hat{j}$	Unit vector in the lateral direction	---	1

$\tilde{v}$	Velocity vector: $\tilde{v} = u\hat{i} + v\hat{j}$	cm/s	1-10
dx	Axial dimension between numerical grid points	cm	0.01
dy	Lateral dimension between numerical grid points	cm	0.01
A_{L_f}	Area under L_{front} *vs. t* curve	cm s	180
A_s	Area under L_{front} *vs. t* curve if the curve trend was a straight line	cm s	$A_s < A_{L_f}$
ζ	Change-of-rate indicator	---	0-0.2

Table of Important Abbreviations

HEC	Hydroxyethylcellulose
HIV	Human immunodeficiency virus
STI	Sexually Transmitted Infection
BiCG	BiConjugate Gradient

Acknowledgements

I would like to thank my family for their love and support through this entire experience. During my time at the University of Kansas, my parents (Emilya and Oleg Kheyfets) acted as if they have more invested in my school and career than I do. They worried about every aspect of every issue I had and would summon any resource for help. My father and uncle (Joseph Kheyfets, Israel) spent endless hours on Skype discussing my academic prospects and complications. Every milestone and setback prompted an immediate international conference call, which would quickly result in practical and useful advice. My brother (Eugene Kheyfets) was an endless resource for anything ranging from proofreading papers to writing and debugging C code. He and his wife (Julia Kheyfets) would even listen to my extremely boring presentations to give me an opportunity to rehearse and get feedback. My uncle and grandparents (Anthony Khalemsky, Asia Khalemsky, and Yuli Khalemsky) never missed an opportunity to ask about my progress and offer words of encouragement and support. For all this, I give my warmest love and thanks to my entire mishpuhach!!!

Thank you to my advisor (Sarah L. Kieweg) for all of your time, effort, and encouragement. Thank you for the tons that I have learned from you over the past five years, and for your unconditional willingness to help. I would also like to thank my committee for their time, feedback, and support.

Thank you to my friends for their love and support, and being a crucial source of sanity during this crazy and fun experience. Thank you to Ilya Tabakh for endless hours of conversation on issues that specifically related to my work and overall advice on graduate school matters. Thank you for always making your assistance a phone call away. Thank you to Heather

Reynolds for spending much of your busy time on proofreading my projects and papers, and teaching me writing skills that I will use for the rest of my career.

I would also like to thank my lab group: B. Hu, M. Pacey, T.McDonald, T.Wilson, S.Karri, T.Balough for helpful discussions and advice. I would especially like to thank A.Markey for helping with calibrating thermocouples, preparing the calibration grid and building a box to contain the instrument's electronics.

This work was supported by NIH K12 HD052027, NIH R21 AI082697, and a KU New Faculty General Research Fund Award. V.O. Kheyfets was also supported by The Kansas Partnership for Graduate Fellows in K-12 Education NSF/GK NSF 07-555. Some of the computational resources were funded by NSF MRI 0821625.

INTRODUCTION: SUMMARY OF OBJECTIVES AND OUTCOMES

HIV is a growing concern in the scientific community and general populace all over the world. The research presented in this document will explain the work completed for an original Ph.D. dissertation. I hope that this document will aid in the development of microbicide delivery vehicles, which can be used to prevent the growing spread of HIV infection as a consequence of unprotected sex.

The document will cover an overview of HIV transmission (Ch 1), the development and rheological testing of hydroxyethylcellulose (HEC) gels (Ch 2), and carrying out objectives described in this introduction.

Developing a mechanism capable of protecting the vaginal or rectal epithelium from sexually transmitted pathogens can be an effective tool in the prevention of HIV infection. One such tool can come in the form of a cellulose-based gel, used to provide a physical barrier and act as a delivery vehicle for its active ingredient. Published findings of the Microbicide Development Strategy (MDS) have documented that vehicle design is a current priority gap [1]. In order for the microbicide to be an effective barrier and delivery vehicle it must have the capability to coat the epithelium for a specific amount of time and sustain its structural integrity under the influence of gravity and other perturbation forces [2]. In addition, to be used as a drug delivery vehicle the microbicide must serve the following functions: coat the surface completely without leaving any of the surface exposed, stay on the surface while influenced by external forces such as gravity and squeezing, and must be able to deliver potent concentrations of one or more active microbicidal ingredients.

The analytic hierarchy of this dissertation will be modeled using the system outlined in Figure I.

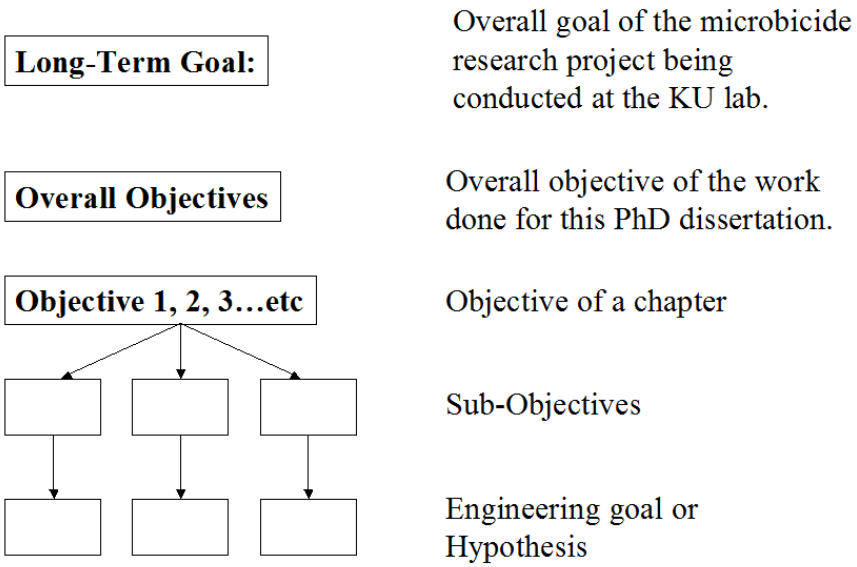

Figure I. Analytic Hierarchy of Dissertation

Our research group's long-term goal is to design a delivery vehicle, in the form of a gel, optimized to cover the vaginal epithelium. To achieve that goal, we need to better understand how a gel's rheological properties (i.e. viscosity, shear-thinning behavior) will govern spreading characteristics.

This work analyzes a finite bolus of gel applied to the epithelium of the vagina. After application, several physical forces will perturb the gel: gravity, squeezing and shearing. This dissertation will focus on the free surface coating flow of a shear-thinning polymeric liquid ("gel"), perturbed by gravity, analyzed in 3-D.

The overall objective of this work is:

(1) To design an instrument and technique for obtaining experimental flow characteristics along with surface topography of spreading gels.

(2) To develop a numerical model of a non-Newtonian fluid spreading, in 3-Dimensions, due to gravity.

The development of a 3-D power-law model is an advancement of a previous 2-D model [3, 4], which was used to simulate shear-thinning gels spreading under the influence of gravity. My motivation for developing a 3-D model was that when compared with an experiment, the 2-D model noticeably overestimated the flow in the axial direction.

The overall hypothesis for this work is that the following three changes will improve our existing numerical model's simulation of gravity-driven flow experiments:

1. **Use modeling in 3-Dimensions to account for axial and lateral spreading rather than the current 2-Dimensional power-law model, which does not account for lateral slumping.** This should improve the overshooting problem seen with the old numerical method because some of the mass will now be slumping in the lateral direction, resulting in less mass moving in the axial direction.
2. **Use the experimental initial condition, which accounts for local curvatures of the free surface, as input into the numerical model rather than a 4^{th} order approximation that includes only bulk geometry dimensions.** The spreading evolution of the free surface is governed by the local contours of the free surface. Therefore, accounting for the local contours of the experimental initial condition in the numerical simulation should improve spreading agreement, between numerical model and experiment, compared with an initial condition that only matches the experiment in maximum height, length, and width (bulk dimensions).
3. **Use an improved constitutive equation (Ellis) to account for low-shear rate shear-thinning behavior, not well described by the current power-law model.**

A constitutive equation that can accurately describe viscous forces at low shear rates should result in a better correlation with experiment, because during spreading some regions of the flow are exposed to very low shear rates.

The overall objectives of this work were accomplished by sequentially completing the following objectives that are specific to this dissertation:

<u>OBJECTIVE 1 (Chapter 3):</u> Develop an instrument and a technique for performing spreading tests with the ability to:

1. **Simulate humidity and temperature of *in vivo* environment.**
2. **Release a finite volume bolus of gel that is not in contact with anything other than the spreading surface (contact-free).**
3. **Map the topography of the initial condition of the sample to be used as the initial condition for the numerical simulation.**
4. **Measure sample spreading characteristics as a function of time.**

This instrument will provide useful data for spreading characteristics of different gels, with different concentrations of HEC, as well as validate the numerical simulation.

The <u>engineering goal</u> of this objective is to introduce a new instrument and method for releasing a "contact-free" spreading sample, measuring free surface topography, and obtaining spreading characteristics of a bolus of fluid.

<u>Outcome:</u> In Chapter 3, I will present an instrument and original technique for conducting gravity-induced flow experiments, and non-invasively obtaining spreading characteristics and surface topography as a function of time.

OBJECTIVE 2 (Chapter 4): Develop a 3-D numerical model to simulate the free surface, gravity-induced spreading of a thin film of Newtonian fluid.

The engineering goal of this objective is to develop an original code for solving a non-linear, second order PDE, in 3-D, that governs the free surface of a viscous, gravity-driven flow of a finite volume. This numerical simulation should: (1) show mesh convergence in axial and lateral direction; (2) conserve volume within 0.0001%; (3) be easy to upgrade for other PDEs that account for non-Newtonian behavior.

Outcome: In Chapter 4, I will present a numerical code capable of solving PDE's that govern free surface flow of a Newtonian fluid perturbed by gravity, in 3-D. This method is robust and can be upgraded to account for additional driving forces (e.g. surface tension, intermolecular).

OBJECTIVE 3 (Chapter 5): Incorporate the power-law constitutive equation into the 3-D numerical model developed in Objective 2.

The first hypothesis of this objective is that upgrading the 2-D numerical method (currently used to simulate power-law flow) to a 3-D method will result in better agreement with experimentally measured spreading characteristics (from Objective 1). The second hypothesis of this objective is that, when compared with code using an approximation of the initial condition that does not include specific gradients of the free surface, the actual experimental initial condition inserted in the computational code will result in better agreement between the numerical and experimental spreading characteristics.

Sub-Objective 3.1: Derive an evolution equation in 3-D using the power-law constitutive equation, and incorporate it into the numerical method developed in Objective 2.

The engineering goals of this sub-objective are to derive a 3-D evolution equation with power-law parameters that includes axial and lateral fluxes, and solve it numerically using the method developed in Objective 2.

Outcome: In Chapter 5, I will show the derivation of a second-order, non-linear PDE that governs the 3-D free surface flow of a two-parameter power-law fluid. I will present the methods used for discretizing the power-law evolution equation to ensure mass conservation.

Sub-Objective 3.2: Perform 2-D and 3-D numerical simulation for 2.4%, 2.7% and 3.0% HEC gels using the 3-D power-law code with rheological parameters (obtained by fitting to the viscometric data) and the experimental initial conditions obtained in Objective 1. For the 2-D numerical simulation, the initial condition will be a cut along the midpoint of the lateral axis of the experimental initial condition.

The hypothesis of this sub-objective is that the 3-D power-law code will match the spreading of the experiment better than the old 2-D power-law code.

Outcome: In Chapter 5, I will show that the 2-D numerical model noticeably overestimates axial spreading when compared with experiment. The 3-D model corrected this overestimation by diffusing some mass laterally.

Sub-Objective 3.3: Perform numerical simulation for 2.4%, 2.7% and 3.0% HEC gels using the 3-D power-law code with rheological parameters obtained by fitting to the viscometric data using: (1) the experimental initial condition (obtained from Objective 1) and (2) a 4^{th} order approximation of the initial condition that matches the maximum width, length and height of the experimental initial condition.

The hypothesis of this sub-objective is that the code with experimental initial conditions will match the experiment better than approximate initial condition. The engineering goal is to determine if variations of local surface gradients at the onset of flow, where shear rates are highest, will substantially impact flow dynamics.

Outcome: In Chapter 5, I will show that an approximation of the free surface, which entails the general physical dimensions of the experiment, is capable of simulating the experiment as well as using a detailed surface topography for the initial condition that encompasses a better approximation of the local surface contours.

Sub-Objective 3.4: Perform a rigorous power-law parameter sensitivity analysis, and document the effect of rheological parameters on axial spreading.

The engineering goal of this sub-objective is to perform a parameter study and a sensitivity analysis of the power-law numerical model and provide a framework for predicting how changes to the power-law parameters would impact axial spreading.

Outcome: In Chapter 5, I will present a complete sensitivity analysis of the power-law parameters and their impact on axial spreading and axial spreading rate.

Outcome of Objective 3: The overall conclusion of Chapter 5 shows that it is important to account for lateral spreading in a numerical simulation, and that mapping the exact local

contours of the initial condition does not particularly aid in agreement between computational analysis and experimental results.

OBJECTIVE 4: Incorporate the Ellis constitutive equation into the 3-D numerical model developed in Objective 2.

The hypothesis of this objective is that a 3-D numerical model (using exact IC) with an Ellis constitutive equation will match the experiment closer than the power-law model. Completing this objective will also result in a sensitivity analysis that reveals how the three Ellis parameters impact axial spreading.

Sub-Objective 4.1: Derive an evolution equation, in 3-D, using the Ellis constitutive equation and incorporate it into the numerical method developed in Objective 2.

The engineering goals of this sub-objective are to derive an evolution equation with Ellis parameters that includes axial and lateral fluxes, and solve it numerically using the method developed in Objective 2.

Outcome: In Chapter 6, I will show the derivation of a second-order, non-linear PDE that governs the 3-D free surface flow of a three-parameter Ellis fluid. I will present the methods used for discretizing the Ellis evolution equation to ensure mass conservation.

Sub-Objective 4.2: Perform numerical simulation for 2.4%, 2.7% and 3.0% HEC gels using the 3-D power-law and Ellis code (using exact IC) with rheological parameters obtained by fitting to the viscometric data, and compare the spreading characteristics of each simulation with its experimental counterpart.

The hypothesis of this sub-objective is that the Ellis numerical model will spread more like the experiment than the 3-D power-law numerical model due to the fact that the Ellis constitutive equations accounts for the Newtonian viscosity plateau at low shear rates.

The engineering goal is to determine if it is more beneficial to perform computational simulations of HEC spreading using the Ellis constitutive equation.

Outcome: In Chapter 6, I will show that the Ellis simulation equation does not pose considerable advantages over the power-law simulations, and are probably not worth implementing for microbicide application.

Sub-Objective 4.3: Perform a rigorous Ellis parameter sensitivity analysis and document the impact of rheological parameters and axial spreading.

The engineering goal of this sub-objective is to perform a parameter study of the Ellis numerical model and provide a framework for predicting how changes to the three Ellis parameters would impact axial spreading, which could be useful for numerous applications in addition to microbicides.

Outcome: In Chapter 6, I will present a complete sensitivity analysis of the Ellis parameters and their impact on axial spreading and axial spreading rate.

Outcome of Objective 4: The overall conclusion of Chapter 6 shows that using the Ellis constitutive equation results in modest advantages over the power-law constitutive equation when compared with experimental spreading of HEC gels.

Chapter 1 HIV TRANSMISSION AND MICROBICIDES

Overview of HIV infections

According to the UNAIDS Global report, it is estimated that in 2010 approximately 33.3 million people were living with HIV worldwide [5]. The rate of infection increases the number of sick patients by about 5 million per year [6]. A lot of current research is focused on decreasing the rate of spreading by testing techniques that prevent infection and making the infected less contagious.

Post-infection therapy using antiviral medication can improve the life expectancy of the patient and decrease the chances of transmitting the virus by reducing the genital secretion of HIV in infected patients [7]. Nevertheless, post-infection therapy is not currently capable of ridding the patient of the virus and is not a viable solution for preventing undiagnosed hosts from spreading the infection. Preventative measures, which range from improving awareness and teaching abstinence to free condom distributions, have proved to be disappointing [7, 8]. Also, after decades of grueling research, there is still no vaccine that can give uninfected people immunity to the HIV virus [6-10]. This lack of progress forces the scientific community to constantly re-evaluate realistic choices for treatment and prevention.

A significant portion of new infections is a result of unprotected sex. Emerging research has repeatedly confirmed that women are more vulnerable to infection than men during intercourse because of anatomical factors. In sub-Saharan Africa the effect that this epidemic is having on women is disproportionate, accounting for 60% of HIV cases [5]. It is widely

believed that this imbalance is a result of gender inequality and socioeconomic status, where in many cases of intercourse women are subjected to violence and are unable to negotiate condom use [5, 9].

Relative Anatomy and HIV transmission

The vagina is a muscular passage that is connected to the cervix. It is tubular with an H cross-section. It is surrounded with a rich matrix of blood vessels, which regulate moisture and pH. The multi-layered squamous epithelium, which does not have the necessary mechanisms to be infected, acts as a barrier to the lamina propria, which contain the primary sites of infection: (1) lymphoid cells, (2) dendritic cells, and (3) macrophages [7]. All of these cells have the CD4 receptor along with either the CCR5 or CXCR4 co-receptor, necessary for infection to occur [6, 7]. Infected dendritic cells can travel to the local lymph nodes where the virus will begin aggressive replication.

Intra-epithelial T-cells and Langerhans cells that can position themselves in the epithelial lining might have surfaces that extend into the mucosal lumen and act as transports for HIV. Once internalized, they can serve as a host for the virus or simply a transport mechanism like a bridge [6, 7, 9].

Vaginally transmitted HIV can also occur through cervical routes [6]. The cervix is a single layer of endocervical columnar epithelial cells usually coated with mucus containing antiviral proteins [6, 9]. The intact endocervix can usually block both the cell-associated and cell-free HIV from internalizing, but remains vulnerable to disruption. Moreover, it remains inconclusive if the ectocervix is more susceptible, but a condition that results in the ectocervix

being exposed beyond the mucus plug (cervical ectopy) has been shown to increase susceptibly to HIV transmission [6].

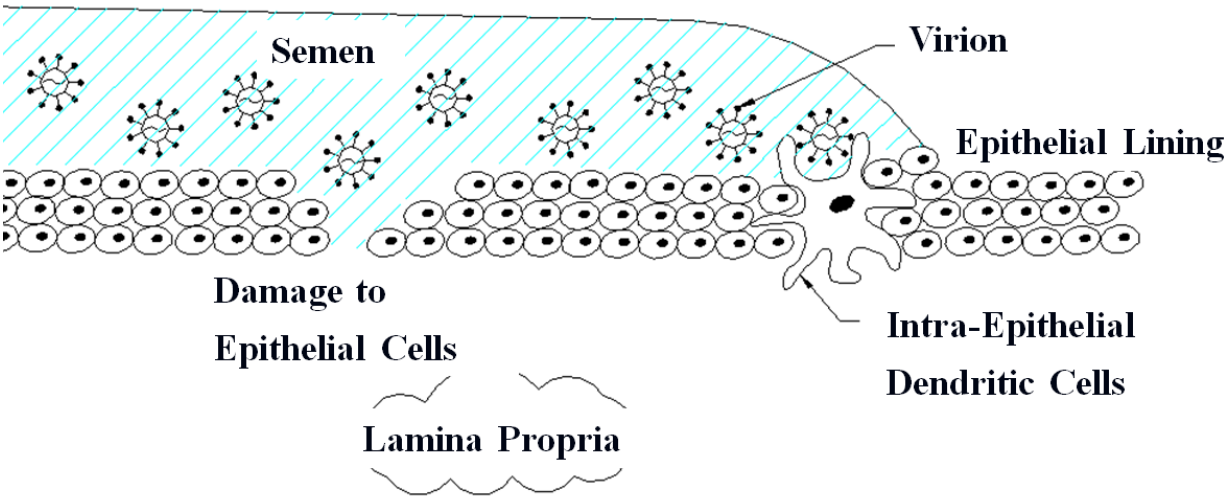

Figure 1.1. Diagram of vaginal epithelium subjected to semen infected with HIV.

During intercourse, semen infected with HIV (leukocytes infected with HIV and cell-free HIV [6]) comes into contact with the epithelial tissue inside the vaginal lumen. Any virion that penetrates the epithelial lining into the lamina propria is free to proliferate and cause the recipient to become infected. The epithelial wall is normally a sufficient barrier to infection, however any disruption to the epithelial walls can increase the risk of virions transmitting the mucosa [7]. Disruptions to the epithelial lining can appear as traumatic breaches or lesions caused by dry or traumatic sex, or occur as a result of pathological conditions such as other sexually transmitted infections [6].

Microbicides

A microbicide is a topical formulation that consists of a pharmaceutical agent suspended in a delivery vehicle (e.g. a polymeric liquid “gel”). The pharmaceutical agent will most likely

serve one of the following purposes: (1) damage the lipid membrane of the pathogen [7, 8], (2) inhibit cell entry by receptor deactivation [6, 8] by means such as charge manipulation, (3) inhibit target viral structures [6, 8], and (4) prevent dendritic cell uptake [8]. The delivery vehicle can come in the form of a gel or foam (from this point on a microbicide formulation will be referred to as a microbicide gel). The vehicle itself can act as a physical barrier and if developed to meet specific conditions might eliminate the need for a pharmaceutical agent all-together. In fact, a vehicle's ability to coat the epithelium has been singled out as a crucial variable, which might dictate the microbicides efficacy [11]. Vehicles can be designed to serve as a bioadhesive lubrication agent and regulate, or be controlled by, pH [8].

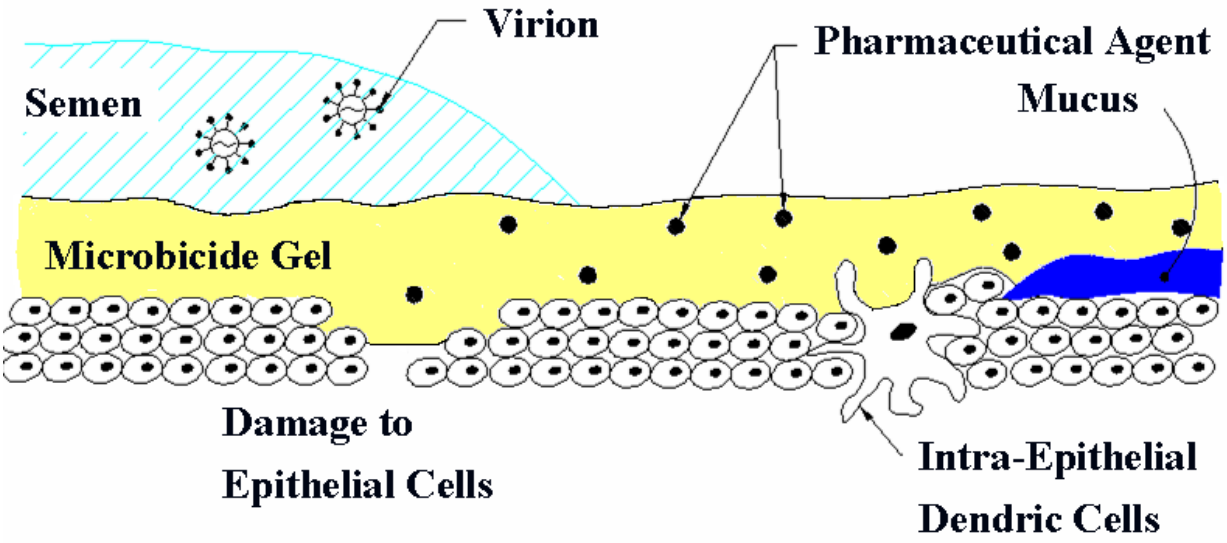

Figure 1.2. An image showing a microbicide gel protecting the surface of the epithelium.

Delivery

There are several options when considering methods of applying microbicide gels to the vaginal epithelium. The method we consider in this paper is application using a plunger that is inserted near the posterior fornix of the vagina (Figure 1.3). After application, the gel might

come into contact with anterior and posterior walls, especially after the plunger is removed and the vagina relaxes to the un-distended conformation [2].

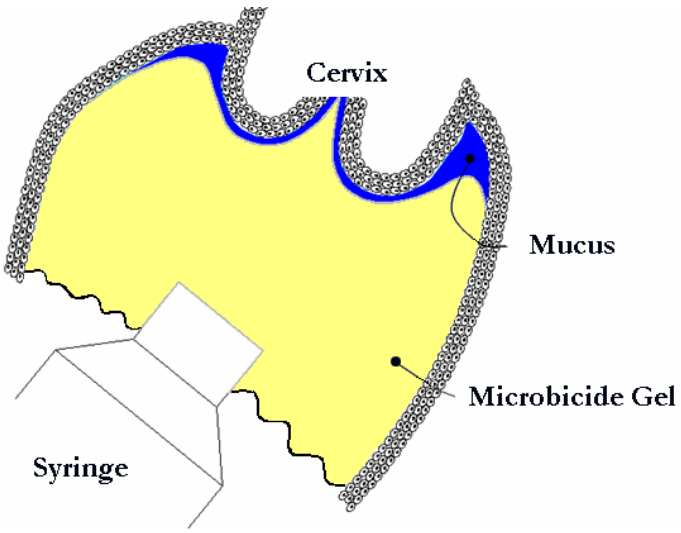

Figure 1.3. Example of microbicide gel being applied, using a syringe, directly below the cervix.

After application, the gel will be subjected to three main perturbation forces: (1) gravity, (2) shear, and (3) squeeze [2] (Figure 1.4). The idea behind the remainder of this dissertation is to model the gravity-induced perturbation acting on the gel. A final master model will have to account for all three perturbation forces.

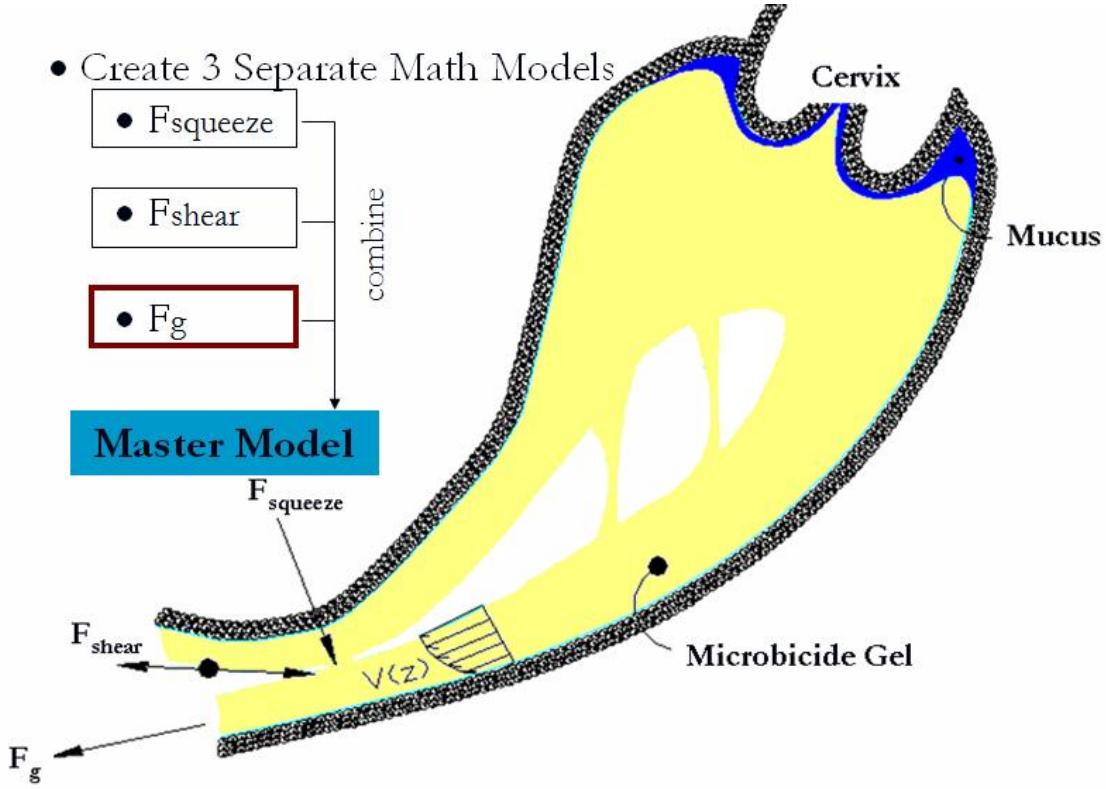

Figure 1.4. Likely evolution of the gel after delivery. The gel will be exposed to three perturbation forces: (1) squeezing, (2) shear, and (3) gravity.

Chapter 2 PREPARATION AND RHEOLOGY OF GELS

Introduction

A microbicide is a topical formulation that consists of a pharmaceutical agent suspended in a delivery vehicle. The microbicide delivery vehicle can come in the form of a gel, foam, cream, or any other applicable material [2]. The delivery vehicle should coat the entire epithelium under the perturbation of physical forces, such as gravity, squeezing and shearing. No specific type of vehicle has been singled out or excluded, but polymeric liquids, referred to by the pharmaceutical and microbicide community as "gels", seem to present clear advantages when considering the application in question. To confirm distribution and retention [12], magnetic-resonance imaging has shown that gels can be retained in the vagina for many hours [7, 13]. In addition, the only formulations that ever advanced to Phase III trials, as current microbicide candidates, were gels intended to be vaginally delivered before intercourse [8, 14, 15]. A formulation with a hydroxyethylcellulose (HEC) thickening agent, which is a linear polymer with no net charge or antiviral properties, has been implemented as a universal placebo for clinical trials [16].

In 2004, Kieweg *et al.* compared the spreading characteristics of different commercially available vaginal gels being perturbed by gravity [2]. Because cellulose gels don't have a yield stress, they are able to freely deform under the influence of gravity making them ideal for researching the correlation of spreading characteristics with certain non-Newtonian properties.

As a result of all these factors I have decided to focus my research on the spreading characteristics of a hydroxyethylcellulose gels and the constitutive equations that might be used to represent their shear-thinning behavior.

Cellulose

Cellulose is a tough, water-insoluble polysaccharide polymer, found in the protective cell walls of plants, with repeating units of β-glucose monosaccharide molecules [17, 18]. Cellulose can be chemically transformed for a variety of applications such as fabric detergent and solution thickener.

A specific ether of cellulose is hydroxyethylcellulose [19]. The addition of hydroxyethyl side chains makes this large molecule water-soluble (Figure 1). When added to water, this cellulose derivative becomes stiff under the influence of van der Waals forces and hydrogen bonding [19].

Water or PBS solution mixed with a hydroxyethylcellulose powder results in a non-Newtonian monopolymeric system (HEC "Gel"). Cellulose gels are rheologically characterized as shear-thinning fluids [2], meaning that the effective viscosity of the solution is decreased as the shear rate is increased. Cellulose gels, along with most other polymeric liquids that don't have a yield stress, generally abide by the following viscosity regimes when shear stress is applied: at some low and high shear rates they behave as Newtonian fluids, but somewhere in the middle the stress vs. strain-rate relationship becomes non-linear and can be represented using a power-law [20].

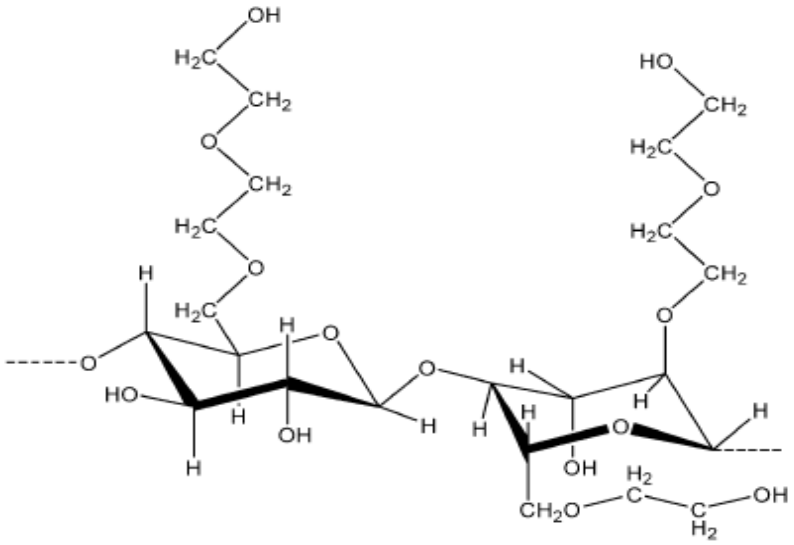

Figure 2.1. Structure of a repeating unit of hydroxyethylcellulose molecule [19]. Branches show hydroxyethyl side chains, which make the molecule water soluble.

Dynamic (oscillatory) rheological analysis has revealed that HEC gels store more elastic energy as the polymeric concentration is increased [21, 22]. Andrews *et al.* [23] found that for HEC concentrations of 2.4-4.8% (w/w), the storage modulus (G') might slightly exceed the loss modulus (G'') indicating solid-like behavior. For my research I will focus on the viscous behavior of the solution as the preliminary step to modeling the dynamics of this monopolymeric system in full. I feel that this simplification is not very impractical because, for my application, the concentrations that I am working with are in the lower spectrum of the "elastic" range that Andrews *et al.* specified. In addition, Andrews *et al.* found that strong elastic behaviors mostly occurred at high oscillation frequencies, but because my application deals with a very low rate of flow, I feel that the reasoning, for only considering the viscous behavior, is only affirmed. Dynamic oscillation data collected by Taylor Wilson at the University of Kansas, Biofluids Laboratory, confirms that a gel with 3.0% HEC concentration will adopt "solid-like" properties

at approximately 0.5 Hz of oscillation. This frequency will increase for gels with lower concentrations of HEC. This further reinforces that the HEC gels in question do not have a strong elastic component, especially within the scope of my application.

In conclusion, the mathematical models that will be presented in later chapters are not limited by the constitutive equations; therefore it might be possible to upgrade their capabilities to account for elastic behavior, but probably won't be necessary.

Constitutive Equations to Model HEC

To model the rheological behavior of HEC gels I start with the Newtonian expression for the linear stress-shear rate relationship [24] (Eq. (2.1)). Where τ is the shear stress, μ is the effective viscosity, and $\dot{\gamma}$ is the shear rate in 1-D.

$$\tau = \mu\dot{\gamma} \tag{2.1}$$

The power-law model [24] (Eq. (2.2)) is able to mathematically account for the shear-thinning behavior observed in most cellulose-based gels, where m is the consistency index and n indicates the level of non-Newtonian behavior ($n = 1 \rightarrow$ Newtonian) in 1-D.

$$\tau = m(\dot{\gamma})^n \tag{2.2}$$

Its primary limitation is that it is unable to fit to any plateaus in the stress-shear rate relationship [20].

To account for this limitation the Ellis model introduces a third parameter (Eq. (2.3)), which incorporates the low shear rate Newtonian plateau [20, 24, 25] seen in the rheological data of HEC gels (Figure 2.2), where η_0 is the zero shear rate viscosity, λ is the measure of shear-

thinning behavior, and $\tau_{1/2}$ is the stress at which the apparent viscosity has dropped to half its $\tau\big|_{\eta_0}$ (stress evaluated at zero shear rate) value.

$$\frac{1}{\eta} = \frac{1}{\eta_0}\left(1 + \left|\frac{\tau}{\tau_{1/2}}\right|^{\lambda-1}\right) \tag{2.3}$$

In the shear-thinning region of the data, there are direct relationships between the Ellis and power-law models [24]. The measure of shear-thinning behavior, λ, is directly related to the power-law shear-thinning index: $n = 1/\lambda$. Therefore, as λ increases, the fluid exhibits more shear-thinning behavior.

There is an alternative way of writing the Ellis constitutive equation. This substitute strategy is particularly advantageous in this circumstance because the viscosity/stress data were obtained by varying the shear rate, while Eq. (2.3) expresses the viscosity as a function of the shear stress. Eq. (2.4) is an expression of the relationship between the shear rate and the stress [24].

$$\dot{\gamma} = \left(\varphi_0 + \varphi_1|\tau|^{\lambda-1}\right)\tau \tag{2.4}$$

The coefficients $\varphi_0 = 1/\eta_0$ and $\varphi_1 = (1/\eta_0)(1/\tau_{1/2})^{\lambda-1}$ are easily related back to Eq. (2.3). It should be noted that it is not trivial to explicitly express the stress term as a function of the shear rate as is desirable for fitting this equation to the rheology data. The technique for overcoming this limitation will be explained in the following section.

The Carreau model is able to account for plateaus in both low and high shear rate regions [20]. The advantage of using the Ellis model is that when deriving the thin-film flow model, the Carreau model does not allow for the explicit expression of velocity [20]. This simplification comes at practically no cost because the rheological data of HEC gels don't show a clear plateau

in the shear rate region that is of interest to our application. Therefore, the Ellis constitutive equation is an acceptable choice for mathematically representing the rheological properties of HEC gels.

Preparing the gels:

The gels were prepared by combining de-ionized water with hydroxyethylcellulose (manufacturer: Hercules, lot #: C1763, Type: 250 HX PHARM). The HEC percentage indicates its ratio of HEC to water in the mixture. The pH was not adjusted because this experiment was mostly intended for observing the effects of rheological characteristics on spreading characteristics along with initial condition effects. The water was heated to 80°C and stirred at ~750rpm (constant RPM) as HEC was slowly added. The mixture was left to stir for 60 minutes, or until no visible clumps of HEC were left. After the gel was created, it was refrigerated for approximately 24 hours.

One batch was made for each concentration (2.4%, 2.7%, 3.0% HEC). Each batch underwent rheology and spreading testing. In addition, to show repeatability of reproduction, 3 batches of 2.7% HEC gel were created. The rheological and spreading data comparing different batches can be found in Appendix B.

Rheological Testing:

Before testing the gels' rheological properties, each sample was inserted into syringes and centrifuged to remove air bubbles. Each gels' rheology was recorded using an AR2000 rheometer (TA Instruments) with a 2° aluminum cone (40mm diameter) geometry containing a humidity trap loaded with ionized water.

The gel was released onto a heated plate (37 ± 1 °C) and allowed to settle for several seconds. The geometry was then lowered to 69 μm and the excess gel was cleared from the edges of the geometry according to rheometer specifications. The geometry was then lowered again to a testing gap of 49 μm, as dictated by the cone angle.

Before obtaining rheological data, a test was run, for each HEC concentration, to confirm that every sample point was given sufficient time to reach equilibrium.
Initially, the gel was allowed to relax at the testing temperature for 5 minutes. The sweep test consisted of recording shear stress values for a shear rate sweep over 0.1/s to 100/s, on a log scale, sampling for 3 minutes at each shear rate. Each gel was tested in triplicate and the results were averaged at each recording of shear rate.

Rheological Test Results:

In order to incorporate the rheological characteristics of the HEC gel, the viscometric measurements were fitted with the two-parameter power-law and three-parameter Ellis models [24] for each gel.

Power-law

The average values of the shear stress, of triplicate experiments, were fitted with the power-law constitutive equation (Figure 2.2). Using the Nelder-Mead simplex direct search method, the second term of Eq. (2.5) was optimized to arrive at the best fit [3, 26, 27].

Eq. (2.5) represents the goodness of fit between the model and the measured values for the power-law constitutive equation; where y_i is the log of the measured data point, $\bar{y}$ is the log of the mean of the measured data points, and $\hat{y}_i$ is the log value of the power-law constitutive

equation corresponding to the same shear rate. An R^2 value of 0 would mean that there is no correlation, while a value of 1 indicates that both data sets are 100% the same [26, 27].

$$R^2 = 1 - \frac{\sum_{i=1}^{n}(y_i - \hat{y}_i)^2}{\sum_{i=1}^{n}(y_i - \bar{y}_i)^2} \qquad (2.5)$$

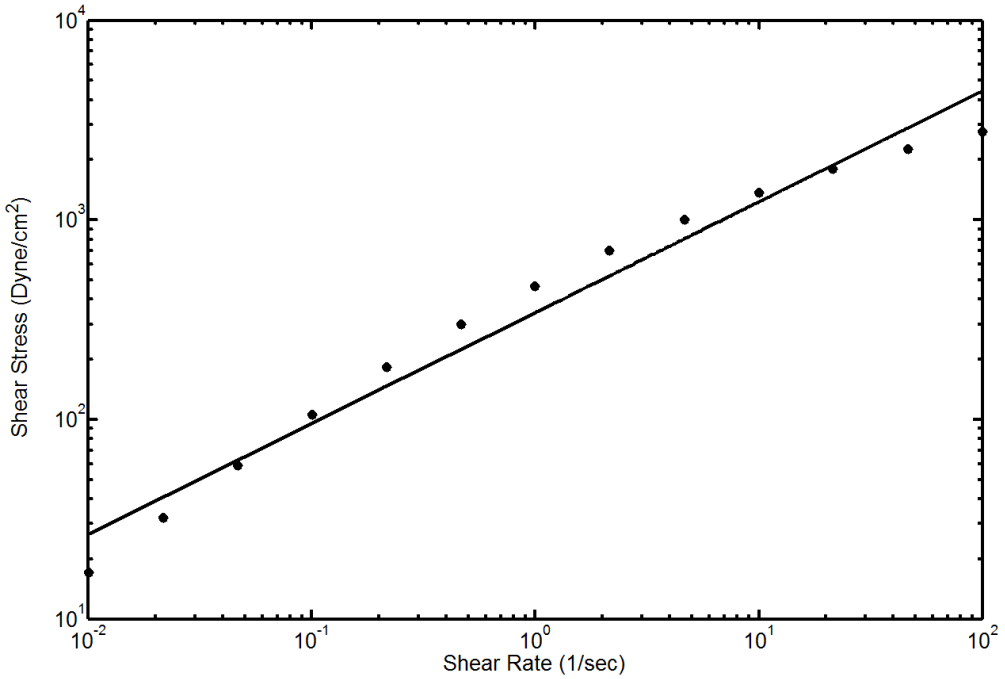

Figure 2.2. Example rheological data of 2.7% HEC gel. Dots represent the average stress values of three trials. Solid line represents power-law fit. Power-law model captures overall non-Newtonian trend of rheological data.

The viscometric measurements of the power-law fit are given in Table 2.1:

HEC Concentration % (w/w)	*m* (*Psec*$^{n-1}$)	*n*	R^2
2.4	227.9195	0.5951	0.9806
2.7	343.3896	0.5543	0.9793
3.0	479.6178	0.5207	0.9789

Table 2.1. Power-law parameters for gels of 3 different HEC concentrations. Note: $m \equiv$ consistency index; $n \equiv$ shear-thinning index; R^2 represents the goodness of fit.

As expected, the model embodies the fact that as the concentration of HEC increases, the *consistency index* of the gels will also increase along with the level of non-Newtonian behavior (i.e. *n* decreases).

Ellis

In order to account for the low shear rate Newtonian plateau in the rheology data, a third parameter had to be introduced into the constitutive equation.

There were 4 techniques of fitting the data with the Ellis constitutive equation to arrive at the three parameters: η_o, λ and $\tau_{1/2}$.

Technique 1:

The Ellis equation (Eq. (2.3)) was fitted to the viscometric measurements using a "curve fitting toolbox" from MATLAB. MATLAB uses a non-linear, least-squares method, of fitting to the non-log values of the measured data, to perform custom equation fits to non-linear data and calculates the correlation using Eq. (2.5).

Using the least-squared method for fitting the rheological data seems to produce a good fit that loses accuracy as it reaches the shear-thinning region. Fitting to the log of the residuals results in an improved approximation of the data, as will be seen in Technique 2.

HEC Concentration	η_o (Poise)	$\tau_{1/2}$ (Dyne/cm^2)	λ	R^2
2.4%	944.1	141.7	2.017	0.9942
2.7%	1813	151.4	2.045	0.9950
3.0%	3120	170.4	2.108	0.9970

Table 2.2. Ellis parameters fitted with the T1 technique. Note: $\eta_o \equiv$ zero shear Newtonian viscosity plateau; $\tau_{1/2} \equiv \tau\ (1/2\ \eta_o)$; $\lambda \equiv$ measure of shear-thinning behavior; R^2 represents the goodness of fit.

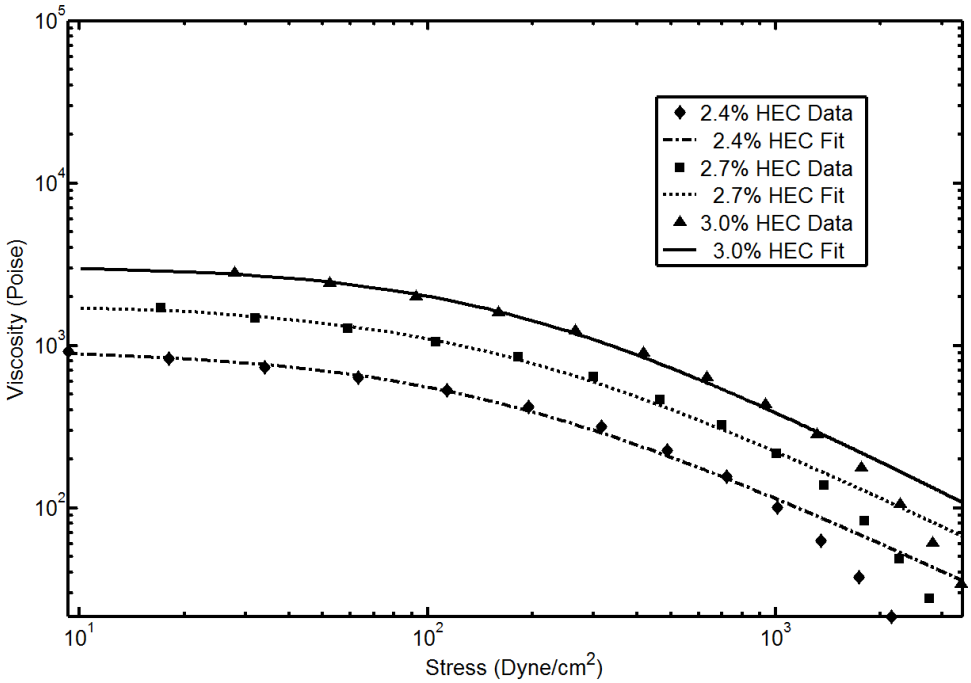

Figure 2.3 Rheological data for 2.4%, 2.7% and 3.0% HEC gel fitted with the Ellis constitutive equation (T1). With T1 fit, Ellis model fits well with data at low shear rate, but diverges from data at higher shear rates.

Figure 2.3 shows viscosity vs. shear-stress rheological data for 2.4%, 2.7%, and 3.0% HEC concentrations. The dependent and independent axes of this plot are different from the power-law plots because the Ellis constitutive equation is a function of viscosity and stress as opposed to the power-law constitutive equation, which is a function of stress and shear rate.

Even though the agreement between the data and the fit was modest at the shear-thinning region, the R^2 values were surprisingly good.

Technique 2:

The Ellis equation (Eq. (2.3)) was fitted using the log of the residuals, as it was done for the power-law constitutive equation (Figure 2.4). As a result, the quality of the fit seems to be an improvement over Technique 1, when considering the entire data set.

HEC Concentration	η_o (Poise)	$\tau_{1/2}$ (Dyne/cm^2)	λ	R^2
2.4%	762.56	276.98	2.604	0.9895
2.7%	1370.50	331.70	2.700	0.9888
3.0%	2264.90	381.00	2.800	0.9887

Table 2.3. Ellis parameters fitted with the T2 technique. Note: Parameters defined in Table 2.2.

After implementing this fitting technique, we see that the Newtonian plateau is decreased and the shear-thinning region is better accounted for by increasing the value of $\tau_{1/2}$ and λ.

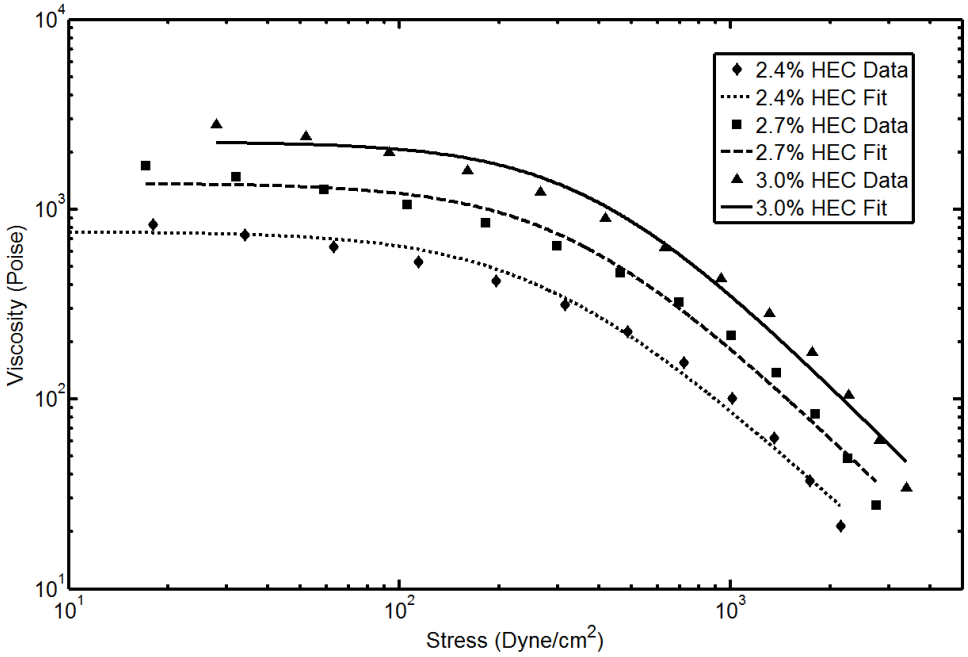

Figure 2.4 Rheological data for 2.4%, 2.7% and 3.0% HEC gel fitted with the Ellis constitutive equation (T2). With T2, the Ellis model improves fit between rheology data and model of viscosity to shear stress relationship.

Technique 3:

There is a direct relationship between the Ellis and power-law constitutive equation. They are both intended for modeling the shear-thinning region of non-Newtonian rheology data, but the power-law is not capable of accounting for the Newtonian plateau at low shear rate.

Nevertheless, Bird, Armstrong, and Hassager [24] identified a relationship between the power-law and Ellis parameters as:

$$m = \eta_0^{1/\lambda}\,\tau_{1/2}^{1-(1/\lambda)} \qquad n = 1/\lambda \qquad (2.6)$$

I used this relationship, along with the power-law parameters presented in Table 2.1, to arrive at the Ellis parameters for T3. The viscosity of the Newtonian plateau was obtained from Table 2.3.

HEC Concentration	η_o (Poise)	$\tau_{1/2}$ (Dyne/cm^2)	λ	R^2
2.4%	762.56	38.63	1.68	0.7849
2.7%	1370.50	61.41	1.80	0.8320
3.0%	2264.90	88.82	1.92	0.8656

Table 2.4. Ellis parameters fitted with the T3 technique. Note: Parameters defined in Table 2.2.

When plotted with the actual data, this technique results in a modest description of the rheology data, but it's a good approximation of the overall trend (Figure 2.5). The resulting approximation appears similar to the power-law fit with a plateau region at low shear rate.

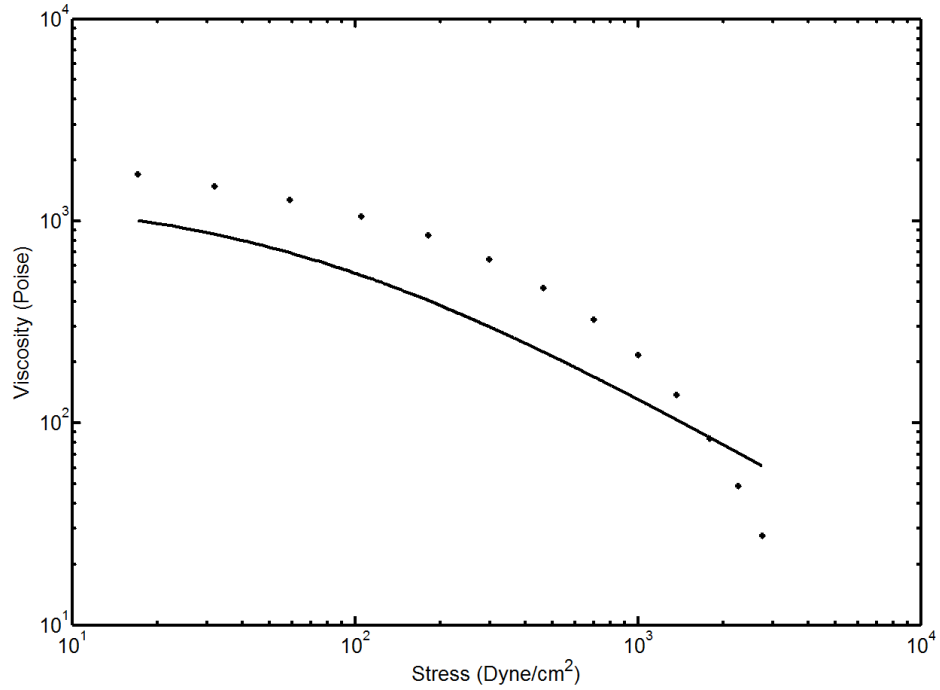

Figure 2.5 Rheology data (dotted) of 2.7% HEC fitted with Eq. 2.3 (solid) using the values from Table 2.3. (2.4% and 3.0% HEC fits are omitted for clarity). Using the relationship between Ellis and power-law constitutive equations, the Ellis model produces a modest fit of rheology data.

Technique 4:

Because the rheology data was actually acquired by controlling the shear rate, the Ellis equation (Eq. (2.4)) was used to fit to the original stress data vs. shear rate. A predicament occurs since in Eq. (2.4), it is not trivial to explicitly write an expression for the stress as a function of the shear rate. When minimizing the norm of the log of the residuals, I solved Eq. (2.4) for the stress at each value of shear rate by using Newton's method, set to converge at an error of 10^{-10}.

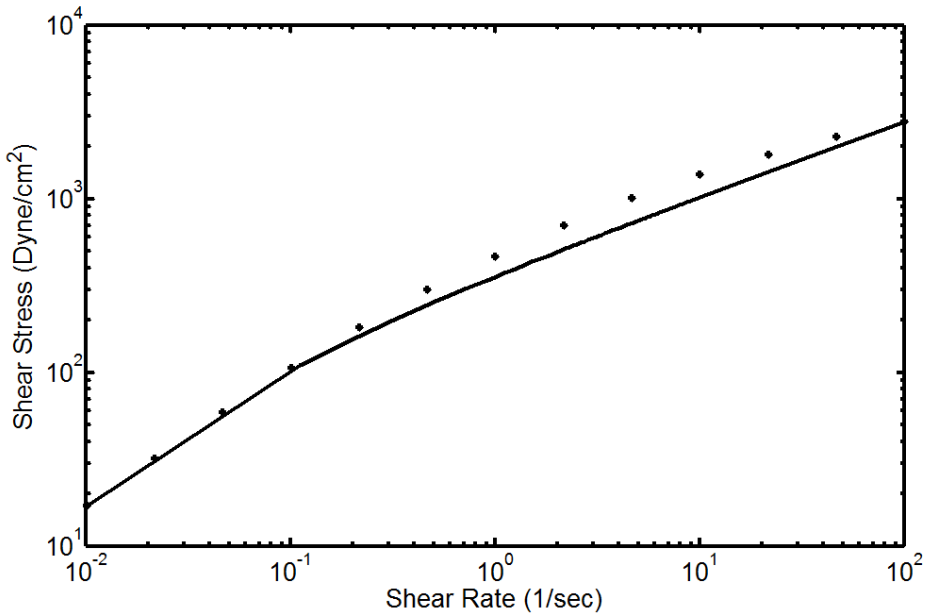

Figure 2.6 Rheology data (dotted) of 2.7% HEC fitted with the Ellis equation (Eq. (2.4)) (solid) using the values from Table 2.5. (2.4% and 3.0% HEC fits are omitted for clarity). Using T4 allows for fitting to the shear rate vs. shear stress data, with good agreement at low shear viscosity.

HEC Concentration	η_o (Poise)	$\tau_{1/2}$ (Dyne/cm^2)	λ	R^2
2.4%	1000	137.72	2.391	0.9948
2.7%	1590	174.01	2.461	0.9925
3.0%	2883	260.01	2.732	0.9944

Table 2.5. Ellis parameters fitted with the T4 technique. Note: Parameters defined in Table 2.2.

Discussion and Conclusions

The rheological parameters in this chapter will be used as input parameters into the numerical models described in the subsequent chapters. It is important to note, as will be discussed in Chapter 7, that the power-law and Ellis models are only capable of capturing the shear-thinning part of an otherwise very complex behavior of HEC gels. Moreover, as was seen with the Ellis constitutive equation, even using different methods for fitting the data can result in different output parameters.

In Chapter 6 (Ellis) I will explain which fitting technique was used when presenting results.

From a thermodynamics perspective, one might consider verifying that the constitutive equations satisfy the Clausius-Duhem inequality (second law of thermodynamics). For a microbicide application, the Reynolds number is low enough that I can neglect any heat loss.

Chapter 3 INSTRUMENT AND METHOD FOR VISUALIZING AND CHARACTERIZING GRAVITY-INDUCED FLOW

Introduction

Our team's long-term goal is to design an effective microbicide delivery vehicle with optimized spreading characteristics. A crucial step in reaching this goal is being able to conduct spreading experiments that are capable of validating numerical models and providing reliable spreading data. This chapter will address this project's first overall objective: to design an instrument and technique for obtaining experimental flow characteristics along with surface topography of spreading gels. In addition, performing spreading tests on this instrument will provide data that will be used in Objectives 3 and 4.

Significance and Chapter Goals

When conducting 3-D gravity-induced flow experiments, there are two common objectives which present challenges: dispensing the gel on to the spreading surface in a way that resembles the physical process that is being modeled, and numerically representing the 3-D shape of the fluid [28]. The 3-D shape is needed for two reasons: (1) to recreate the initial shape of the experiment and use it as the initial condition in the numerical model and (2) to compare the spreading characteristics of the experiment with the numerical model at later times.

In detail, challenges of capturing the 3-D shape of a fluid include:

(a) Obtaining the instantaneous shape of a fluid as it is spreading. Some methods can take minutes to analyze and capture the shape of an object, which is not a practical option during an experiment.

(b) Dispensing and releasing a fixed volume of fluid without disturbing its spreading or its environment.

(c) Capturing the shape of the fluid without bulky equipment.

OBJECTIVE 1: The objective of this chapter is to present an instrument and a technique for performing spreading tests with the ability to:

1. Provide a humidified, temperature-controlled environment that simulates aspects of the vaginal lumen (37±1°C, <70% Humidity), and prevents the gel from drying during the experiment.
2. Dispense an initial condition without the applicator in contact ("Contact Free"), and create a repeatable initial shape.
3. Represent the spreading gel at any point during the spreading as a computerized mesh, which can be used for implementing the experimental initial condition into numerical code.
4. Quantify the characteristics of gel spreading in the axial and lateral direction as a function of time.

The engineering goal of this chapter is to introduce a new instrument and method for releasing a "contact-free" spreading sample, measuring free surface topography, and obtaining

spreading characteristics of a bolus of fluid spreading in a humidity/temperature controlled environment.

The novel contribution of this work is a method to repeatedly dispense a gel onto a spreading surface, to quantify the shape of the initial condition using a 2-D mesh discretization matrix, and to measure the characteristics of the gel's spreading properties at any point in the spreading process.

Review of Relevant Literature

Experiments of free surface coating flows are useful for many applications, such as: geophysical flows [29], industrial flows [30], and mathematical instability analysis [31, 32]. For a drug delivery application [2], my colleagues and I have been needing to do similar experiments, and corresponding numerical simulation, in order to optimize and design new polymeric liquids for the topical vaginal delivery of anti-HIV microbicidal agents. However, previously existing methods to image and analyze free surface coating flows do not meet the specific needs of our objectives.

Incorporating experimental initial condition topography into a computational simulation is a challenge, especially when evaluating microbicide delivery vehicles, because the physical application of the vehicle by a potential user must be taken into account. Therefore, in our experiment, the polymeric liquid must be applied to the spreading surface using a syringe that will break contact with the fluid immediately after application – a *contact-free* dispensing method. Instantly after contact is broken, surface topography of the fluid is needed as the initial condition in the numerical model. As the fluid begins to spread, quantities such as coverage area, thickness (up to 1 *cm*), and spreading rate should be obtainable at any instance of time to verify

numerical results. And finally, all this must be done in a controlled environment that replicates body temperature and humidity, so that the gel does not dry during the test.

In the past, researchers have tried several techniques to capture the shape and thickness of a spreading fluid at a brief instance in time, but all these methods have restrictions that do not meet the needs of my application. Research on thin-film dynamics has given birth to several different non-intrusive techniques to measure thin-film spreading, thickness, and surface waves.

In 1952 Duckler and Bergelin [33] measured the average film thickness by placing the spreading fluid between two conducting plates and measuring the capacitance between them. By finding the relationship between the capacitance and the air gap (distance between fluid surface and top plate), they could effectively measure the thickness of the film. Because this method can only give the average thickness for a small region of interest, it is not capable of mapping the surface topography of a large area that is constantly deforming. Ambrosini *et al.* [34] and Roy *et al.* [35] considered a larger region of interest by placing capacitance probes in different parts of the spreading domain. This was a successful method for obtaining a film thickness distribution along the entire spreading surface. However, due to the large size of each probe it would be impossible to set them up to measure surface topography at an acceptable spatial resolution for our application. In addition, stray electromagnetic fields can cause equipment malfunction and it is unlikely that this method could measure capacitance across air gaps as large as 10 *mm*. This is too restrictive for our application because the height of a given sample may vary from 1 to 9 *mm*, spanning along its length.

Liu *et al.* [36-38] used laser beam deflection together with a fluorescent imaging technique to measure the properties of traveling waves on a film's surface. The laser beam deflection technique is only capable of giving the local surface slope at a specific point and

cannot be used for mapping an entire surface that is constantly changing in time. The fluorescent imaging technique will be discussed later.

Zaitsev *et al.* [39] used a double-fiber optical probe that they were able to move along the free surface to measure the thickness of thin, smooth films. The limitation of this method was that it could only provide local film thickness and every measurement presented in that study was below 1 *mm*.

Lel *et al.* [40] compared a chromatic confocal imaging method and a fluorescence intensity technique for obtaining film thickness. Both techniques provided accurate measurements of fluid thickness (less than 1 *mm*) at a specific point, but could not instantaneously map the surface. Also, the measurement system for the fluorescence intensity technique must be within a few millimeters of the spreading surface making it an unrealistic option for surfaces with large variation in height. The chromatic confocal imaging method [40, 41] can be used at a gap of 1 *cm*, but is also an unrealistic option for our application due to its coverage-area limitation.

Techniques such as the anamorphic schlieren system [32, 42] and the laser focus displacement instrument [43] can provide a slice of thickness in one plane of interest, but are incapable of scanning an entire surface at an instant of time. Laser focus displacement is also limited in that it can only measure thickness within 2 *mm*, and is inaccurate at steep changes in surface topography occurring at spreading edges. The anamorphic schlieren system can give an entire footprint of the spreading fluid's leading edge [31, 32], but it remains unclear if it can map the edges at the trailing end or the sides of a fluid with a finite width.

In contrast to the thin-film experimental methods, a few techniques (summarized below) have been developed to measure the topography of thicker layers (more than 1 or 2 *mm*) of a

spreading fluid. However, these techniques are also too restrictive for our needs, or do not implement a suitable dispensing mechanism. For example, Johnson *et al.* [44, 45] applied a fluorescent imaging technique to successfully measure surface topography of thicker films (up to 10 *mm*), but did not include a method to automatically dispense a contact-free, finite volume of polymeric liquid. The fluorescent intensity to fluid-depth data presented in that study shows that the relationship could be strongly non-linear depending on the fluid being tested and is extrapolated for any depth greater than 3.5*mm*. In addition their averaging process to normalize the UV illumination intensity might be problematic for a large finite volume of fluid (up to 1 *cm* in height), with large variations in height, that is constantly spreading in three-dimensions. The technique presented here offers an alternative way of approximating surface topography and also describes a new method to automatically dispense a contact-free initial shape of gel.

An earlier approach by Kieweg *et al.* [2] was to hold and release a finite bolus of gel from a frame, momentarily controlling the shape of the initial condition. Such a method, like others with surfaces that are in contact with the fluid right up until the experiment began [46-48], can lead to problems with fluid adhering to the loading frame when it is removed [2]. In addition, it is hard to activate such an apparatus unless an operator can reach it with his/her hand, and therefore it is difficult to do in an environment-controlled chamber. It is also important to note that the box-like initial condition produced by a rectangular frame in this method might not work well with some numerical methods that need a certain level of smoothness in order to minimize error [49]. Thus, these methods do not satisfy our need for a contact-free initial condition.

Another approach is to take advantage of a fluid's yield stress to set up a stable, contact-free, initial shape before the flow experiment began. In one particular test, a kaolin slurry was extruded from the base of a horizontal surface and allowed to settle into a constant-volume,

stable shape [28]. The mathematical approximation of the slurry's shape (the dome-shaped Nye solution [28]) was used as the numerical initial condition before tilting the spreading surface for the experiment. However, only fluids with a yield stress (e.g. kaolin slurry [28]) could be tested using this technique because fluids without a yield stress would continue to slump before the start of the experiment. The yield stress requirement is too restrictive for applications that consider polymeric liquids without a yield stress (such as cellulose-based microbicide delivery vehicles). In addition, that dispensing method injected the fluid at the base of the spreading surface to model a specific phenomenon, which is not consistent with our application and can impact flow characteristics.

Cochard and Ancey [46, 47] employed an imaging analysis technique, analyzing changes of patterns projected onto the fluid surface, to reconstruct the free surface profile and obtain the spreading rate of an avalanching mass of fluid. The release mechanism for the dam-break experiment in that study is specific to applications with a *source* of fluid (i.e. geophysical flows) and is not applicable for spreading experiments of a *finite* (constant-volume) bolus of fluid. Also, while the technique was effective for mapping the surface of the sample, it did not acquire the complete footprint and was demonstrated only on the leading edge. Nevertheless, Schwartz and Eley [30] applied this technique to a finite bolus of fluid, but did not show clear resolution and borders at the trailing edge.

There are methods that use ultrasonic waves for measuring surface topography, but they are limited in the amount of surface area they can scan at one time point [48]. Therefore, when considering a large surface area that is continuously deforming, they are incapable of analyzing the entire surface at a specific time point.

Here we present a dispensing/imaging procedure, capable of automatically releasing a contact-free bolus of a polymeric fluid on any surface and obtaining topography and spreading characteristics over time. The apparatus and procedure yields measurements that are accurate within 0.5%, in a temperature and humidity-controlled environment, with repeatability. This apparatus and method will be useful for providing an initial shape as input to 3-D numerical simulations, and for verifying the time-dependent results of numerical simulations. The system described in this paper is ideal for our application of gravity-driven flows of polymeric microbicide delivery vehicles, but is also applicable to any field of research in which free surface, gravity-induced flow is of interest.

Methods

The new apparatus and method consists of an environment-controlled chamber, spreading surface, release mechanism and camera (with calibration and image analysis technique) (Figure 3.1).

There were four main criteria for the experimental setup: (1) The syringe must release the gel on the spreading surface at a consistent 45 degree angle relative to and regardless of the spreading surface angle; (2) the rate of release must not vary between experiments of the same gel; (3) after release, the syringe must detach from the gel to ensure "contact free" initial conditions; and (4) the top and side profile of the gel must be visible at all times during the experiment.

Environment-Controlled Chamber

The chamber is rectangular in shape with physical dimensions of 35.625” x 7” x 34.75”. The chamber walls are made of 0.5” and 1” transparent Acrylic Plexiglas.

An air-heating element (1025W Finned Tubular) maintained the temperature of the environment and two 12V fans circulate the air. Temperature was acquired using two thermocouples (NI Type E) strategically placed to ensure that the whole environment in which the experiment was taking place was uniform. Temperature control (within 1°C) was accomplished with a custom NI LabView 8.6.1 feedback control system program using a data acquisition card (NI PCI 6221 DAQ). Temperature was validated using two high accuracy Fisherbrand thermometers (Red-Spirit, partial immersion).

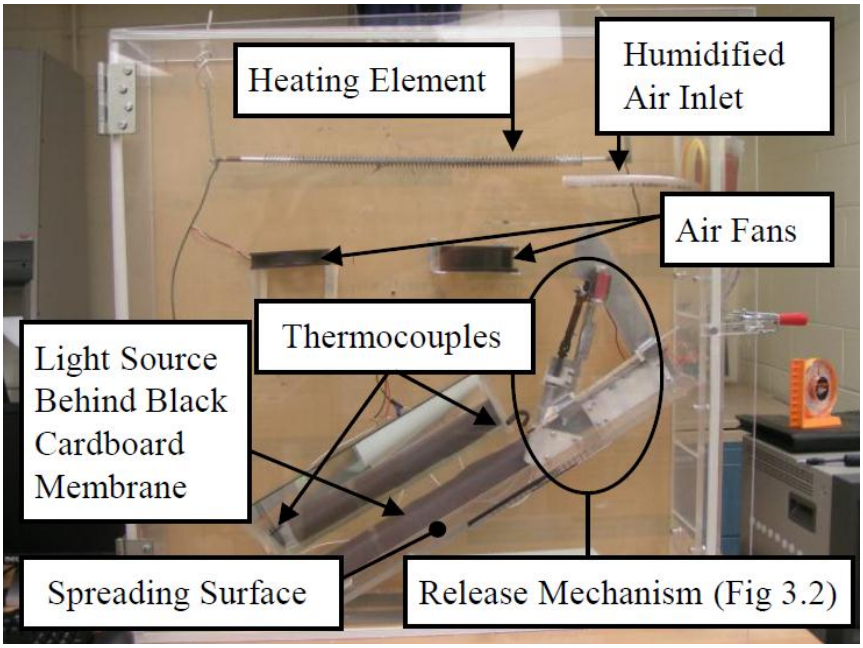

Figure 3.1. Picture of temperature/humidity chamber.

Humidity was provided using an ultrasonic cool-mist air humidifier (Sunbean Ultrasonic Humidifier 700), pumping at a constant rate, and measured with a humidity indicator (Fisher

Scientific). Because excess humidity would obstruct the camera's field of view, every experiment was started after chamber humidity reached 70%.

Spreading Surface

The gel spreads on a polycarbonate surface. The ramp was designed so that any other surface can be attached and detached with ease. For example, in future work, users can perform spreading experiments conducted on a surface of bovine vaginal epithelial tissue. The tilt angle of the spreading surface (with respect to the horizontal) can be changed in 10° increments (0-80°).

Gel Release and Syringe Detachment Mechanism

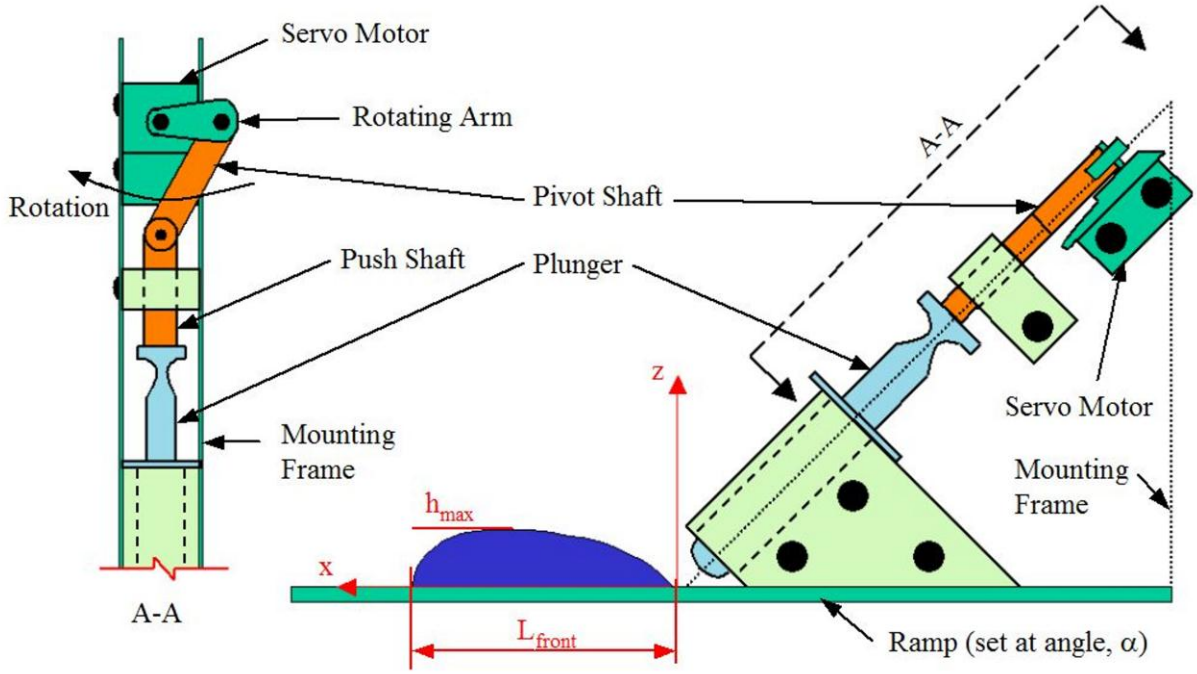

Figure 3.2. Mechanical drawing of side view of release mechanism, definition of spreading characteristics and overall assembly of apparatus. Cross-section A-A shows that during 180° of servo rotation, plunger releases gel and gets retracted from the spreading surface to obtain a contact-free initial condition.

A servo motor (JRSERVO DS8711) was used to press the gel out of the syringe (Figure 3.2). The servo motor control software was developed using NI LabVIEW 8.6, and connected through a data acquisition card (NI PCI 6221 DAQ). Servo motor rotation rate was controlled using pulse width modulation (PWM) analysis and optimized to achieve a dome-like shape (~$\pi/2$ rad/sec).

Once the servo was activated, the "servo-rotating arm" (Figure 3.2) converted rotation to linear motion, thereby compressing the plunger. The first 90° of the rotation was responsible for compressing the plunger, while the second 90° retracted it from the gel (Top View of Figure 3.2). This simple mechanism achieved a contact-free initial condition with a manageable shape, reproducible over multiple experiments.

Top and Side View Image Acquisition

This instrument was designed to reproduce gel geometry with a computerized mesh and characterize spreading in both the axial and lateral direction. In order to avoid the complexities of synchronizing two separate cameras, for the side and top view, a mirror was installed (Figure 3.2) with the reflective plane 45° to both the spreading surface and the camera (Figure 3.3).

The instrument contains an optional single light source positioned directly behind the side view of the gel (Figure 3.3) (not used in this study). If needed, light can be diffused using a black cardboard membrane, which (after experimenting with many different configurations) I found most clearly accentuated the edges of a transparent gel. In this study, only ambient room lighting was used and the gel was colored using a food coloring dye (0.3 *ml* of water volume), which was confirmed not to affect rheological properties and did not require the use of a background light source.

During the experiment, gel spreading was recorded using a camcorder (Aiptek HD-DV, 1280x720 HD, 30 fps) positioned directly outside the chamber (Figure 3.3). The camera captured the side view of the gel and the top view from the image reflected in the mirror (Figure 3.3 b). The resulting video file consisted of images that were 1008x576 pixels. When doing measurements using image analysis, it is important to determine how each pixel of the image corresponds to a physical dimension of the space being photographed (pixel to real-world calibration). Because the lens of the camera is concave and parts of each image are observed at an angle, a complex calibration algorithm is required.

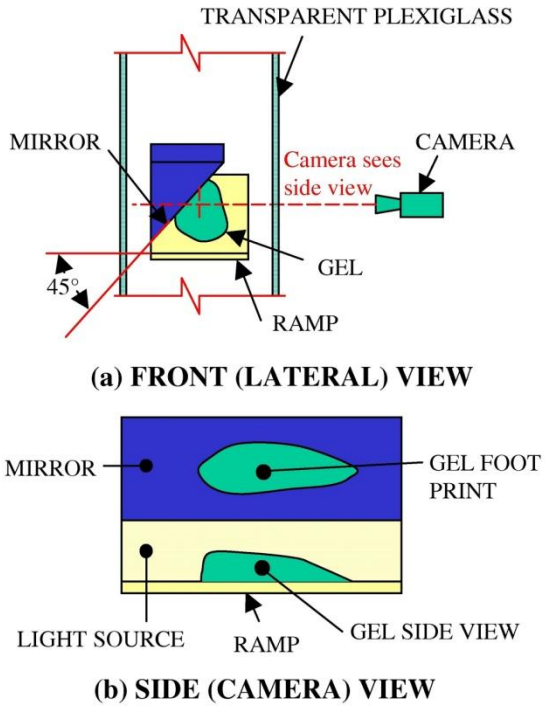

Figure 3.3. Apparatus and camera configuration. (a) Shows side view of chamber with camera capturing side and top view profiles. (b) Shows views seen by camera.

It would be inaccurate to determine the dimension of a single pixel, and assume that it would correspond to every other pixel in the image. Ordinarily, the position and zoom of the camera would affect the calibration and must remain constant for every experiment. With this

technique, the camera position between experiments did not have to be exactly the same because a method (described in the next section) was employed to obtain pixel to real-world calibration within 1mm accuracy, for each experiment, regardless of camera position or zoom.

Calibration

Once the camera was positioned and set in a way that was suitable to film the side and top profile of the spreading experiment, the camera's recorder was activated and top-view and side-view calibrations were performed as follows. First, specially manufactured grids of dots at 5mm intervals were placed on the spreading surface. Using the dots on the grid, the camera captured spacing of 5mm increments of both the top and side view (Figure 3.4).

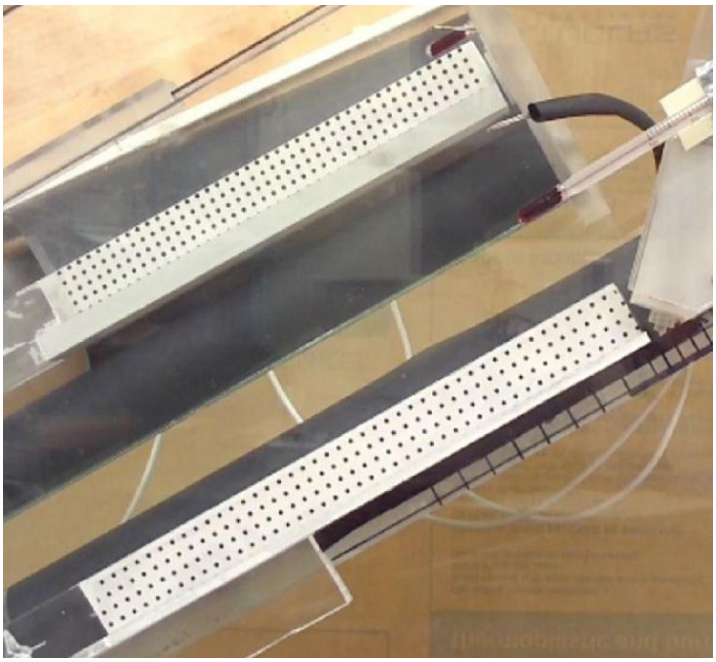

Figure 3.4. Top-view and side-view calibration image with calibration grids. Calibration technique eliminates error from: (1) camera position changing between experiments, and (2) pixel to real world conversion non-linear relationship with camera view perspective.

A calibration was completed using NI Vision Assistant 8.6, employing the software's non-linear calibration algorithm, which accounted for the camera's distortion of an image as it

got further away from its center by measuring the distortion of the dots. Vision Assistant created a calibration file that could be incorporated into any LabVIEW code being used for image analysis.

I determined the measurement and calibration accuracy by first performing a calibration, then recording the centroid (the energy center of a dot) of five specific dots positioned throughout the grid, and then verifying that their calibrated, measured distances relative to the bottom-right dot were as expected: within 1mm (Table 3.1).

Table 3.1 shows an example of a side-view calibration. The % accuracy results are all less than 0.5%, allowing me to conclude that measurements taken within the spreading domain are accurate.

Reference Point	**Actual Point (*mm*) Coordinates**	**Measurement (*mm*)**	**|(% Accuracy)|**
A	0,0	0,0	---
B	30,0	30.06,0.01	0.2
C	30,10	29.85,9.96	0.45
D	50,10	49.83,9.95	0.33
E	50,0	50.13,-0.23	0.26
F	80,5	79.87,4.95	0.16

Table 3.1. Example of side-view calibration measurements of points. (The point of origin, A, was positioned in the bottom right corner of the grid. The % accuracy was determined using the total length of the vector between two points.)

Performing this calibration process for every experiment separately ensures accuracy for each experiment. This method, in conjunction with image analysis, allows for pixel to real-world calibration within 1*mm* accuracy regardless of camera positioning or zoom.

Experiment

After completing the calibration, the grid was removed and the chamber was sealed, allowing for the spreading experiment to begin once the proper temperature and humidity levels

were reached. After 180 seconds of spreading was recorded, the .avi file was transferred to a PC for analysis. Quick Time Player was used to export the movie into frames of 1-second intervals to analyze a successive 180 frames of spreading. The first frame was considered to be the initial condition, taken at the point when the syringe first breaks contact with the gel.

Image Analysis

Each image underwent an image analysis procedure (Figure 3.5) developed using LabVIEW 8.6. The analysis procedure performed a "Color Plane Extraction" to convert all the pixels to a green plane, which made an image containing one color with different intensities. Then, I performed a Logarithmic Image Sequence (LIS) and highlighted the details using a LabVIEW algorithm.

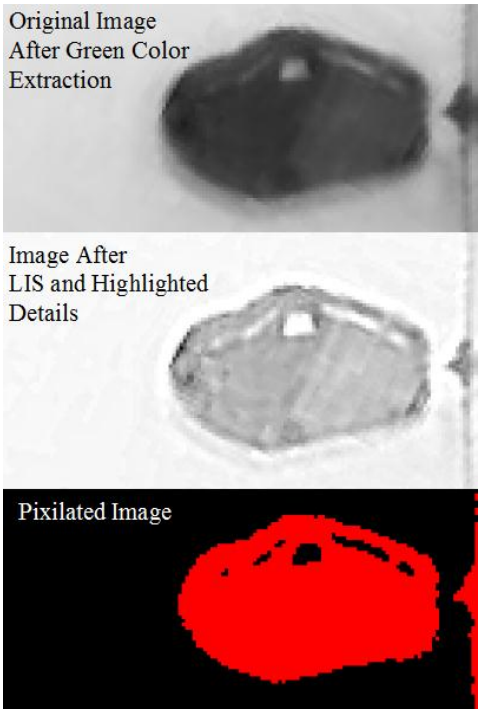

Figure 3.5. Example of image analysis procedure on top view. Each image undergoes green color extraction (top), edge highlighting algorithm (middle), and is turned into a binary for measurement (bottom).

This procedure allowed me to eliminate "shadow" noise, and analyze the true fluid edges. Afterwards, the image was turned into a binary, which eliminates most noise from the image, and analysis of flow characteristics could be executed.

Using image analysis software written in LabVIEW, the calibrated coordinate position of the fluid edge was found for every pixel within a user-defined domain, leading to the calculation of the maximum length, width and height of the fluid in each image. The following procedure was performed for each image in the 180-second sequence to determine the maximum length, width and height as a function of time thus resulting in the fluid's spreading characteristics.

Surface Topography of the Initial Condition

In addition to providing spreading dimensions, the image analysis procedure produced a height matrix (over a user-specified N x M grid domain) of the gel for any time frame in the spreading experiment. N and M are the number of spatial nodes in the axial (downhill) and lateral direction, respectively (Fig 3.6).

To approximate the surface topography of the fluid, the image underwent the same process described for spreading characteristics analysis, to arrive at a binary image clearly showing the edges of the side view profile (representing the height at the centerline axial plane) and the footprint (z-plane). The pixelated edges (due to the binary image) of the side profile and footprint were smoothed using the least squares method to find a general polynomial fit. The degree of the polynomial was chosen based on the shape and dimension of the curve in comparison with the image.

The surface topography of the fluid was constructed by combining the views of the axial (side-view profile seen in camera view) and z-planes (footprint seen in mirror), while assuming a

cross section defined in Eq. (3.1) along the lateral plane, which was not captured in the camcorder view (Fig 3.6). The algorithm prompts the user to define the number of nodes (*N* x *M*), and a mesh size (*dx* and *dy*, *in mm*). If the desired mesh size was finer than the one available by the resolution of the camera, linear interpolation was used to obtain the three parameters: d_t, d_b and *h* (in *mm*) (Fig 3.6) for each gel edge dimension along the axial plane and the z-plane.

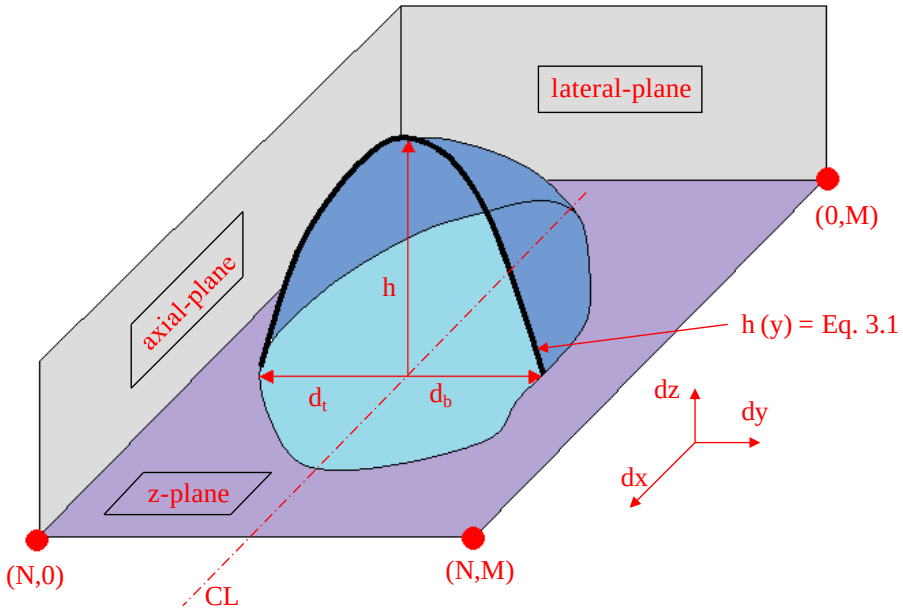

Figure 3.6. A conceptual image of how dimensions and planes are defined. *N* and *M* are the number of spatial nodes in the axial and lateral directions, respectively. Values d_t and d_b are distances from the centerline (*CL*) to the gel edge, measured using the top view, at each increment of *N*. Measurements of height are denoted using *h*, which are the distances from the spreading surface to the top surface of the gel, measured using the side view.

The assumed parabolic-like shape in the lateral direction was selected with a shape factor (*F*) and represented as:

$$h(y) = -F \cdot \frac{16 h_{max}}{(d_t + d_b)^4} \left(y - d_b - \frac{d}{2} \right)^4 + h_{max} \qquad (3.1)$$

The shape factor (*F*) adjusted the volume of the mesh to match the volume used in the experiments, as measured with volume indicators on the syringe. (For experiments here, volume

was matched within 0.1ml for a 3.8*ml* initial experimental volume.) As can be seen from Eq. (3.1), having the footprint dimensions (d_t, d_b) and the height (h_{max}) (Figure 3.6) at a specific point along the *N* mesh allows for Eq. (3.1) to calculate an appropriate cross section.

The origin of Eq. (3.1) is relatively straight-forward and omitted for brevity. It stems from 4th order polynomial, with roots at d_t and d_b and a maximum height at h_{max}.

Spreading Experiments

Spreading experiments were conducted on three concentrations of HEC gels (2.4%, 2.7%, and 3.0% HEC), each concentration (from a single batch) tested in triplicate. For each experiment, the plunger automatically dispensed an approximately 3.8±0.1 *ml* bolus of gel onto a plexiglass surface set at a slope of 30° with respect to the horizontal, and was allowed to spread for 180 seconds.

Results and Discussion

The image analysis process in conjunction with the image calibration described in the Methods section allowed me to obtain axial and lateral spreading characteristics within 1*mm* over a 80*mm* spreading domain (all measurements were within 0.5% accuracy).

Table 3.2 shows spreading data of 3 HEC concentrations tested in triplicate. Each experiment was compared with corresponding numerical simulation that used the experimental topography as the initial condition (Chapter 5). For a 180 second test, gels with lower concentrations of HEC spread further in the axial direction than gels with higher concentrations. Interestingly, gels with lower concentrations also got thinner, but did not diffuse as far in the lateral directions when compared with gels containing higher concentrations. There does not

seem to be a correlation between initial bolus height and lateral diffusion. Therefore, it is not immediately clear why higher HEC concentrations cause greater lateral diffusion. It might be due to surface tension affects, which should be investigated in future studies.

The influence of gel development on behavior variability is discussed in Appendix B by comparing the spreading behavior and rheology of different batches with the same HEC concentration.

Concentration	ΔL	ΔW	Δh	h_0
2.4% HEC	58.25±3.18 *mm* (5.46%)	3.34±0.66 *mm* (19.76%)	3.27±0.43*mm* (13.15%)	7.46±0.49*mm* (6.57%)
2.7% HEC	38.07±0.77 *mm* (2.02%)	4.44±0.57 *mm* (12.84%)	3.18±0.30*mm* (9.43%)	7.29±0.12*mm* (1.64%)
3.0% HEC	29.38±1.69 *mm* (5.75%)	4.65±0.48 *mm* (10.32%)	2.95±0.40*mm* (13.56%)	8.64±0.25*mm* (2.89%)

Table 3.2. Spreading data of gels containing 2.4%, 2.7%, and 3.0% HEC concentrations (n = 3 from 1 batch of each concentration). ΔL and ΔW represent total axial and lateral spreading, in 180 sec, respectively. Δh represents the change in height, with h_0 being the initial height. The data show more axial spreading and less lateral diffusion for lower HEC concentrations. **Note: Each cell presents the: Mean ± Standard Deviation (Coefficient of Variation).**

Figure 3.7 shows curves of 3 runs of a 2.7%HEC gel. The axial spreading curve seems almost linear, while lateral spreading appears to nearly plateau at approximately 90 seconds.

A separate, but identical, experiment was conducted on untreated glass, only to find that the variability of spreading characteristics between experiments of the same fluid were occasionally as large as 1 *cm*. This result confirmed a study by Kieweg *et al.* [2] that showed variations, when spreading on glass, can be large. Further investigation revealed that condensation on the glass surface was the culprit that was to blame for this surprising result, and that spreading experiments on plastic materials were more consistent. This short study alludes to the fact that the spreading surface can have an impact on spreading characteristics and, most

importantly, repeatability of the results. Therefore, in future studies, it is important to repeat these spreading experiments on epithelial tissue, which might reveal that any potential theoretical model would have to account for slip at the gel-epithelium interface (see more on slip and surface interaction in Chapter 7).

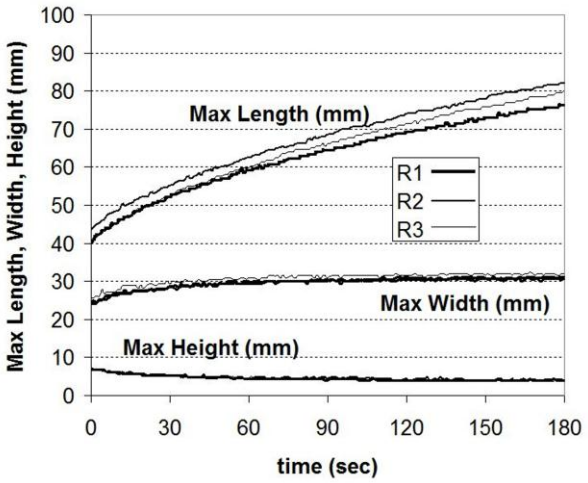

Figure 3.7. Spreading characteristics of the gel as a function of time for three repeated experiments of the 2.7% HEC gel.

Figures 3.8 and 3.9 show the surface topography obtained with the new method and apparatus for the same example data. The results show very good agreement between the photographed images and digitized surface meshes (Fig 3.8).

I chose the camcorder and apparatus dimensions for my specific application where a 1-image/sec and 1 *mm* accuracy over an 80 *mm* domain were sufficient. For other applications that require higher accuracy and time resolution, researchers may choose different apparatus dimensions or a camera/camcorder/frame-grabbing software with appropriate capabilities (e.g. finer pixel resolution, faster image-grabbing frequency).

The careful design of the automated dispensing mechanism created a smooth, dome-shaped initial condition that did not fold over onto itself, a phenomenon that could not be digitized/viewed with this technique.

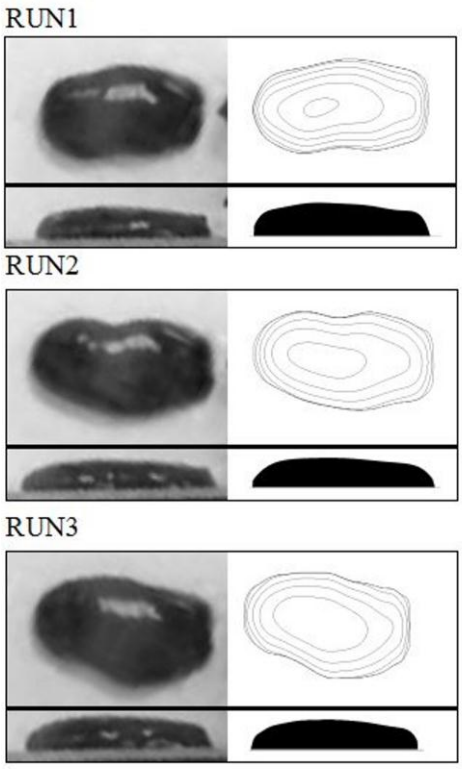

Figure 3.8. Comparison of photo image (immediately after the gel was dispensed on the spreading surface) with resulting digital surface topography of 3 repeated experiments of the 2.7% HEC gel. Left: top and side view of the photograph image of experiment initial condition. Right: top contour and side view of the resulting digital surface topography. There is good qualitative agreement between the photographic images and their computational reconstruction.

This apparatus does not provide a lateral view, but the assumed parabolic shape in that dimension was qualitatively similar to the dome-like shape observed at the start of the experiment. This method also ensured that the digitized volume exactly matched the known experimental volume.

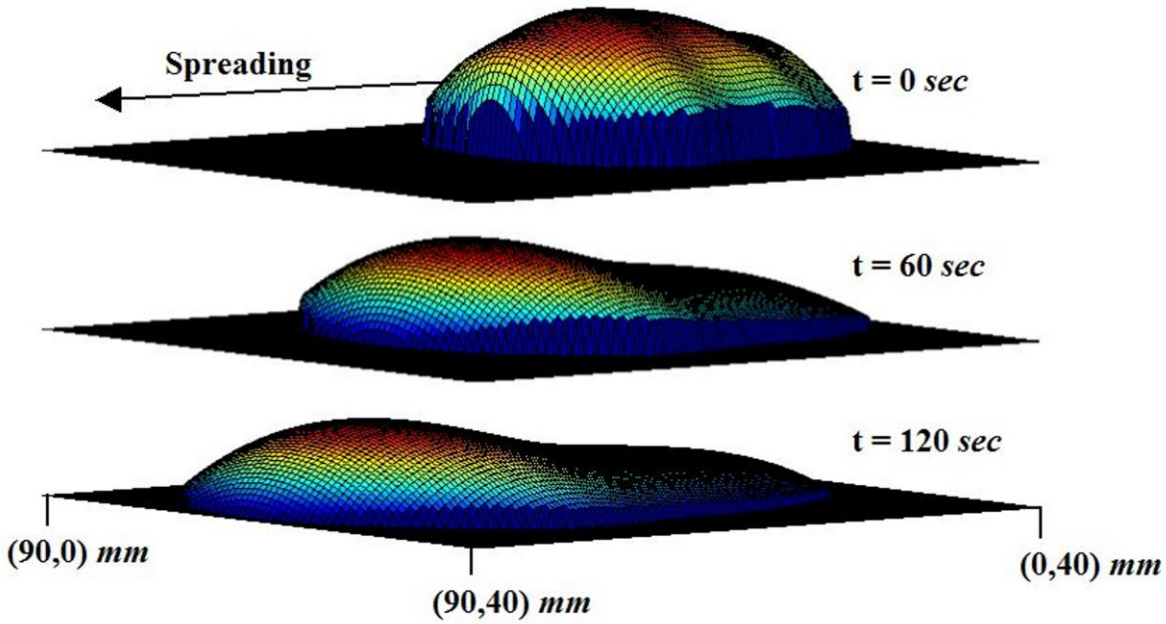

Figure 3.9. Isometric views of the evolution of the digital surface topographies of a spreading experiments at t = 0, 60 and 120 *seconds* (RUN1).

There are three main limitations for this technique for reconstructing the surface topography of a finite bolus of fluid. The first limitation stems from the fact that each point in space (*x,y)* will have one height value *h(x,y).* If the experimental gel has any fluid collapsing on itself (Figure 3.10), the method presented would not capture that complexity.

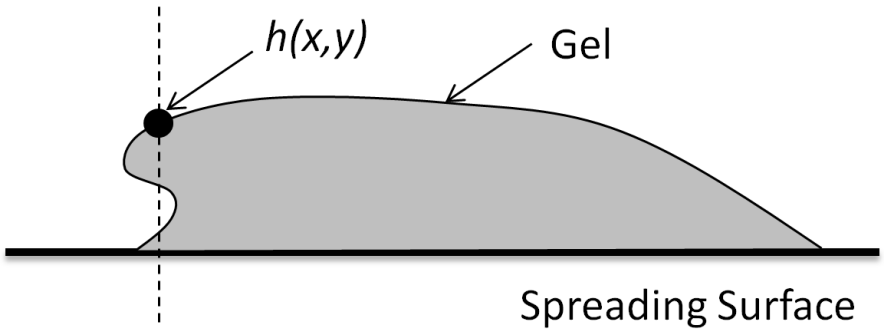

Figure 3.10. Cartoon showing an example of a fluid edge that would not be appropriately captured with the method described in this document.

The second limitation of this technique is that as the leading edge of the fluid becomes very thin, the side view of the gel, seen in the camera, might have low visibility. This does not pose a problem for obtaining bolus dimensions because they are available in the top view, but reconstructing the topography of the trailing edge could be problematic. Finally, the fact that the cross-section along the lateral plane is approximated using a standard function (Eq. (3.1)), with known width dimensions, is clearly a disadvantage to methods that don't make this assumption. Nevertheless, the width and height of the cross-section are measured experimentally and the fact that the resulting volume of the fluid matches the experiment suggests that the 4^{th} order estimate for the lateral cross section is close to the actual cross section.

Two other realistic methods for reconstructing the surface: approximating fluorescent intensities [44, 45] and tracking projected image deformation of the fluid surface [30, 46, 47] will not provide solutions to the first two limitations. Nevertheless, for future work it might be advantageous to use the fluorescent technique [44, 45] because it is more of a measure of the topography, as opposed to an approximation resulting from reconstructing the topography from the cross-sections.

Conclusion

In this chapter I present a new repeatable technique for automatically dispensing a finite mass of fluid that is free to spread down an incline without contact with any other surface. This dispensing technique enables me to control the rate at which the fluid is applied to a spreading surface in a controlled environment, allowing the researcher to experiment with different spreading surfaces and examine how the initial release of the gel might impact spreading.

In addition, I present a new automated image analysis procedure using LabVIEW to measure the spreading dimensions and approximate surface topography of a free surface, finite bolus of fluid with spatial accuracy within 0.5%. This is especially useful for verifying numerical simulations of free surface flow and can be used to quantify surface area coverage of a microbicide delivery vehicle as a function of time. The non-invasiveness of this image analysis technique allows for accurate measurements of polymeric fluid that is spreading in a controlled environment and on any surface (e.g. hydrophilic, hydrophobic, epithelium tissue, etc.). The method and apparatus described here is ideal for finite samples of viscous polymeric liquids and slurries studied in drug delivery, geophysical fluid flow, and non-Newtonian fluid dynamics.

The instrument and image analysis technique presented here achieves the engineering goal of this chapter and completes the first objective of this dissertation. I completed a total of 9 spreading experiments on HEC gels by testing 2.4%, 2.7% and 3.0% HEC gels in triplicate. Gels with lower concentrations of HEC spread more in the axial directions, but diffused less in the lateral direction. This limited diffusion might be explained by surface tension, which should be investigated in future studies. The surface topography of each experiment was used as the initial condition of each corresponding computational simulation. Finally, the spreading data obtained from each experiment was used to validate the power-law (Chapter 5) and Ellis (Chapter 6) numerical models.

Chapter 4 DEVELOPING A COMPUTATIONAL SPREADING SIMULATION

Introduction

The dynamics of avalanching masses of fluid are extensively studied in countless disciplines, including biomechanics, and are essential to achieving our group's long-term goal of developing a microbicide delivery vehicle. This chapter will outline the numerical solution that will be used to meet the second overall objective of this project: to develop a numerical model of a non-Newtonian fluid, spreading in 3-D, due to gravity.

Significance and Chapter Goals

Modeling fluid flow usually begins by solving a momentum equation in conjunction with the conservation of mass. In order to simplify the momentum equation, when relevant, many studies implement the *lubrication approximation* [30, 50] allowing for the inertial terms to be neglected. Originally, models that employed lubrication approximations were restricted to Newtonian fluids [30], but researchers have expanded this field of study by incorporating different constitutive equations such as Bingham, Herschel-Bulkley, power-law, Ellis, O'ldroyd-B and even some viscoelastic models [51]. **In this document, one of my objectives is to focus on numerical modeling of a finite volume of fluid being driven by gravity and Newtonian viscous forces. In the subsequent chapters, I aim to incorporate non-Newtonian viscous**

forces, and compare the spreading characteristics derived from the numerical model with the spreading characteristics measured experimentally to investigate how:

a. Sophistication of the constitutive equation that incorporates viscous forces affects the model's spreading accuracy.

b. Matching the model's initial condition with the experiments initial condition affects the model's spreading accuracy.

This chapter will outline the derivation and numerical solution of the 3-D evolution equation for a Newtonian fluid. The foundation for this derivation was adopted from an existing 2-D model [3, 4]. Presented here is a mathematical model that simulates a finite bolus of Newtonian fluid coating an inclined surface. The fluid is analyzed using the Navier-Stokes Equation to develop a differential equation for the evolution of the height of the fluid as a function of time and space in the *x* and *y* direction, $h(x,y,t)$ (Figure 4.1). The evolution equation will then mathematically describe the motion of the fluid's surface, while incorporating the viscous properties of the fluid and gravitational perturbation force acting on it.

Figure 4.1 shows the coordinate system diagram of the problem statement, analyzing spreading in 2-dimensions (*x* and *y*). In the remainder of this work, spreading in the *x*-direction will be referred to as axial and spreading in the *y*-direction will be referred to as lateral.

OBJECTIVE 2: Develop a 3-D numerical model to simulate the free surface, gravity-induced spreading of a thin-film of a Newtonian fluid, to be used in Objectives 3 and 4 for non-Newtonian fluids.

The engineering goal of this objective is to develop an original code for solving a non-linear, second order PDE that governs viscous, gravity-driven flow of a finite volume of Newtonian fluid with a free surface in 3-D. This numerical code should: (1) obtain mesh

convergence in axial and lateral direction; (2) conserve volume within 0.001%; (3) be easy to upgrade for power-law and Ellis constitutive equations.

This chapter's work may not have a defensive novel contribution. It is intended to provide a foundation and validation for numerical code (described in subsequent chapters) that simulates non-Newtonian free surface flow, which is original and is intended for publication.

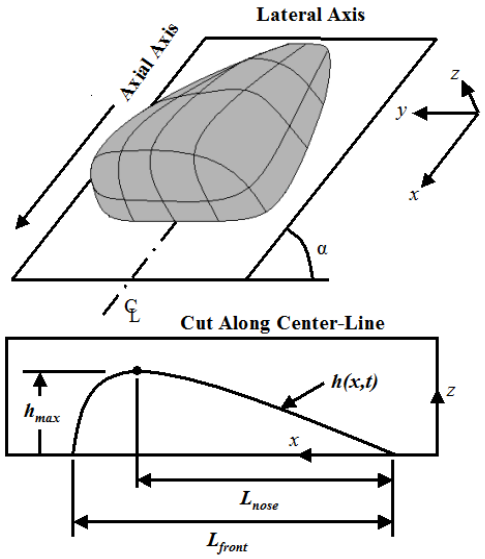

Figure 4.1. Coordinate System of the Problem Statement. Spreading surface is inclined to spread in the axial direction, and slumping is defined in the lateral direction.

Review of Relevant Literature:

There is a rich body of literature on gravity-induced flow. The following focused review of relevant literature is intended to give a general background of the type of modeling that has been done for Newtonian and non-Newtonian fluids being perturbed by gravity. All of the mentioned literature implements the thin-film approximation along with one of four viscous models (Newtonian, Bingham, power-law, Ellis), which I considered to be most relevant to the current objective. There have been several review articles outlining various models for coating flows of non-Newtonian fluids [20, 51, 52], but they rarely consider flow in multiple dimensions

or finite volume flow. Craster *et al.* primarily discuss finite volume flow papers with stability issues resulting from surface tension that don't address viscous relationships relevant to this document [53]. Ancey *et al.* allude to several articles that address finite geophysical flow with viscoplastic constitutive properties, which serve as a useful reference, but that work does not meet the current objectives because they focus on yield stress in the material [54].

Numerical and Analytical modeling of Newtonian flow

A natural starting point for modeling the flow of polymeric liquids is to start with a basic 2-D Newtonian simulation of a free surface, gravity-induced flow of a finite volume (Figure 4.1). The non-linear partial differential equation governing Newtonian flow (Newtonian evolution equation derived later in this chapter) can be solved approximately in 1-D of spreading, using a similarity solution, with acceptable experimental agreement [55]. However, to fully solve the evolution equation and to develop techniques capable of incorporating non-linear viscometric relationships, 2-D and 3-D numerical solutions have been introduced [49, 56-60].

Harlow *et al.* developed a finite-difference, explicit method for numerically simulating a dam breaking problem, using a Newtonian fluid [61]. This paper was one of the first to analyze free surface flow numerically, concluding that this method could be improved upon to account for different problem configurations.

Kondic *et al.* have documented a finite-difference method for solving a fourth-order PDE describing the time evolution of a free surface of a Newtonian fluids being perturbed by gravity [62]. In most cases they use a configuration with an infinite source of fluid (constant-flux), for a Newtonian liquid under the influence of viscous, capillary and gravity forces [56, 58]. Recent publications give a thorough outline of a numerical method so robust that incorporating non-

linear viscometric data or any other driving forces is straightforward [62]. While the numerical method being presented in this paper has its own unique attributes, many space and time discretization ideas were adopted from this article.

Originally I tried solving the evolution PDE using an Alternate Direction Implicit (ADI) scheme [49, 60, 63, 64], resulting in irresolvable problems with space convergence and volume conservation. As a result, I adopted the numerical scheme outlined in this chapter.

Numerical and Analytical modeling of viscoplastic flow

Most geophysical flows are modeled as Bingham or Herschel-Bulkley viscoplastic materials, which typically behave as a single-phase fluid that obey Newtonian (Bingham) or power-law (Herschel-Bulkley) viscous deformation in areas that have exceeded a yield stress [54, 65]. The Herschel-Bulkley constitutive equation is a commonly used stress versus shear ratemodel for viscoplastic flow [51, 54], which can be reduced to the power-law at the limit of no yield stress. There are two primary reasons for why this rich body of literature is seldom applicable to the objectives of this document: (1) researchers modeling viscoplastic flow are rarely interested in shear-thinning effects, and mostly focus their research on how yield stress impacts flow characteristics [66-68], and (2) most viscoplastic models are trying to simulate source-flow [69-71] instead of a finite volume due to the nature of their problem, and in some cases use channel-like geometry instead of flat plate [66].

Fluids that contain a yield stress could potentially be a very useful tool when developing a vaginal delivery vehicle, as discussed in Chapter 7. Quantifying the interdependence of the two power-law parameters and their impact on spreading is challenging enough, and could be done

using a Herschel-Bulkley code with zero yield stress, but adding a third yield stress parameter complicates the problem even further.

Huang and Garcia [72] conducted preliminary studies of power-law parameters and their impact on the free surface and flow characteristics, for a Hershel-Bulkley fluid. They combined asymptotic solutions for the inner and outer surface, for spreading at a relatively steep slope. Most of the results and conclusions reached in that study were targeted for fluid that contains a yield stress. Some aspects of the sensitivity analysis focused on the impact of the shear-thinning of the fluid. They inevitably reached the common conclusion that as a fluid becomes more shear-thinning; it does not spread as far in a given time. This was, however, the extent of the shear-thinning sensitivity analysis. They found that, when incorporating a yield stress, shear-thinning does not have a considerable impact on spreading at early time stages, but does have great impact at later times. An important limitation to note is that this and most Hershel-Bulkley studies are intended to simulate large scale flows (e.g. volcanic), therefore small scale flows are outside the scope of the work done by Haung and Garcia [72] and most previous papers that investigate fluids with a yield stress.

Balmforth *et al*. [29] have presented a discussion on the effect of shear-thinning and yield stress on spreading characteristics for symmetric extrusions on horizontal plates. They found that in a given time, the extrusion would spread further as the shear-thinning index approached unity.

Balmforth *et al.* has published a Herschel-Bulkley fluid numerical, Alternate Direction Implicit (ADI) scheme, spreading model of a free surface, finite volume bolus, where they even attempted to roughly match the initial conditions of an experiment to compare flow characteristics [68]. They also experimented with different initial condition configurations to conclude that the initial condition is a driving force in flow characteristics, even in cases where

volume is the same [28, 68]. It is noteworthy that they reached this conclusion based on the fluid's surface ridges not being able to overcome yield stress, but I believe the same conclusion would be reached for fluids that don't have a yield stress because the fluxes in the evolution equation are functions of the gradients of the surface curvature [49]. The performance of the numerical method used in these papers was not extensively documented. When trying to replicate that method for a power-law fluid, I encountered problems with convergence and volume conservation, and chose to use a direct Newton's method [49], which resolved the aforementioned issues.

Sutalo *et al.* introduced a sophisticated computational fluid dynamic (CFD) simulations of constant-flux viscoplastic flow spreading from one incline to another, until it eventually coats four inclines [71]. To incorporate non-Newtonian effects, they used the Herschel-Bulkley constitutive equation, with rheological parameters obtained from viscometric analysis of three gels. Very similar to the objectives of this document, in order to confirm their numerical model they compared spreading data of the three gels to the solution of the numerical method. They found that the numerical simulation agreed with the experiment for the first incline, but not for the other three. Most importantly, they documented a parameter study of the power-law variables of the Herschel-Bulkley constitutive equation, and showed that they changed spreading characteristics in agreement with the experiment [71]. Otherwise their problem statement was not applicable to this objective because they used an infinite source and only calculated for one-dimension of spreading.

Numerical and Analytical modeling of power-law flow

In an effort to mathematically represent any non-linearity in the stress-shear rate relationship, the power-law constitutive equation has been used in models that that utilize the lubrication approximation [20]. Its appeal is that it is able to account for shear-thinning behavior, but it is limited in the fact that it can't describe Newtonian plateaus observed with most polymeric fluids [20, 24]. Because the terms in the power-law constitutive equation can be mathematically and explicitly manipulated, it is straightforward to implement it into a derivation of a second-order, non-linear PDE that governs the evolution of a fluid being perturbed by gravity and viscous forces.

Using an evolution equation that is slightly different than the one derived in this paper, Gratton and Perazzo developed approximate analytical solutions for different geometry configurations [73], including a finite volume of a fluid that is spreading on an incline in one-dimension [74]. Only considering nearly horizontal or vertical inclines, the evolution equation was approximated as an initial value problem, which was solved using the method of characteristics. This analysis was limited to modeling the free surface from the trailing edge to the nose ("outer edge" defined in [72]), and can't be applied to most engineering problems. This analysis showed that the shear-thinning index, in the power-law constitutive equation, has a major effect on the outer edge of the free surface, but this is not enough information to conclude the shear-thinning indexes impact on spreading characteristics [74].

In 1999, Gratton *et al.* analytically solved the evolution PDE, using a similarity solution, to show that the spreading of a finite-volume on a horizontal surface will have good agreement with experiment [52]. Other approximate solutions are usually also limited to a horizontal plane

[75, 76]. A free surface solution of a power-law fluid spreading on an extremely angled incline was developed using an approximate self-similar solution of the evolution PDE [77].

Haeri *et al.* conducted 3-D numerical and experimental studies on the falling flow of power-law films [78]. An open source CFD package using a "volume of fluid" numerical method was implemented to solve the continuity and momentum equations, for the velocity vectors, in a domain that included both the spreading fluid and the surrounding air. The free surface was found by applying an algorithm to distinguish between the fluid and air. The study accounted for power-law viscous forces and surface tension. A contact angle measurement was utilized to account for the interaction between the spreading surface and fluid. The method presented in this document eliminates the need for a fluid-solid interface search algorithm by deriving and solving for the fluid height directly.

In Chapter 5 I will present the derivation of a second-order, non-linear PDE, governing the 3-D motion of a finite bolus of power-law fluid, spreading under the influence of gravity and viscous forces. The 3-D power-law model is an expansion of Kieweg's previously published PDE governing spreading of a power-law fluid in 2-dimensions [3]. Kieweg's numerical solution tended to overshoot the experimental spreading in the axial direction. This may be because the model did not account for lateral spreading in the 3rd direction. Alternately, it may also reflect other assumptions/limitations, such as the power-law constitutive equation.

The completion of Objective 3 (in Chapter 5) is necessary because it will allow me to see if the power-law model is a good predictor for HEC spreading characteristics. This simulation will also allow me to perform detailed sensitivity analysis to expose the interdependence of the power-law parameters, inclination angle and axial spreading. Finally, I will test if incorporating a

detailed topography of the initial condition results in a more accurate numerical model, when compared with an approximate topography.

Numerical and Analytical modeling of Ellis flow

The Ellis constitutive equation complicates the derivation of the evolution equation by adding a third parameter. This allows the constitutive equation to describe the low shear rate Newtonian plateau of the HEC rheological data, giving it a clear advantage over the power-law [20, 79]. Its limitation is that it can't fit with the second plateau at high shear rates [20], which does not apply to this work because the low shear rate region is of principal interest. This leads to the conclusion that the Ellis model is a good option for modeling the viscous behavior of HEC gels.

There is very limited literature on integrating the Ellis constitutive equation into an evolution equation describing free surface flow. Weinder and Schwartz derived an analytical expression for the velocity of an Ellis fluid edge, when spreading on a completely vertical surface (with surface tension) [80]. They also completely derived an evolution equation that can't be applied to the current objective because it does not account for a surface inclination angle or spreading in the lateral direction.

Schwartz and Eley developed a 3-D numerical ADI scheme to simulate the spreading of a shear-thinning fluid, and compared it with an experiment [30]. Even though the fluid could have been characterized well with an Ellis model, they developed a method to use the tabulated experimental rheological data to avoid deriving the evolution equation with Ellis viscous forces. The other studies that I found implementing the Ellis constitutive equation never solve for the evolution of a free surface [25, 81].

Thus, there are no known publications describing the derivation and solution of a PDE that governs gravity-induced, free surface flow of an Ellis fluid.

Chapter 6 presents the derivation of a second-order, non-linear PDE, governing the 3-D motion of a finite bolus of Ellis fluid, spreading under the influence of gravity and viscous forces. I will also present sensitivity analysis to suggest how the three parameters of the Ellis constitutive equation influence axial spreading.

The completion of Objective 4 (in Chapter 6) is necessary because it will produce an original numerical study of gravity-induced spreading of a finite volume of fluid characterized with an Ellis constitutive equation. I will show if using the more complicated Ellis constitutive equation results in an improvement over the power-law constitutive equation, when using a numerical model to simulate gravity-induced HEC spreading. I will also present a sensitivity analysis of the Ellis parameters and discuss how the method of obtaining those parameters could considerably influence the efficacy of the simulation.

In this chapter I will derive the Newtonian evolution equation and describe the numerical method used to solve this equation. This numerical simulation will also be used as a basis for solving more complicated non-Newtonian models in Chapter 5 and 6.

Methods

The Navier-Stokes Equation (Eq. (4.1)) where $\tilde{v}$ and $\tilde{g}$ are the velocity and gravity vectors respectively, p is the hydrostatic pressure, μ is the viscosity and ρ is the density, is utilized as the governing equation of motion.

$$\frac{d\tilde{v}}{dt} + (\tilde{v} \cdot \nabla)\tilde{v} = -\frac{1}{\rho}\nabla p + \frac{1}{\rho}\mu \cdot \nabla^2 \tilde{v} + \tilde{g} \qquad (4.1)$$

The velocity vector $\tilde{v}$ is broken down into its Cartesian coordinates: *u, v, w* in the *x, y, z* directions respectively.

1. **Thin-film (lubrication) approximation:** We start by assuming that throughout the simulation, the characteristic height, *H* (maximum thickness along the *x*-*z* plane) of the gel is considerably larger than the characteristic length, *L* (measured from the trailing to the leading edge along the *x*-axis), and *T* is the characteristic time (Eq. (4.2)).

$$H << L \text{ and } \frac{\rho H^2}{\mu T} << 1 \qquad (4.2)$$

$$\left(\frac{\rho U L}{\mu}\right)\left(\frac{H}{L}\right)^2 << 1 \qquad (4.3) \text{ [50]}$$

Eq. (4.3) is the characteristic Reynolds number [50], where *U* is the characteristic velocity. With both conditions (Eq. (4.2) and (4.3)) satisfied [50], using the lubrication approximation is justified [50]. The reasoning for this is explained in greater detail in Appendix A1. Even though the Reynolds number does not necessarily have to be small to implement the thin-film approximation, it generally will be for the simulations presented in this document. Kieweg estimated worst-case scenarios of Reynolds number for extreme conditions of flow, for gels similar to ours, and found that the largest values are on the order of 10^{-2} to 10^{-4} [3]. Therefore, I conclude that viscous forces dominate and omit the inertial terms in Eq. (4.1) following the lubrication approximation.

2. **No slip assumption:** Here we assume that there is no slip between the gel and the spreading surface, which leads us to the following boundary condition:
    a. Boundary Condition 1: $u(z = 0) = v(z = 0) = 0$
3. **Free surface assumption:** Here we assume that the surface of the gel, which is exposed to the air, is not experiencing any stress and is subjected to ambient pressure.
    a. Boundary Condition 2: at $z = h(x,y,t) \rightarrow \ \tau_{zx} = \tau_{zy} = 0$
    b. Boundary Condition 3: at $z = h(x,y,t) \rightarrow \ p = p_o$

    After implementing the first three assumptions, the momentum equation (Eq. (4.1)) is reduced to three governing equations of motion (Eq. (4.4)-(4.6)) where α is the angle of the ramp with respect to the horizontal plane (Figure 4.1).

$$\text{x-direction: } 0 = -\frac{dp}{dx} + \mu\frac{d^2u}{dz^2} + \rho g \sin\alpha \tag{4.4}$$

$$\text{y-direction: } 0 = -\frac{dp}{dy} + \mu\frac{d^2v}{dz^2} \tag{4.5}$$

$$\text{z-direction: } 0 = -\frac{dp}{dz} - \rho g \cos\alpha \tag{4.6}$$

Using Eq. (4.4)-(4.6) along with the first boundary condition, I arrive at the velocity profiles in the axial (Eq. (4.11)) and lateral (Eq. (4.12)) directions.

$$u = \left(\frac{1}{3\mu}\right)\left(\frac{dp}{dx} - \rho g \sin\alpha\right)\left[z - h(x,y,t)\right] \tag{4.7}$$

$$v = \left(\frac{1}{3\mu}\right)\left(\frac{dp}{dy}\right)\left[z - h(x,y,t)\right] \tag{4.8}$$

The flow rate per unit width in the axial (q_x) and lateral (q_y) directions, is then found using Eq. (4.9). Integrating the equation of motion in the *z* direction, and incorporating the third boundary condition, I arrive at an expression for pressure (Eq. (4.10)).

$$q_x = \int_0^{h(x.y.t)} u(x,y,t)\, dz \qquad\qquad q_y = \int_0^{h(x.y.t)} v(x,y,t)\, dz \tag{4.9}$$

$$p = [\rho g \cos\alpha][h(x,y,t) - z] + p_o \tag{4.10}$$

Incorporating pressure (Eq.(4.10)) and using the flow rates in the axial and lateral (Eq. (4.9)) directions, substituted into the conservation of mass (Eq. (4.13)), I arrive at the non-linear partial differential equation. This equation describes the evolution of the free surface, and thus called the "evolution equation".

$$q_x = -\left(\frac{\rho g}{3\mu}\right)\left(\frac{dh}{dx}\cos\alpha - \sin\alpha\right)h^3 \tag{4.11}$$

$$q_y = -\left(\frac{\rho g}{3\mu}\right)\left(\frac{dh}{dy}\cos\alpha\right)h^3 \tag{4.12}$$

$$\frac{dh(x,y,t)}{dt} + \frac{dq_x}{dx} + \frac{dq_y}{dy} = 0 \tag{4.13}$$ [62, 74]

Numerical Solution of Evolution Equation

Discretization in Space:

The free surface evolution equations (Eq. (4.13)) was solved for *h(x,y,t)* using Newton's method written in the C programming language. The domain is the rectangular spreading surface (Figure 4.1), broken down into a finite number of grid points, that can be set to any dimensions.

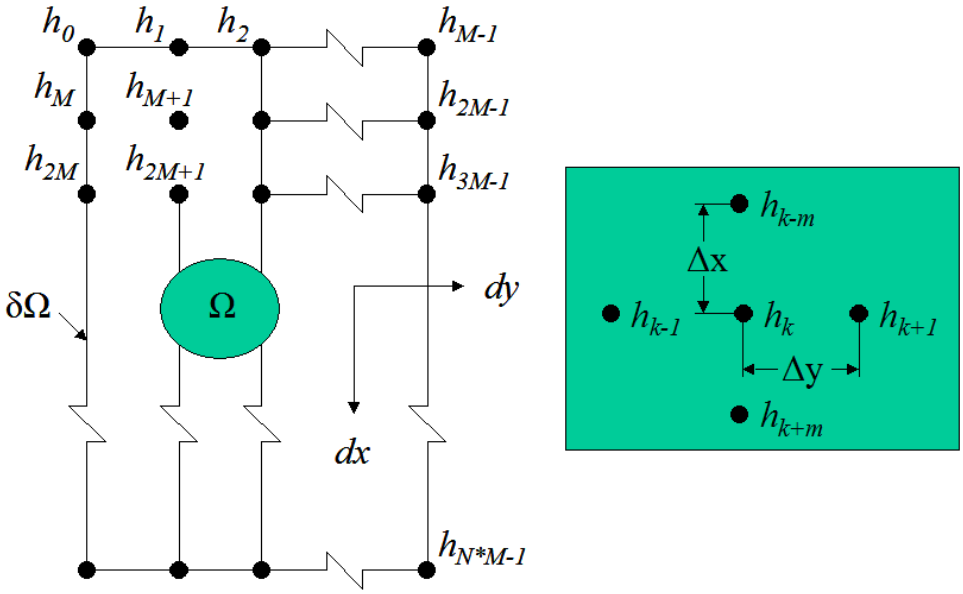

Figure 4.2. Domain for the numerical method divided into TOT points.

The surface is defined by $0 \le x \le L$ and $0 \le y \le W$, which is divided into rectangular cells, $TOT = N \times M$, in the x and y directions respectively. The user-defined cell dimensions are Δx and Δy in the x and y-directions, respectively, and are not necessarily equal to each other (Eq. (4.14)).

$$x_{i+1} = x_i + \Delta x \qquad\qquad y_{i+1} = y_i + \Delta y \qquad\qquad (4.14)$$

Because the value of any point that is not covered by the fluid is zero, the values on the boundary of the domain, $\partial\Omega$, were also fixed at zero. It is important to point out that the code is not written to have a distinct boundary. Instead of setting a boundary that will be big enough to accommodate the spreading fluid, this code is designed to expand the boundary immediately ahead of the fluid. This prevents the code from solving for any points on the boundary that are not expected to contain fluid in the next time step, resulting in a code that requires less memory and less computation time.

The main evolution equation (Eq. (4.13)) will be discretized in space using the central difference approximation (Eq. (4.15)).

$$\frac{dh(x,y,t)}{dt} + K\left(\frac{q_{(x)k+m/2} - q_{(x)k-m/2}}{\Delta x} + \frac{q_{(y)k+1/2} - q_{(y)k-1/2}}{\Delta y}\right) = 0 \tag{4.15}$$

where: $K = \frac{\rho g}{3\mu}$.

The fluxes will be discretized using central differences (Eq. (4.16)-(4.19)), centered about the node interfaces. After experimenting with different methods of discretizing the diffusion term, h^3, I found that a discretization suggested by Diaz and Kondic [62] resulted in the fastest computation time.

$$q_{(x)k+m/2} = -\left(\left(\frac{h_{k+m} - h_k}{\Delta x}\right)\cos\alpha - \sin\alpha\right)\left[\frac{1}{2}\left(h_k^3 + h_{k+m}^3\right)\right] \tag{4.16}$$

$$q_{(x)k-m/2} = -\left(\left(\frac{h_k - h_{k-m}}{\Delta x}\right)\cos\alpha - \sin\alpha\right)\left[\frac{1}{2}\left(h_k^3 + h_{k-m}^3\right)\right] \tag{4.17}$$

$$q_{(y)k+1/2} = -\left(\left(\frac{h_{k+1} - h_k}{\Delta y}\right)\cos\alpha\right)\left[\frac{1}{2}\left(h_k^3 + h_{k+1}^3\right)\right] \tag{4.18}$$

$$q_{(y)k-1/2} = -\left(\left(\frac{h_k - h_{k-1}}{\Delta y}\right)\cos\alpha\right)\left[\frac{1}{2}\left(h_k^3 + h_{k-1}^3\right)\right] \tag{4.19}$$

Discretization in Time:

Defining the free surface height as a function of space and time as $h(x,y,t^n)$ can be simplified numerically as h_k^n, where the superscript, *n*, denotes the time step. The superscript *n+1* symbolizes the solution at the next time step (variable being solved for). The Θ-method [62, 63] is a time discretization scheme (Eq. (4.20)), where θ = ½ results in an implicit, second-order accurate Crank-Nicolson scheme.

$$\frac{h_k^{n+1} - h_k^n}{dt} + \theta\, f_k^{n+1} + (1-\theta)\, f_k^n = 0 \tag{4.20}$$

Using any other value for θ that is greater than zero also results in an implicit scheme that is first-order accurate.

Solving the non-linear system of equations:

Applying Eq. (4.15) and (4.20) to the domain will result in *TOT* non-linear equations with *TOT* unknowns (Eq. (4.21)), where the superscript *n* represents the time step and the subscript *k* is the point in space.

.

$$F_k(h_k^{n+1}, h_{k+1}^{n+1}, h_{k-1}^{n+1}, h_{k+M}^{n+1}, h_{k-M}^{n+1}) = 0 \text{ for } (0 \le \text{k} \le \text{TOT-1}) \tag{4.21}$$

Newton's method can be used to transform the system of non-linear equations into a linear system (Eq. (4.22)) [82], where h^z is a guess and $z+1$ is an improvement of the guess. The derivative matrix is the Jacobian [*J*], which is a sparse matrix with at most five non-zero elements in each row.

$$\begin{bmatrix} \frac{dF_0}{dh_0^z} & \cdots & \frac{dF_0}{dh_{TOT-1}^z} \\ \vdots & \ddots & \vdots \\ \frac{dF_{TOT-1}}{dh_0^z} & \cdots & \frac{dF_{TOT-1}}{dh_{TOT-1}^z} \end{bmatrix} \begin{Bmatrix} h_0^{z+1} - h_0^z \\ \vdots \\ h_{TOT-1}^{z+1} - h_{TOT-1}^z \end{Bmatrix} = - \begin{Bmatrix} F(h_0^z) \\ \vdots \\ F(h_{TOT-1}^z) \end{Bmatrix} \tag{4.22}$$

For any good initial guess, Newton's method can be expected to converge rapidly by iteratively solving linear systems until a suitable error is reached [64, 82]. The linear system (Eq. (4.22)) can be solved using iterative and direct methods [83], but iterative methods are generally more appealing for large, sparse systems. This iterative method is especially efficient for sparse systems because its computational procedure only requires matrix-vector multiplication, making the code for banded matrices straight forward. The Conjugate Gradient method is a widely used iterative method, which is able to solve symmetric and positive definite systems [83, 84]. The system presented in this document is not symmetric but is positive definite, therefore I used the BiConjugate Gradient Method (BiCG), a slight variation of the conjugate gradient method [83], to obtain an iterative solution.

A preconditioner can be used to accelerate the convergence [83] of iterative methods. Both sides of Eq. (4.22) can be multiplied by a matrix [*M*], which should be chosen to make the left hand side of the equation as close to an identity matrix as possible [83, 84]. If the inverse of [*J*] were known, then using it as the preconditioner would result in a solved system, but because this matrix is not known a preconditioner can be an approximation of $[J]^{-1}$. In this model an incomplete LU (ILU) factorization is performed on the Jacobian matrix, for every iteration of Newton's method, and is used as the preconditioner matrix [83].

The BiCG method is set to iterate until the first norm of the residuals, defined as $\varepsilon_{\mathbf{B}iCG}$, falls below 10^{-6}. The first norm of the height change, resulting from each Newton's iteration, $\varepsilon_{NEWT} = \max \sum_{i=0}^{N-1} h_{i,\, newiteration} - h_{i,\, olditeration}$, is used as the check for Newton's method convergence. Once the first norm of the height change falls below 10^{-10}, Newton's method iteration is terminated and a solution for the new time step is accepted.

In the event that either Newton's method or BiCG method will not converge within a user-defined number of iterations, the time step, *dt*, is decreased and Newton's method is repeated.

A final note is that all numerical simulations were carried out on an Information and Telecommunication Technology Center (ITTC) cluster allowing me to run multiple computations at one time.

Results:

Code Validation:

I confirmed that the code results in reproducible spreading in both the axial and lateral direction, and the maximum height of the bolus does not grow. An excellent check of the accuracy of the solution is validating that the conservation of mass is not violated (volume stays constant) [62]. If mass is completely conserved, then the area under the surface of the fluid should never change in time (Eq. (4.23)). During each simulation, volume is monitored to confirm mass conservation was maintained within 0.001% for the entire simulation. The main shortcoming of the ADI scheme that I originally used to solve this problem was that it accumulated truncation error, and the volume would gradually decrease.

$$\frac{\partial}{\partial t}\iint_{\Omega} h(x,y,t)\,dx\,dy = 0 \tag{4.23}$$

All simulations for code validation and convergence study purposes were carried out on a 5 x 1.8 cm domain (prior to introducing space-adaptation), in the *x* and *y* direction respectively. The angle of inclination was set at 30°. The initial condition was a discretized dome shape

calculated using the equation: $h = -x^2 - y^2 + h_{o(\max)}$. Figure 4.3 shows a typical bolus initial condition.

Another useful check for a numerical solution is to compare it with a known analytical solution, which has been presented by Huppert [55]. I show this comparison in later chapters for non-Newtonian constitutive equations and verify that they simplify to the Huppert solution for the Newtonian case.

Each simulation in this validating study was run for up to 5 seconds of spreading. The time step was originally set to: $dt = 10^{-5}$, but the code was written to dynamically adapt time in case Newton's method or the BiCG method could not converge. In most cases this was not necessary.

A singularity might arise from the fact that a numerical simulation solves for a propagating contact line, while restricted under the no-slip boundary condition. This is not problematic for our solution because the movement of the contact line can be driven by any point that is not at $z = 0$. The axial spreading of the fluid is interpreted as tractor treads rolling along on a surface [85]. To preserve the positivity of the solution, any point that became negative during numerical calculations (typically immediately ahead of the leading edge) was forced to zero.

Often, a precursor is used in thin film simulations to handle the singularity when surface tension effects (4^{th} order derivatives) are included (e.g., Ref [62, 72, 86, 87]). While this has no physical meaning, I originally ran my code with a precursor positivity preserving method, using a constant thin film of $d = 10^{-3}$ *cm*. After a brief study, I found little difference in spreading characteristics when comparing the two positivity-preserving techniques and both simulations conserved volume. However, a solution with the forced positivity technique, rather than the

precursor method, was a slightly better comparison with the similarity solution. Most importantly, using a precursor film caused a sufficient lag in computational efficiency. Thus I chose the forced method rather than the precursor method to use in all simulations presented in this dissertation.

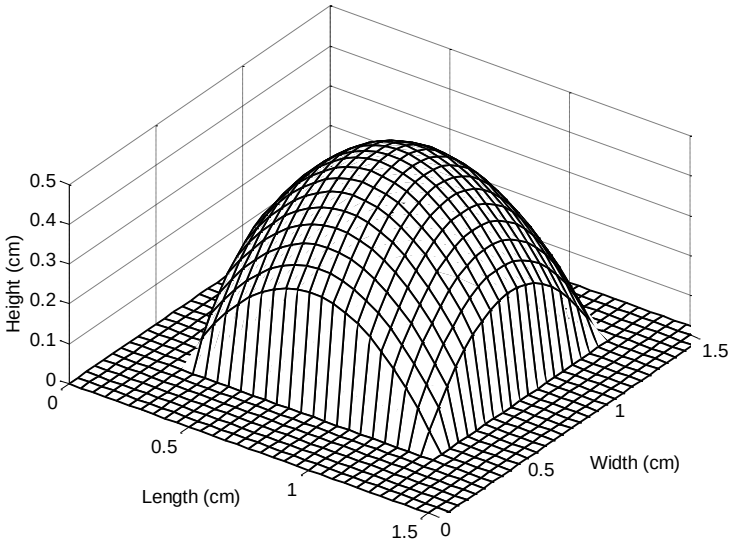

Figure 4.3. 1 x 1 cm bolus of fluid used as an initial condition for simulations validating mass conservation and used to validate non-Newtonian models introduced in subsequent chapters. Input Parameters: ($\alpha = 30°$, $\Delta x = 0.01$, $\Delta y = 0.01$, Δt – adapted, $\mu = 500$ Poise, $\varepsilon_{NEWT} = 10^{-10}$, $\varepsilon_{BiCG} = 10^{-6}$)

Spreading characteristics of the fluid analyzed using this code appeared to have a familiar and expected shape, formerly seen in previous studies and papers related to this work [3]. Because of the inclination of the spreading surface, the length, *L* (in the *x*-direction), of the fluid increased at a higher rate than the width, *W* (in the *y*-direction) (Figure 4.4) as expected. Results show that the leading edge of the fluid spreads in both directions, but because spreading in the lateral direction is only a result of the weight of the fluid collapsing on itself (slumping), lateral spreading decreases along with the maximum thickness. The spreading in the axial direction is

also happening as a result of the fluid collapse, but flow downhill causes spreading to dominate in the axial direction.

Figure 4.5 shows a typical evolution of the free surface, for as fluid spreading on an incline. As code validation, a simulation was run at a zero inclination angle and spreading was uniform in all directions as expected. Another technique used to validate the code and accuracy of the solutions was to verify that mass is being conserved throughout the simulation. In the five seconds of spreading, there was absolutely no change to the fluid's volume, which was calculated using a Riemann's Sum technique [64].

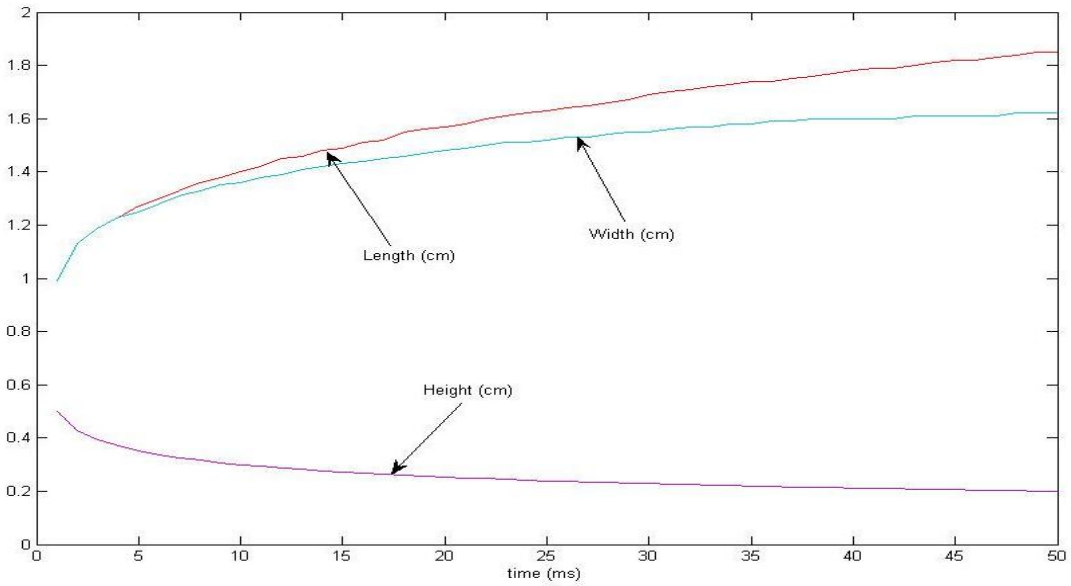

Figure 4.4. Spreading Characteristics of a Spreading Bolus of Newtonian Fluid Input Parameters: ($\alpha = 30°$, $\Delta x = 0.01$, $\Delta y = 0.01$, Δt – adapted, $\mu = 100$ Poise, $\varepsilon_{NEWT} = 10^{-10}$, $\varepsilon_{BiCG} = 10^{-6}$)

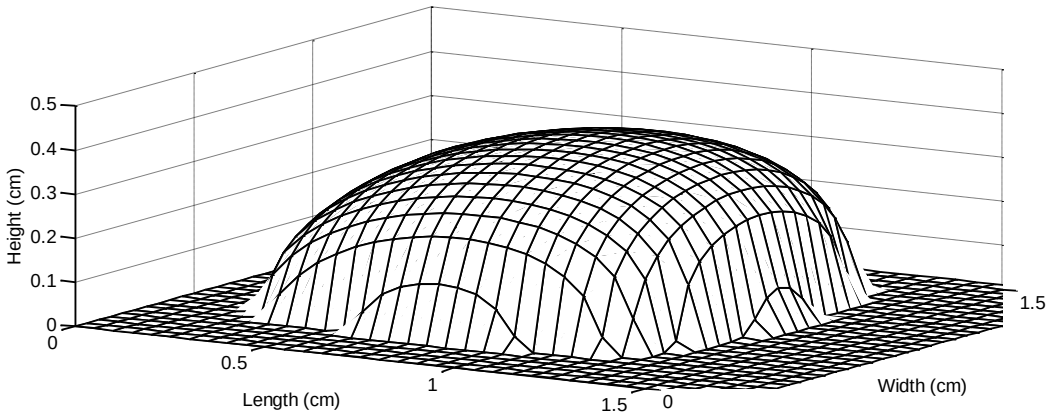

Figure 4.5. Spreading Profile of a bolus presented in Figure 4.3 after 1 second of spreading. Input Parameters: ($\alpha = 30°$, $\Delta x = 0.01$, $\Delta y = 0.01$, Δt – adapted, $\mu = 500$ Poise, $\varepsilon_{NEWT} = 10^{-10}$, $\varepsilon_{BiCG} = 10^{-6}$)

Mesh Convergence:

A convergence study was completed to determine if the solution converged with refined spatial discretization. Figures 4.6 and 4.7 show case studies to investigate how changing the mesh affected the spreading characteristics of a fluid with all other parameters kept constant.

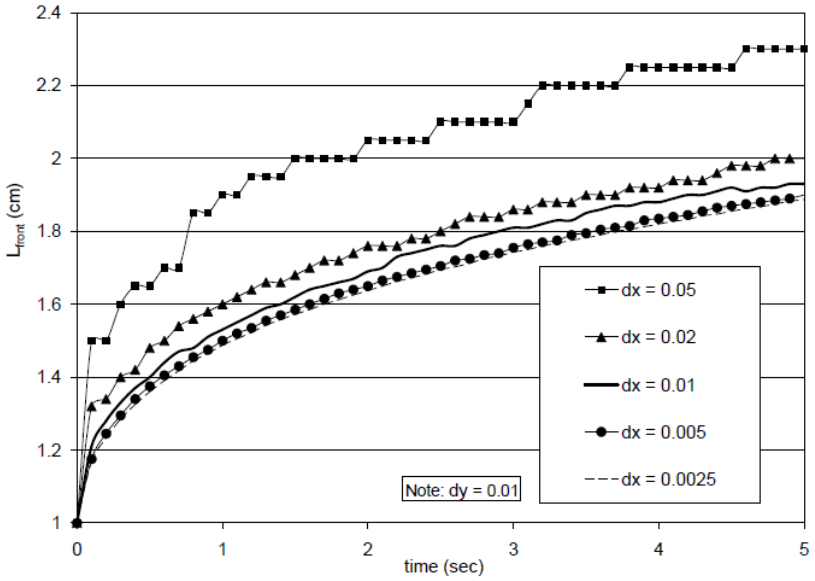

Figure 4.6. Convergence of Axial Spreading (L_{front}) as a function of time, for varying *dx* (*dy* kept constant). This figure shows axial spreading convergence with decreasing mesh size for each time point of the simulation. Input Parameters: ($\alpha = 30°$, $\Delta x = 0.01$, $\Delta y = 0.01$, Δt – adapted, $\mu = 500$ Poise, $\varepsilon_{NEWT} = 10^{-10}$, $\varepsilon_{BiCG} = 10^{-6}$)

Results of the axial convergence study (Figure 4.6) show that as the mesh in the axial direction becomes finer, the solution converges. From this data, I concluded that dx = 0.01 is an operational number because making it even smaller would only add to computation time with very little benefit to the accuracy of the solution.

A similar study confirmed that the solution also converged as dy was decreased (Figure 4.7). From that convergence study I concluded that dy = 0.01 was an operational mesh dimension in the lateral direction because making dy smaller would only improve accuracy to $1/10^{th}$ of a millimeter on average.

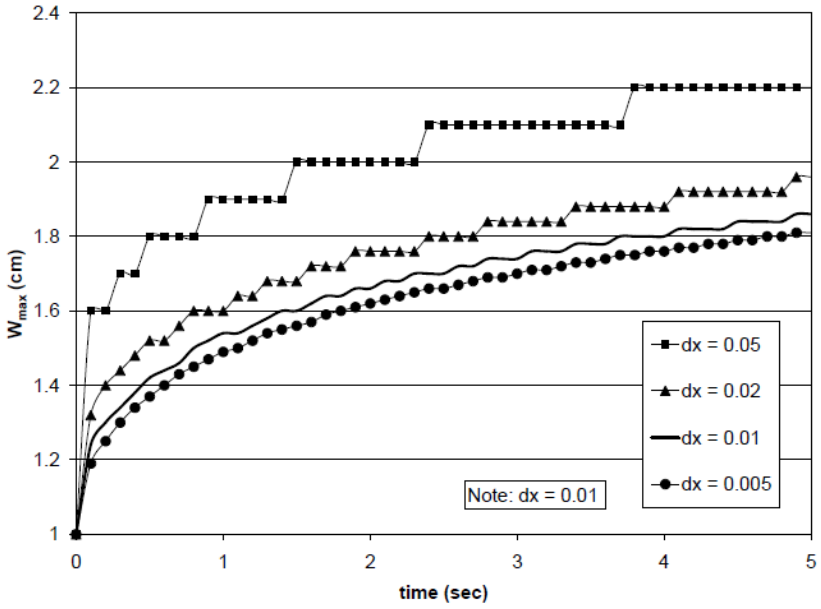

Figure 4.7. Convergence of Lateral Spreading (W) as a function of time, for varying dy (dx kept constant). This figure shows lateral spreading convergence with decreasing mesh size for each time point of the simulation. Numerical solution of lateral spreading converges as dy is made smaller. Input Parameters: (α = 30°, Δx = 0.01, Δy = 0.01, Δt – adapted, μ = 500 Poise, ε_{NEWT} = 10-^{10}, ε_{BiCG} = 10^{-6})

As an interesting note, varying the mesh in a particular direction does not cause the spreading characteristics in the other direction to drastically change.

In a final step to improve the efficiency of the code and determine operational parameters with which I would expect an accurate solution at the lowest computational cost, I conducted several tests to verify that using time adaptation did not impact the accuracy of the spreading characteristics.

During computation, none of the simulations needed to adapt the time step below 10^{-6} sec. To verify that adapting time did not affect the numerical solution, I compared two simulations: (1) one was set to a starting $dt = 10^{-3}$ sec and allowed to adapt time according to $dt = dt \cdot 0.999$ when Newton's method could not converge, and (2) a dt set to a constant $dt = 10^{-6}$ sec without any time adaptation (Newton's method always converged). All other input parameters were identical.

The results of both numerical simulations, with and without time adaptation, were identical for all 5 seconds of simulation. Calculating for $dx = 0.005$ and $dy = 0.01$ seconds of spreading took approximately 64 hours of CPU time without time adaptation, and 7.5 hours with time adaptation. Therefore, using time adaptation improves the efficiency of the code with no loss of accuracy.

Conclusion

Completing the second objective resulted in a 3-D numerical code capable of solving free surface evolution equations for Newtonian, which can also be straightforwardly employed to solve for the spreading of non-Newtonian fluids. Solving the Newtonian evolution equation confirmed that this code converges with refined spatial discretization. In addition, the Newtonian flow results can be used as a validation for simulations with non-Newtonian fluids (see

subsequent chapters). Finally, this code can be updated to account for other driving forces such as surface tension.

The main limitation for this numerical method is efficiency. An upgrade of this code to perform parallel calculations on multiple processors might drastically decrease CPU time.

It should be noted that the implementation of more complex, non-Newtonian, constitutive equations would undoubtedly require more involved spatial discretization, as will be discussed in subsequent chapters. When performing calculations on a single grid point, the current Newtonian model requires the values for 4 surrounding points. As a result, the Jacobian matrix will contain 5 non-zero columns. As will be explained in future chapters, PDE's that govern the height of non-Newtonian fluids will require using more surrounding points.

Unless it is stated otherwise, all of the input parameters used for the Newtonian fluid spreading simulations were implemented into the non-Newtonian models.

Chapter 5 THE POWER-LAW MODEL

Introduction

In an effort to achieve our group's long-term goal of developing a microbicide delivery vehicle with desired spreading characteristics, non-Newtonian viscous forces of any potential vehicle must be accounted for in math modeling. This chapter will address the second overall objective of this project: to develop a numerical model of a non-Newtonian fluid spreading, in 3-dimensions, due to gravity.

Significance and Chapter Goals

Kieweg [3, 4] has developed a 2-D numerical model to simulate free surface, gravity-driven flow of a power-law fluid. When compared with experiments, the 2-D model overestimated flow in the axial direction and was unable to account for coating in the lateral direction.

OBJECTIVE 3: The working objective of this chapter is to develop a 3-D numerical model of a free surface power-law fluid that is spreading under the influence of gravity.

The first hypothesis of this objective is that upgrading the 2-D numerical model, which is currently used to simulate power-law flow, to a 3-D model will result in better agreement with experimentally measured spreading characteristics (from Objective1). The second hypothesis of this objective is that, when comparing with a parabolic initial condition, setting the numerical initial condition with the experimental initial condition will result in better agreement between the numerical and experimental spreading characteristics.

Sub-Objective 3.1: Derive an evolution equation in 3-D using the power-law constitutive equation, and incorporate it into the numerical method developed in Objective 2.

The engineering goals of this sub-objective are to derive an evolution equation with power-law parameters that includes axial and lateral fluxes, and solve it numerically using the method developed in Objective 2 (Chapter 4).

Sub-Objective 3.2: Perform 2-D and 3-D numerical simulation for 2.4%, 2.7% and 3.0% HEC gels using the 3-D power-law code with rheological parameters obtained by fitting to the viscometric data and the experimental initial conditions obtained in Objective 1. For the 2-D numerical simulation, the initial condition will be a cut along the midpoint of the lateral axis of the experimental initial condition.

The hypothesis of this sub-objective is that the 3-D power-law code will match the spreading of the experiment better than the old 2-D power-law code.

Sub-Objective 3.3: Perform numerical simulation for 2.4%, 2.7% and 3.0% HEC gels using the 3-D power-law code with rheological parameters obtained by fitting to the viscometric data using: (1) the experimental initial condition (obtained from Objective 1) and (2) a 4^{th} order approximation of the initial condition that matches the maximum width, length and height of the experimental initial condition.

The hypothesis of this sub-objective is that the code with experimental initial conditions will match the experiment better than an approximate initial condition.

Sub-Objective 3.4: Perform a rigorous power-law parameter study and sensitivity analysis, and document the effect of rheological parameters on axial spreading.

The engineering goal of this sub-objective is to determine how the power-law rheological parameters impact spreading characteristics. I aim to create a framework for optimizing delivery vehicle rheological parameters based on anatomical requirements and functionality.

Thus, the overall engineering goal of this chapter's objective is to develop a 3-D power-law numerical model and use it to test if: (1) 3-D modeling poses a noticeable advantage over 2-D, and (2) incorporating details into the initial conditions improves model agreement with experiment, when compared with an approximate initial condition.

The novel contribution of this work is an original numerical solution of a 3-D power-law evolution equation governing gravity-induced flow. In addition, this work will document the effects 3-D modeling and initial conditions have on the numerical models reliability by drawing direct comparisons between theoretical and experimental spreading characteristics. Finally, I will present a thorough sensitivity analysis of the power-law rheological parameters and their impact on spreading characteristics.

Review of Relevant Literature

For a review of relevant literature discussing power-law rheology and using the power-law constitutive equation in spreading models please refer to the introductions of Chapters 2 and 4, respectively.

Methods

Evolution Equation for a Free Surface Flow of Power-law Fluid

The mathematical model presented in this chapter simulates a gel coating the vaginal epithelium as a finite bolus of a power-law fluid spreading down an incline. The fluid is analyzed using the conservation of linear momentum combined with the power-law fluid constitutive equation.

The primary goal of this model is to develop a differential equation for the evolution of the height of the gel as a function of time and space in the *x* and *y* direction, *h(x,y,t)* to represent the spreading of the finite bolus. The evolution equation will then describe the motion of the gel's free surface, while incorporating gel properties and gravity.

Figure 5.1 shows the coordinate system diagram of our 3-D model analyzing spreading in 3-dimensions (*x*, *y* and *z*). In the remainder of this paper, spreading in the x- direction will be referred to as axial and spreading in the y-direction will be referred to as lateral. In addition, Figure 5.1 defines the relevant nomenclature that will be used to describe spreading characteristics for the remainder of this chapter.

Implementing a similar approach as for the Newtonian model (Chapter 4), I begin by solving the conservation of linear momentum (Eq. (5.1)) where $\tilde{v}$ and $\tilde{g}$ are the velocity and gravity vectors respectively, $\tilde{\tau}$ is the shear stress tensor, *p* is the pressure, and ρ is the density. The analysis presented in this chapter deviates from the Newtonian model after the power-law constitutive equation is introduced, particularly because writing out the tensor invariants results in a function of two tangent vectors.

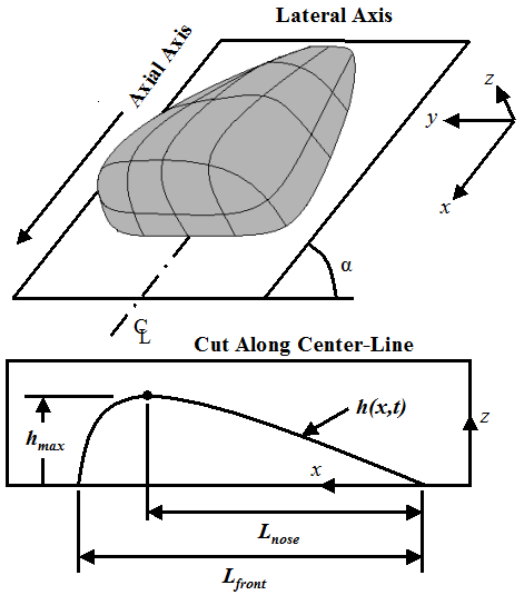

Figure 5.1. Coordinate System (same as Chapter 4) along with defined spreading characteristics considered in this document. Note: *W*, which is not shown here, is the maximum width along the lateral axis.

$$\frac{d\tilde{v}}{dt} + (\tilde{v} \cdot \nabla)\tilde{v} = -\frac{1}{\rho}\nabla p + \frac{1}{\rho}\nabla \cdot \tilde{\tilde{\tau}} + \tilde{g} \qquad (5.1)$$

The velocity vector $\tilde{v}$ is broken down into it cartesian coordinates: *u*, *v*, *w* in the *x*, *y*, *z* directions respectively. The same assumptions are made as in Chapter 4:

1. Thin-film Approximation
2. No slip at the sliding surface
    a. Boundary Condition *1: u (z = 0) = v (z = 0) = 0*
3. The free surface of the gel is exposed to ambient air at pressure p_o.
    a. Boundary Condition 2: at $z = h(x,y,t) \rightarrow \tau_{zx} = \tau_{zy} = 0$
    b. Boundary Condition 3: at $z = h(x,y,t) \rightarrow p = p_o$

Tension at the free surface is neglected under the condition *Bo* >> 1 [55], where *Bo* is the Bond number (measure of body forces to surface tension forces). $Bo = \left(\rho a L^2\right)/\gamma$, where *L* is the

characteristic length, *a* is the acceleration acting on body forces (*g sin* α), and γ is the surface tension. For gravity-induced spreading of HEC gels, the typical Bond number for $\alpha = 10°$ and 90° is 38.3 and 220.5, respectively.

After incorporating the thin-film approximation, and keeping only the relevant stress components, the momentum equation (Eq 5.1) is reduced to three governing equations of motion where α is the angle of the ramp with respect to the horizontal (Figure 5.1).

$$\text{x-direction: } 0 = -\frac{dp}{dx} + \frac{d\tau_{xz}}{dz} + \rho g \sin\alpha \qquad (5.2)$$

$$\text{y-direction: } 0 = -\frac{dp}{dy} + \frac{d\tau_{yz}}{dz} \qquad (5.3)$$

$$\text{z-direction: } 0 = -\frac{dp}{dz} - \rho g \cos\alpha \qquad (5.4)$$

The pressure term is derived using Eq. (5.4) and Boundary Condition 3.b, where p_o is the pressure at the free surface and gets cancelled during integration.

$$p = [\rho g \cos\alpha][h(x,y,t) - z] + p_o \qquad (5.5)$$

A power-law fluid, spreading in 3-D, is mathematically modeled using the constitutive Eq. (5.6), where *m* is the consistency index ($Psec^{n-1}$) and *n* is the level of non-Newtonian behavior (*n* < 1 is shear thinning).

$$\tau_{ij} = m\left|II_{2D}\right|^{\frac{n-1}{2}}\left(2D_{ij}\right) \qquad (5.6)\ [88]$$

In Eq. (5.6), τ_{ij} is a component deviatoric stress tensor, $2\tilde{\tilde{D}} = (\nabla\tilde{v})^T + \nabla\tilde{v}$ is the shear rate tensor and $II_{2D} = (1/2)\left[(tr\,2\tilde{\tilde{D}})^2 - tr(2\tilde{\tilde{D}})^2\right]$ is the second invariant of the shear rate tensor. Utilizing

the second invariant provides the power-law constitutive equation with material indifference (the power-law does not depend on a particular state of reference).

Eq. (5.6) can be broken down into the components remaining in the momentum equations (Eq. (5.2)-(5.3)) after only keeping the shear stress components parallel to the spreading surface: τ_{xz} (Eq. (5.7)) and τ_{yz} (Eq. (5.8)).

$$\tau_{xz} = m\left[\frac{1}{4}\left(\left(\frac{\partial u}{\partial z}\right)^2 + \left(\frac{\partial v}{\partial z}\right)^2\right)\right]^{\frac{n-1}{2}}\left(\frac{\partial u}{\partial z}\right) \tag{5.7}$$

$$\tau_{yz} = m\left[\frac{1}{4}\left(\left(\frac{\partial u}{\partial z}\right)^2 + \left(\frac{\partial v}{\partial z}\right)^2\right)\right]^{\frac{n-1}{2}}\left(\frac{\partial v}{\partial z}\right) \tag{5.8}$$

Rearranging and integrating (with respect to *z*) Eq. (5.2) and (5.3), I derive an expression for τ_{xz} and τ_{yz}, and set them equal to Eq. (5.7) and (6.8).

$$m\left[\frac{1}{4}\left(\left(\frac{\partial u}{\partial z}\right)^2 + \left(\frac{\partial v}{\partial z}\right)^2\right)\right]^{\frac{n-1}{2}}\left(\frac{\partial u}{\partial z}\right) = \rho g\left(\frac{\partial h(x,y,t)}{\partial x}\cos\alpha - \sin\alpha\right)\left(z - h(x,y,t)\right) \tag{5.9}$$

$$m\left[\frac{1}{4}\left(\left(\frac{\partial u}{\partial z}\right)^2 + \left(\frac{\partial v}{\partial z}\right)^2\right)\right]^{\frac{n-1}{2}}\left(\frac{\partial v}{\partial z}\right) = \rho g\left(\frac{\partial h(x,y,t)}{\partial y}\cos\alpha\right)\left(z - h(x,y,t)\right) \tag{5.10}$$

Using the relationship between $\frac{\partial u}{\partial z}$ and $\frac{\partial v}{\partial z}$ shown in Eq. (5.11), along with the no-slip boundary conditions, I solve for the velocity in the axial (Eq. (5.12)) and lateral (Eq. (5.13)) direction.

$$\frac{\left(\frac{\partial h(x,y,t)}{\partial x}\cos\alpha-\sin\alpha\right)\left(z-h(x,y,t)\right)}{\frac{\partial u}{\partial z}}=\frac{\left(\frac{\partial h(x,y,t)}{\partial y}\cos\alpha\right)\left(z-h(x,y,t)\right)}{\frac{\partial v}{\partial z}} \qquad (5.11)$$

Please note from this point on, the variable $h(x,y,t)$ will be expressed as *h*.

$$u=K^{1/n}\left(\frac{n}{n+1}\right)\left(\frac{\partial h}{\partial x}\cos\alpha-\sin\alpha\right)\left[\left(\frac{\partial h}{\partial x}\cos\alpha-\sin\alpha\right)^2+\left(\frac{\partial h}{\partial y}\cos\alpha\right)^2\right]^{\frac{1-n}{2n}}\left[(z-h)^{\frac{1}{n}+1}-h^{\frac{1}{n}+1}\right] \qquad (5.12)$$

$$v=K^{1/n}\left(\frac{n}{n+1}\right)\left(\frac{\partial h}{\partial y}\cos\alpha\right)\left[\left(\frac{\partial h}{\partial x}\cos\alpha-\sin\alpha\right)^2+\left(\frac{\partial h}{\partial y}\cos\alpha\right)^2\right]^{\frac{1-n}{2n}}\left[(z-h)^{\frac{1}{n}+1}-h^{\frac{1}{n}+1}\right] \qquad (5.13)$$

Eq. (5.12) and (5.13) are explicit expressions for velocity in the axial and lateral directions, respectively, where $K=\frac{\rho g}{m}$.

The flow rate per unit width, in the axial (Eq. (5.15)) and lateral (Eq. (5.16)) direction, is then found by inserting the velocity expressions into Eq. (5.14).

$$q_x=\int_0^{h(x.y.t)}u(x,y,t)\,dz \qquad\qquad q_y=\int_0^{h(x.y.t)}v(x,y,t)\,dz \qquad (5.14)$$

Using the flow rates in the axial (Eq. (5.15)) and lateral (Eq. (5.16)) directions, substituted into the conservation of mass (Eq. (5.17)), I arrive at the non-linear partial differential equation that governs the surface evolution.

$$q_x=-K^{1/n}\left(\frac{n}{1+2n}\right)\left(\frac{\partial h}{\partial x}\cos\alpha-\sin\alpha\right)\left[\left(\frac{\partial h}{\partial x}\cos\alpha-\sin\alpha\right)^2+\left(\frac{\partial h}{\partial y}\cos\alpha\right)^2\right]^{\frac{1-n}{2n}}h^{\frac{1}{n}+2} \qquad (5.15)$$

$$q_y = -K^{1/n}\left(\frac{n}{1+2n}\right)\left(\frac{\partial h}{\partial y}\cos\alpha\right)\left[\left(\frac{\partial h}{\partial x}\cos\alpha - \sin\alpha\right)^2 + \left(\frac{\partial h}{\partial y}\cos\alpha\right)^2\right]^{\frac{1-n}{2n}} h^{\frac{1}{n}+2} \tag{5.16}$$

$$\frac{dh(x,y,t)}{dt} + \frac{dq_x}{dx} + \frac{dq_y}{dy} = 0 \tag{5.17}$$

Eq. (5.15) and (5.16) are rearranged and simplified to make them more suitable for numerical discretization, where $\Lambda = \left(\frac{n}{1+2n}\right)\left(\frac{\rho g \cos\alpha}{m}\right)^{1/n}$.

$$q_x = \Lambda\left(\tan\alpha - \frac{\partial h}{\partial x}\right)\left[\left(\frac{\partial h}{\partial x} - \tan\alpha\right)^2 + \left(\frac{\partial h}{\partial y}\right)^2\right]^{\frac{1-n}{2n}} h^{\frac{1}{n}+2} \tag{5.18}$$

$$q_y = -\Lambda\left(\frac{\partial h}{\partial y}\right)\left[\left(\frac{\partial h}{\partial x} - \tan\alpha\right)^2 + \left(\frac{\partial h}{\partial y}\right)^2\right]^{\frac{1-n}{2n}} h^{\frac{1}{n}+2} \tag{5.19}$$

By setting the shear-thinning index, *n*, to 1, and neglecting all terms relating to the lateral direction, and comparing it with its Newtonian counterpart found by Huppert [55], Eq. (5.17) is validated. Under the Newtonian approximation (n = 1), the flux terms (Eq. (5.18) and (5.19)) reduce to the flux terms found for the Newtonian model ((Eq. (4.11) and (4.12)) in Chapter 4. If the surface is flat and lateral spreading is neglected, Eq. (5.17) matches equations of the same form as in Gorodtsov [[89], eqn 5] and Gratton *et al.* [74], as mentioned by Betulu and Fontelos [90].

Numerical solution of the evolution equation

In order to properly optimize a potential delivery vehicle, it is important to be able to perform a detailed sensitivity analysis of the spreading characteristics as a function of rheological parameters, inclination angle and time. Analytically solving Eq. (5.17) provides limited

information about the spreading at either a horizontal or vertical extreme. A numerical solution allows us to obtain the entire free surface profile as a function of space, time, inclination angle and rheological parameters. In addition, a working numerical model yields itself to be updated to account for other external forces (e.g. squeezing, shear, surface tension) and constitutive equations.

As was done for the Newtonian numerical model in Chapter 4, the spreading domain is divided into a finite number of grid points. The evolution equation (Eq. (5.17)) was discretized using the central difference approximation (Eq. (5.20)).

$$\frac{dh(x,y,t)}{dt} + \Lambda\left(\frac{q_{(x)k+m/2} - q_{(x)k-m/2}}{\Delta x} + \frac{q_{(y)k+1/2} - q_{(y)k-1/2}}{\Delta y}\right) = 0 \tag{5.20}$$

The fluxes were discretized using central differences (Eq. (5.21)-(5.24)), centered about the node interfaces.

$$q_{(x)k+M/2} = \left(\tan\alpha - \frac{h_{k+M} - h_k}{\Delta x}\right)\left[\left(\frac{h_{k+M} - h_k}{\Delta x} - \tan\alpha\right)^2 + \left(\frac{\partial h}{\partial y}\right)^2\right]^{\frac{1-n}{2n}}\left(\frac{1}{2}h_k^{\frac{1}{n}+2} + \frac{1}{2}h_{k+M}^{\frac{1}{n}+2}\right) \tag{5.21}$$

$$q_{(x)k-M/2} = \left(\tan\alpha - \frac{h_k - h_{k-M}}{\Delta x}\right)\left[\left(\frac{h_k - h_{k-M}}{\Delta x} - \tan\alpha\right)^2 + \left(\frac{\partial h}{\partial y}\right)^2\right]^{\frac{1-n}{2n}}\left(\frac{1}{2}h_k^{\frac{1}{n}+2} + \frac{1}{2}h_{k-M}^{\frac{1}{n}+2}\right) \tag{5.22}$$

$$q_{(y)k+1/2} = -\left(\frac{h_{k+1} - h_k}{\Delta y}\right)\left[\left(\frac{\partial h}{\partial x} - \tan\alpha\right)^2 + \left(\frac{h_{k+1} - h_k}{\Delta y}\right)^2\right]^{\frac{1-n}{2n}}\left(\frac{1}{2}h_k^{\frac{1}{n}+2} + \frac{1}{2}h_{k+1}^{\frac{1}{n}+2}\right) \tag{5.23}$$

$$q_{(y)k-1/2} = -\left(\frac{h_k - h_{k-1}}{\Delta y}\right)\left[\left(\frac{\partial h}{\partial x} - \tan\alpha\right)^2 + \left(\frac{h_k - h_{k-1}}{\Delta y}\right)^2\right]^{\frac{1-n}{2n}}\left(\frac{1}{2}h_k^{\frac{1}{n}+2} + \frac{1}{2}h_{k-1}^{\frac{1}{n}+2}\right) \tag{5.24}$$

The discretized flux terms in Eq. (5.21)-(5.24) simplify down the discretized flux terms of Newtonian model (Eq. (4.16)-(4.19)) when setting $n = 1$ and after incorporating them into Eq. (5.20).

Due to the fact that there will be no flux across the domain boundaries, the total volume of the fluid should stay constant throughout the simulation (Eq. (5.25)).

$$\frac{\partial V}{\partial t} = \frac{\partial}{\partial t}\iint_{\Omega} h(x,y,t)\,dx\,dy = 0 \tag{5.25}$$

The flux terms must be discretized in such a way that the conservation of mass is satisfied. Any slight deviation from the initial fluid volume should only be a result of the truncation error and not a violation of mass conservation.

The flux in the axial direction contains a $\partial h/\partial y$ term and the flux in the lateral direction contains a $\partial h/\partial y$ term (referred to in this document as Perpendicular Derivatives). Therefore, in order to properly discretize these terms, the sum of each discretization over the entire domain must be equal to zero (Eq. (5.26) and (5.27)).

$$\Lambda\frac{\Delta t}{\Delta x}\sum_{k=0}^{TOT}\left(q_{(x)_{k+M/2}} - q_{(x)_{k-M/2}}\right) = 0 \tag{5.26}$$

$$\Lambda\frac{\Delta t}{\Delta y}\sum_{k=0}^{TOT}\left(q_{(x)_{k+1/2}} - q_{(x)_{k-1/2}}\right) = 0 \tag{5.27}$$

To satisfy Eq. (5.26) and (5.27), if one considers a random point, *z*, the following condition, for the flux in the axial direction, must be true to satisfy the conservation of mass:

$$q_{(x)_{k+M/2}}\Big|_{k=z} - q_{(x)_{k-M/2}}\Big|_{k=z+M} = 0 \tag{5.28}$$

This results in a technique for discretizing the ∂h/∂y term in the axial flux equation and the ∂h/∂x term in the lateral flux equation.

In: $$q_{x_{K+M/2}} \rightarrow \frac{\partial h}{\partial y} \cong \frac{h_{K+M+1} - h_{K+M-1}}{2\Delta y} \tag{5.29}$$

In: $$q_{x_{K-M/2}} \rightarrow \frac{\partial h}{\partial y} \cong \frac{h_{K+1} - h_{K-1}}{2\Delta y} \tag{5.30}$$

In: $$q_{x_{K+1/2}} \rightarrow \frac{\partial h}{\partial x} \cong \frac{h_{K+M+1} - h_{K-M+1}}{2\Delta x} \tag{5.31}$$

In: $$q_{x_{K+1/2}} \rightarrow \frac{\partial h}{\partial x} \cong \frac{h_{K+M} - h_{K-M}}{2\Delta x} \tag{5.32}$$

As a result of the more complex spatial discretization, the calculation of each point will now require more surrounding points (Figure 5.2). The subscript for each grid point can be matched to its physical location in Figure 5.2.

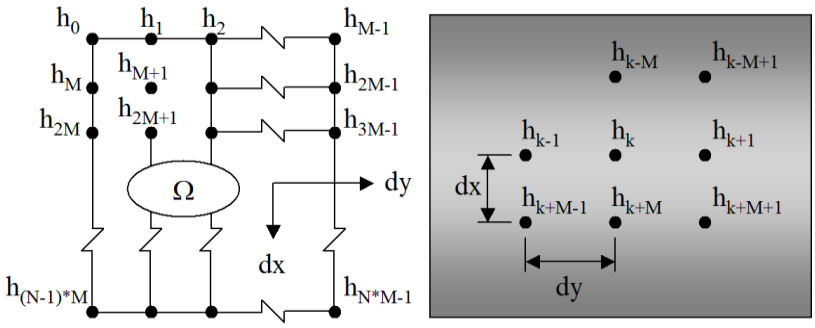

Figure 5.2. **Left:** Domain for the numerical method discretized into N×M points. **Right:** Points used in discretized Eq. (5.20) about a specific point, *k*.

Applying Eq. (5.20) to the domain will result in *TOT* non-linear equations with *TOT* unknowns (Eq. (5.33)), where the superscript *n* represents the time step and the subscript k is the point in space. Each discretized point is now a function on 9 unknowns as opposed to the 5 unknowns encountered in the Newtonian model.

$$F_k(h_k^{n+1}, h_{k+1+M}^{n+1}, h_{k+1-M}^{n+1}, h_{k+1}^{n+1}, h_{k-1}^{n+1}, h_{k+M}^{n+1}, h_{k-M}^{n+1}, h_{k-M+1}^{n+1}) = 0 \text{ for } (0 \le k \le TOT\text{-}1) \tag{5.33}$$

As with the Newtonian numerical code, the system of non-linear equations was solved using Newton's method. The first norm of the height change, resulting from each Newton's iteration,

was used as the check for Newton's method convergence. Once the first norm of the height change falls below 10^{-9}, Newton's method iteration is terminated and a solution for the new time step is accepted.

The Preconditioned BiConjugate Gradient (P-BiCG) method, used to solve the linear system encountered in each iteration of Newton's method, was set to iterate until the second norm of the residuals converges below 10^{-6}. Including more points in the calculation will result in more non-zero elements in the Jacobian matrix. For this specific case, there will now be a total of 9 non-zero elements, as opposed to the 5 for the Newtonian simulation. The P-BiCG linear system solver was modified to accommodate these elements in the sparse matrix. In the event that one might want to include surface tension into the evolution equation, the Jacobian matrix would grow to 12 non-zero elements and a further update would be required to the linear system solver.

Mesh convergence study

A mesh convergence study, identical to the one described in Chapter 4, was completed for the power-law numerical code.

In order to determine if the shear-thinning parameter had an influence on numerical convergence, a convergence study was conducted with all the parameters identical to the Newtonian code study (Chapter 4), but with the shear-thinning parameter, *n*, set to 0.5.

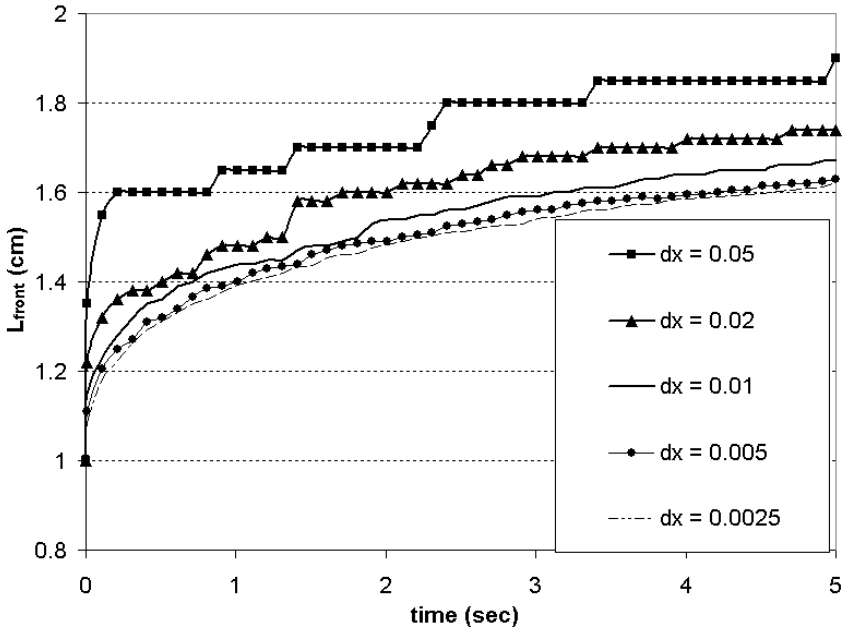

Figure 5.3. Convergence of Axial Spreading (L_{front}) as a function of time, for varying *dx* (*dy* kept constant). This figure shows axial spreading convergence with decreasing mesh size for each time point of the simulation. Input Parameters: ($\alpha = 30°$, dy = 0.01, Δt – adapted, $m = 707.11\ Ps^{n-1}$, $n = 0.5$ $\varepsilon_{NEWT} = 10^{-9}$, $\varepsilon_{BiCG} = 10^{-6}$)

As was evident in the Newtonian convergence study, the power-law numerical code is also showing numerical order. The solution of axial spreading seems to converge to a specific solution, as the mesh in the axial direction is made finer. For the remainder of this chapter I performed all simulations using *dx = dy = 0.01*, which found results with acceptable accuracy (within 1*mm* of finer mesh sizes), without a great sacrifice to computational performance. The Newtonian code showed that convergence in the lateral direction is similar to the axial direction. I assumed that because the power-law code showed clear convergence in the axial direction, almost identical to the Newtonian code, it would show the same convergence in the lateral direction.

Validating the numerical solution

The two techniques I chose for validating the power-law code were: (1) to compare it with the Newtonian code and (2) to compare the spreading profile to an analytical solution that satisfies the evolution equation (Eq. (5.17)).

Technique 1 - Compare with numerical solution of Newtonian code

In the same manner as validating the evolution equation, the numerical solution was validated by comparing it to the Newtonian code, with $n = 1$ and $m = \mu$. The spreading results of power-law code and Newtonian code were in complete agreement.

Technique 2 - Compare with similarity solution

Assuming mostly convective flow, $\tan\alpha >> (\partial h/\partial x)$, as occurs at steep inclinations, the evolution equation is simplified to neglect any diffusive components, including the diffusive flux in the lateral direction. Eq. (5.34) is the convective component of the power-law evolution equation (Eq. (5.17)).

$$\frac{\partial h}{\partial t} + \left(\frac{\rho g \sin\alpha}{m}\right)^{1/n} \left(h^{1/n+1}\right) \frac{\partial h}{\partial x} = 0 \tag{5.34}$$

Recognizing that Eq. (5.34) takes the form of a non-linear advection equation and its commonalities with the material derivative of *h*, the solution to the convective component of Eq. (5.34) is found by solving for *h*, which is constant along the characteristics of the form:

$$\frac{\partial x}{\partial t} = \left(\frac{\rho g \sin(\alpha)}{m}\right)^{1/n} h^{1/n+1} \tag{5.35}$$

The method of characteristics (as outlined by Huppert for a Newtonian fluid [55]) and consideration of times far beyond the initial condition, $t \to \infty$, provides the height profile of the free surface.

$$h(x,t) = \left(\frac{m}{\rho g \sin(\alpha)} \right)^{\frac{1}{1+n}} \left(\frac{x}{t} \right)^{\frac{n}{1+n}} \tag{5.36}$$

This similarity solution satisfies the convective component of the evolution (Eq. (5.34)). Considering a Newtonian fluid, Eq. (5.36) reduces to Huppert's similarity solution [55]. Perazzo and Gratton [74] found a similar expression for the similarity solution, which also satisfies the evolution equation, but with an extra term that is a function of the shear-thinning index. This dissimilarity appears because, I believe, Gratton's *et al.* constitutive equation has a mistake, which is carried as a constant through the entire derivation and ultimately ends up in the solution. Even with the extra term, the evolution equation is satisfied because the terms cancel.

The free surface of the 3-D numerical model was compared with the free surface of the 2-D similarity solution at 90 *sec* of spreading. Qualitative assessment of Figure 5.4 confirms that the numerical and analytical solutions are in complete agreement. The numerical solution shown in Figure 5.4 is a cross-section of the free surface that was cut along the midpoint of the lateral plane.

The slight discrepancy between the numerical and the analytical solutions of the free surface at the leading edge is likely the result of the diffusive component, which seems to have an added effect on the 3-D numerical model by diffusing a slight current in the lateral direction, resulting in slower propagation of the wave front in the axial direction (Figure 5.4).

An investigation of the 2-D numerical model (not shown) confirmed that the numerical solution is indeed invariant of the initial condition. The size of the initial condition does not change the gradient of the free surface, but rather the axial location of L_{nose}. In fact, the location of L_{nose}, which is almost L_{front} for very steep slopes, appears to be directly affected by the initial area under the free surface, A.

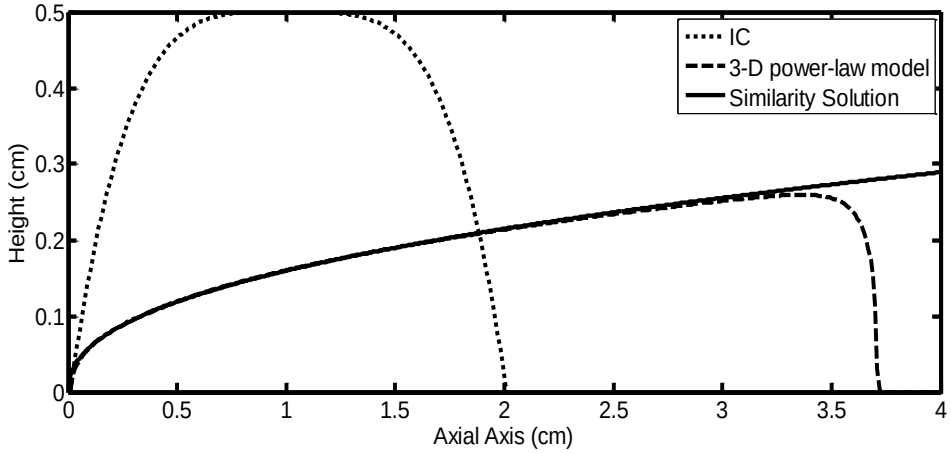

Figure 5.4. Comparison of height profile, at 90 *sec* of spreading, obtained from the 3-D numerical model and the similarity solution. There is good agreement between the numerical and similarity solution, validating the numerical method. Input parameters for both solutions: α = *60°, m = 1000 Ps*$^{n-1}$, *n = 0.75*. Note: The profile of the 3-D numerical model is cut at the centerline along the lateral axis.

One does not need to know the exact shape of the initial condition, but can find an expression for the axial location of the wave crest as a function of time by recognizing two key points: (1) The initial area of the spreading bolus, $A = \int h\,(x,t)\,dx$, will remain constant as the bolus spreads (Eq. (5.37)), and (2) for a very steep slope the nose can be approximated at the same location as the front [55].

$$L_{nose} \approx L_{front}(t >> 0) = \left[A \cdot \left(\frac{2n+1}{n+1} \right) \right]^{\frac{n+1}{2n+1}} \left[\frac{\rho\, g\, \sin(\alpha)}{m} \right]^{\frac{1}{2n+1}} t^{\frac{n}{2n+1}} \qquad (5.37)$$

Results

Each numerical simulation was carried out on the ITTC computing cluster at the University of Kansas. For 90 *sec* of spreading, the 3-D simulations took approximately 120 hours, while most 2-D simulations required less than 24 hours of computation.

The topography of the height evolution of spreading power-law simulations is similar to the results of the Newtonian numerical model, presented in Chapter 4. Nevertheless, incorporating non-Newtonian shear-thinning effects caused noticeable changes to spreading characteristics.

2-D and 3-D Numerical Models Compared with Experiment

As explained in Chapter 3, I conducted a total of 9 spreading experiments on HEC gels, with 2.4%, 2.7% and 3.0% HEC tested in triplicate (each concentration of HEC consisted of 3 runs: R1-R3). Each numerical simulation corresponds to a specific experiment by incorporating the surface topography of that experiment's initial condition. Therefore, a total of 9 numerical simulations were conducted using the 2-D and 3-D numerical code. Each simulation used the experiment's initial condition obtained in Chapter 3 and input rheological properties for the respective HEC concentration. The 2-D code used the profile of the free surface as sliced along the axial axis at the lateral midpoint of the experimental domain.

As expected, gels with higher concentrations of HEC did not propagate as far in either the axial or lateral direction, when compared to gels with lower concentrations. In addition, experiments showed that the moving front at the leading edge decelerated in the axial direction as the free surface became smoother (less steep slopes), regardless of HEC concentration.

Figure 5.5 presents sample spreading profiles of the experiment alongside the numerical model for a 2.4% HEC gel. Both the experimental data and the 3-D numerical model demonstrate that the gels, regardless of HEC concentration, do not accelerate in the axial direction – as one might suspect given that gravity is the primary driving force. In fact, judging by the velocity profiles of the leading edge (Figure 5.5), the gel will eventually stop spreading as the curvature of the free surface decreases.

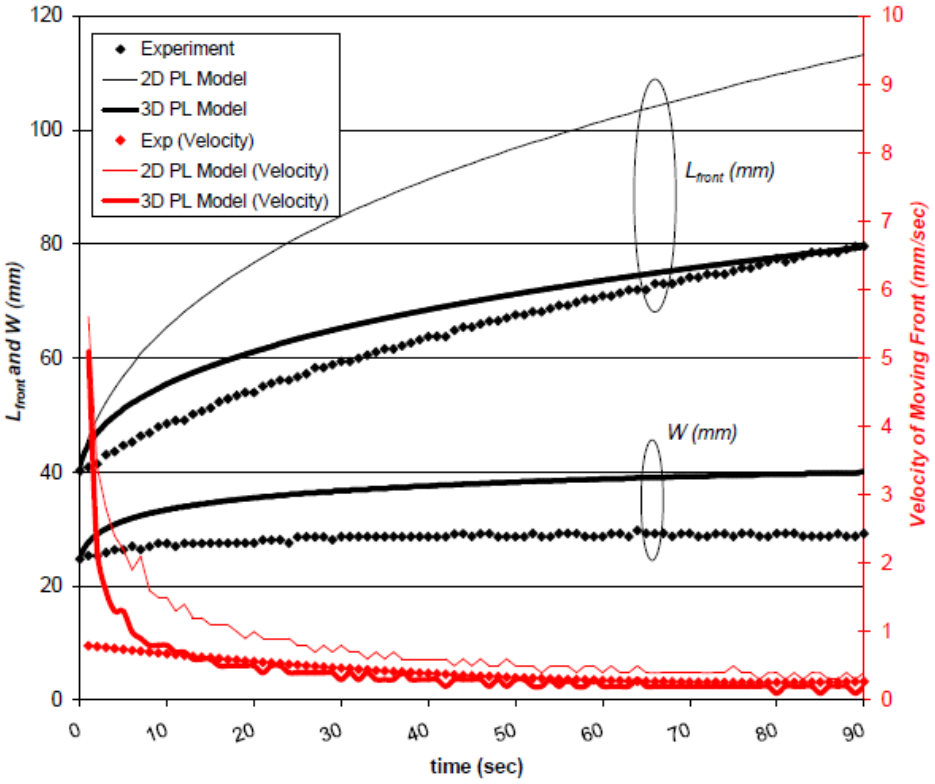

Figure 5.5. Sample spreading characteristics (black) and the axial velocity of the moving front (red) for a sample 2.4% HEC R1 with experimental IC. **Black (Left axis):** Axial (L_{front}) and lateral (W) spreading as a function of time for 2-D and 3-D models, and experiment. **Red (Right axis):** Velocity of the moving front as a function of time for 2-D and 3-D models, and experiment. This figure shows that both the 2-D and 3-D numerical models overestimate axial spreading when compared with experiment, but the 3-D model is a considerable improvement over the 2-D model.

It is clearly evident that accounting for lateral spreading has an effect on spreading in the axial direction, and drastically improves agreement between the numerical model and

experiment. Lateral spreading is only due to slumping, since the spreading surface is not directed downhill along the lateral direction. Because the experimental data shows that most lateral slumping plateaus at approximately 30 seconds, we conclude that a balance must be reached between the gels internal (e.g. viscous and surface tension) and external driving factors (e.g gravity). This is not happening in the numerical models, which might indicate that there is an internal force (e.g. surface tension) that any future simulation might need to take into account.

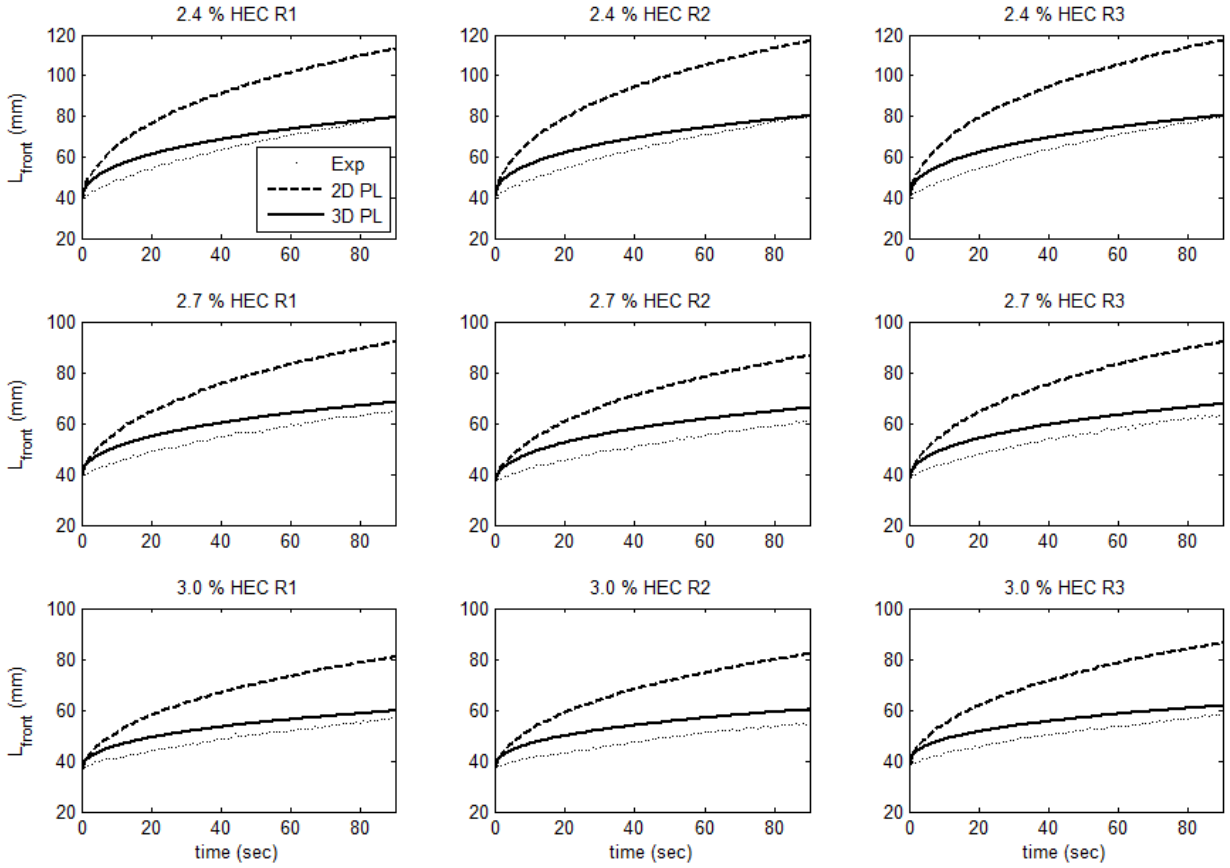

Figure 5.6. Comparison of axial spreading (L_{front}) of 9 experimental runs (3 runs of 2.4%, 2.7%, and 3.0% HEC concentration), and 9 numerical simulations that used the corresponding experimental initial condition obtained in Chapter 3. The 3-D power-law model shows considerable improvement over the 2-D power-law model, when comparing with experiment. Experiment (dot), 3-D Numerical Model (solid), 2-D Numerical Model (dashed).

The speeds of the leading edge seem to disagree at the beginning of the experiment, but all reach a plateau of similar values for later times. The experiment reaches what seems to be a constant axial velocity at approximately 70 seconds, which is a similar observation for both the 2-D and 3-D numerical models. Nevertheless, the 3-D numerical model approaches the experiment much sooner, and seems to plateau at a constant velocity that is closer to the experiment than the 2-D numerical model.

In Figure 5.6, the conclusions reached for a single run of 2.4% HEC are consistent with the other HEC concentrations and experimental runs. Each numerical simulation was carried out using the experimental initial condition obtained in Chapter 3.

In all cases, axial spreading of the 2-D numerical model overestimates the experiment. There is substantial agreement between the experiment and 3-D numerical model to say that it is capable of predicting the experiment within 1cm. These results satisfy the hypothesis that accounting for lateral spreading would noticeably improve the numerical model's agreement with experiment.

Comparing the different initial condition approximations in numerical simulations

A study was conducted to determine the importance of the initial condition used in the 3-D numerical simulation. For each of the 9 experimental runs, I computed a numerical simulation that used: (1) the initial condition obtained by using the surface topography image acquisition algorithm described in Chapter 3 (referred to in this document as: 'Real IC,' and used for all previous results), and (2) an approximation of the initial condition described in Eq. (5.38), where the coefficients a, b and h_{max} are chosen for the profile to match the experiment in maximum length, width and height within 1mm of the measured values.

$$h(x,y) = -\left(\frac{x}{a}\right)^4 - \left(\frac{y}{b}\right)^4 + h_{\max} \tag{5.38}$$

As a result, the benefits of using a more accurate initial condition were inconclusive, when comparing the spreading profiles with experiment. In fact, some cases showed that using an approximate initial condition was computationally more efficient without a noticeable change to spreading characteristics. The results from this work are not shown in this dissertation because the spreading curves comparing the two initial condition approximations are practically indistinguishable.

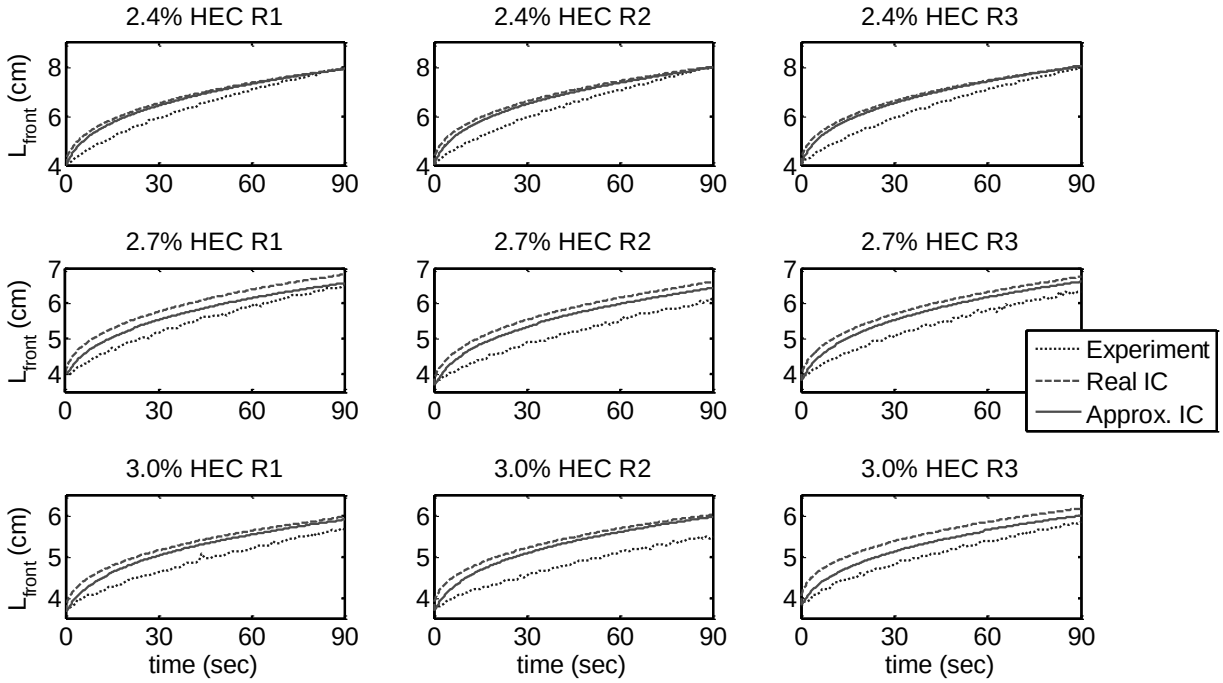

Figure 5.7. Axial spreading (L_{front}) of 3-D power-law simulations compared with 9 experimental runs. First row shows 3 runs of 2.4%HEC gels, and the second and third row show 2.7% HEC and 3.0% HEC, respectively (vertical-axis scales of each row are different). From these plots, it appears as if the experimental IC slightly improves agreement with experiment, but Figure 5.9 will show that this is misleading.

Figure 5.7 shows axial spreading characteristics of the power-law computational model, using real and approximate initial conditions, compared with experiment. Ostensibly, it appears that using an approximate initial condition actually slightly improves agreement between model and experiment. In each of the 9 comparisons, the power-law model overestimates the experiment at the initial phases of spreading and using an approximate initial condition seems to decrease this affect. Figure 5.8 shows that for a 2.7% HEC gel, the approximate initial condition does not spread as far in the initial stages of spreading because it takes approximately 0.5 seconds for the center of mass to move closer to the leading edge and advance the contact line.

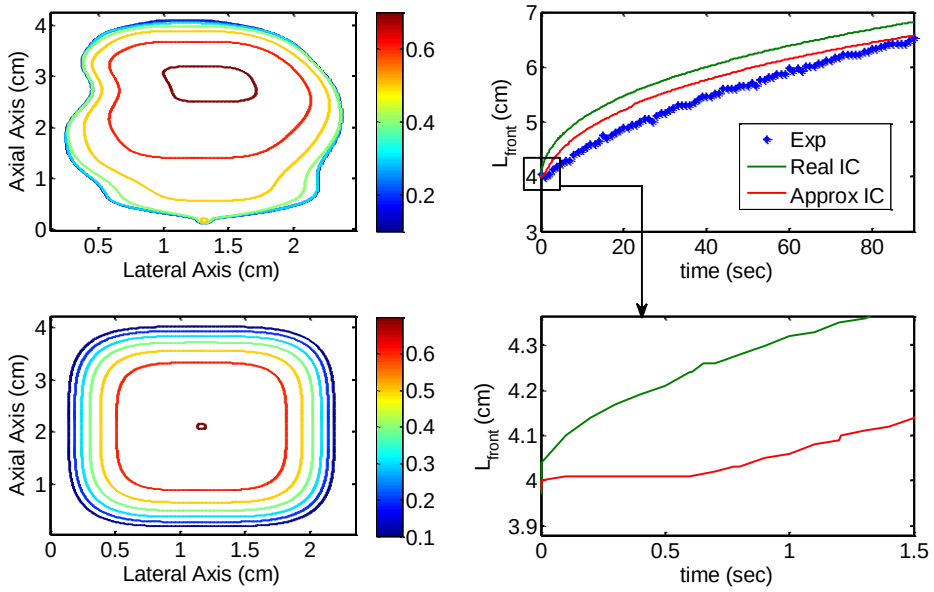

Figure 5.8. An example of 3-D power-law model spreading using two different initial conditions and compared with experiment, for a 2.7% HEC gel. **Top Left:** Surface topography of Real IC, obtained using method outlined in Chapter 3. **Bottom Left:** Surface topography of approximate IC, obtained using Eq. (5.38) with bulk geometry dimensions of Real IC. **Top Right:** Axial spreading (L_{front}) vs. time for computations using Real and Approximate Initial Conditions, compared with experiment (same as Figure 5.8 – 2.7% HEC R1). **Bottom Right:** Axial spreading vs. time for computations using Approximate and Real Initial Conditions at early stage of spreading. This figure shows that the improved agreement between Approximate IC and experiment seen in Figure 5.8 is misleading, and is a result of the "waiting time solution" [52].

This phenomenon is known as the waiting time solution [52] and it can be thought of as an additional variable of error influencing the computational model. The slight improvement of the

approximate initial condition over the real initial condition is purely coincidental because the power-law model tends to slightly overestimate axial spreading, while the "waiting time solution" phenomenon, seen when using an approximate initial condition, caused a slight delay.

Parameter and Sensitivity Analysis

All sensitivity analyses were conducted for a simulation set to spreading on a 30° incline for 90 seconds. Eq. (5.38) was used to construct the initial condition, with $W_{max} \times L_{max} \times h_{max}$ were set to: 2cm × 2cm × 0.5cm.

A non-dimensional parameter analysis has been completed for the 2-D numerical model [3]. Because the spreading profiles between the 2-D and 3-D numerical models were so dissimilar, I present a separate 3-D numerical analysis to determine the effect of power-law parameters and gravity on spreading range in a given time and inclination, and spreading rate, which was not included in the original 2-D analysis. In addition, I will present a novel "percent" sensitivity analysis to determine how fractional changes to the power-law parameters impact spreading. *I hope for this analysis to be used as a preliminary step for optimizing potential delivery vehicles, based on desired clinical performance and external driving factors such as inclination angle.*

In this document I will consider the shear-thinning and consistency index ranges most applicable to microbicides. For that reason I will discuss a fluid with pseudoplastic behavior, with a consistency index within the range of 200 to 600 P s^{n-1}. Figure 5.9 shows final axial spreading lengths of a 90 second simulation at different values of *n* and *m*, for a total of 9 data points. Overlaying dashed lines computed at slightly different values of *n* show increases to axial spreading as a result of marginal (10% increase) changes to the power-law parameters can be

approximated by the general curve, but as I will show later in this chapter, these changes are more complicated than they may appear.

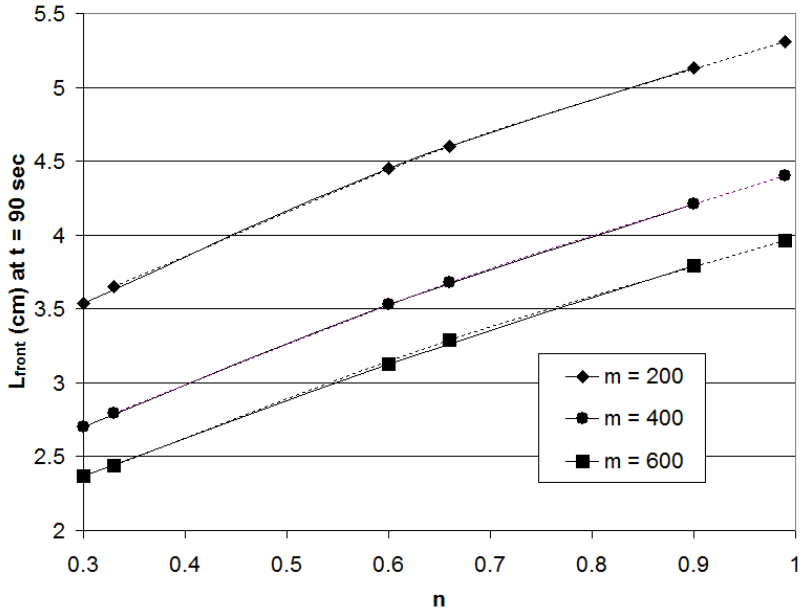

Figure 5.9. Axial spreading length (L_{front}) after 90 sec of spreading, for different values of n and m. The solid lines indicate the original parameter study presented in Figure 5.11, while the dashed lines represent an identical parameter study after increasing the values of n by 10%. This figure shows that the trends can be used to roughly predict axial spreading after slight changes to the power-law parameters. Note: $m \equiv$ consistency index [=] Ps^{n-1}; $n \equiv$ shear-thinning index.

The contour plots for the power-law parameter analysis show the final position of the moving front, L_{front}, after 90 sec of spreading, which is the same data as is shown by the solid lines of Figure 5.9. Axial spreading values were recorded for n = 0.3, 0.6, and 0.9; and m = 200, 400, and 600, and a MATLAB interpolation algorithm is used to reconstruct the contour plots. Figure 5.10 shows that fluid with smaller values of m and smaller shear-thinning effects (i.e. larger n) will spread further in the axial direction, at a given inclination angle.

The angle of each contour line can be reasoned to represent the relationship between the two parameters: n and m. A vertical contour would translate to mean that axial spreading is independent of the consistency index. A horizontal contour would indicate that axial spreading is

independent of the shear-thinning index. A contour slanted at a 45 degree angle represents that both parameters hold approximately equal weight within their own range.

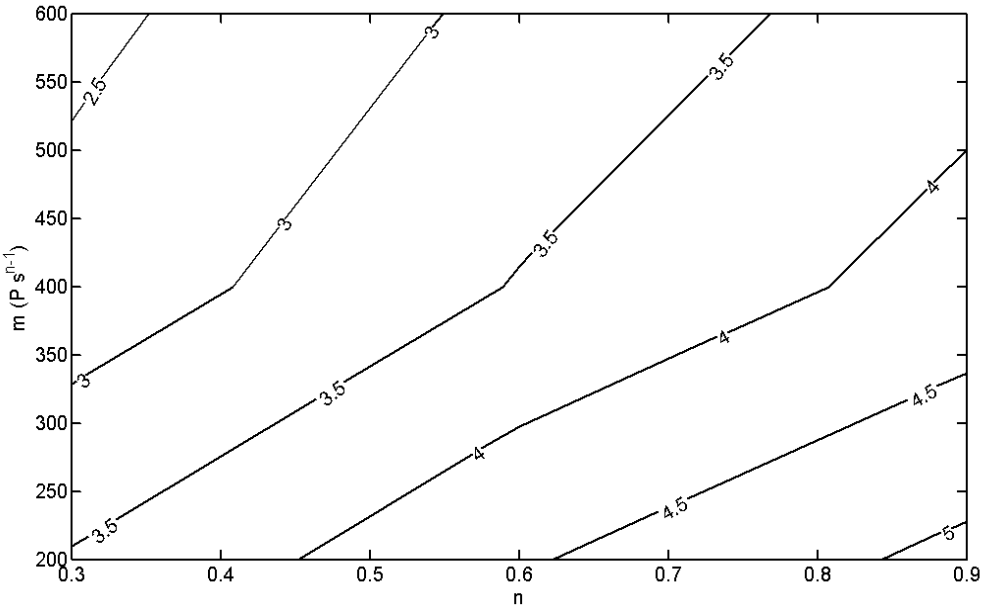

Figure 5.10. Contour lines of axial spreading (L_{front} [=] cm) as a function of power-law rheological parameters. Created using 9 numerical simulations and interpolated using a MATLAB algorithm. This figure shows that within the ranges of *m* and *n* considered, both parameters have near equal impact on axial spreading. Also, maximum spreading in the axial direction occurs at higher values of *n* (near Newtonian) and lower values of *m.* Note: $m \equiv$ consistency index [=] Ps^{n-1}; $n \equiv$ shear-thinning index.

Influence of Gravity to Viscous Force Ratio on Axial Spreading

In an effort to analyze the dependence of multiple variables on axial and lateral spreading, Eq. (5.17) was non-dimensionalized according to the transformations in Eq. (5.40)-(5.43) to arrive at the non-dimensional PDE (Eq. (5.44)).

$$\hat{h} = h / H \tag{5.40}$$

$$\hat{x} = x / H \tag{5.41}$$

$$\hat{y} = y / H \tag{5.42}$$

$$\hat{t} = \frac{t}{\left(\frac{m}{\rho g H \sin\alpha}\right)^{1/n}} \tag{5.43}$$

$$\frac{\partial \hat{h}}{\partial \hat{t}} + \tan^{-1}\alpha\left\{\frac{\partial}{\partial \hat{x}}\left[\left(\tan\alpha - \frac{\partial \hat{h}}{\partial \hat{x}}\right)\left[\left(\frac{\partial \hat{h}}{\partial \hat{x}} - \tan\alpha\right)^2 + \left(\frac{\partial \hat{h}}{\partial \hat{y}}\right)^2\right]^{\frac{1-n}{2n}} \hat{h}^{\frac{1}{n}+2}\right]\right.$$
$$\left. + \frac{\partial}{\partial \hat{y}}\left[\left(\frac{\partial \hat{h}}{\partial \hat{x}}\right)\left[\left(\frac{\partial \hat{h}}{\partial \hat{x}} - \tan\alpha\right)^2 + \left(\frac{\partial \hat{h}}{\partial \hat{y}}\right)^2\right]^{\frac{1-n}{2n}} \hat{h}^{\frac{1}{n}+2}\right]\right\} = 0 \tag{5.44}$$

For the 2-D numerical model, preliminary parameter analysis showed that no noticeable axial spreading would occur until after the gravity forces begin to dominate over viscous forces (not shown in this dissertation). We do not see this constraint for the 3-D numerical model. In fact, we see that the 3-D numerical model starts to show signs of spreading earlier, but will spread less at later times. The early onset of spreading is most likely due to the fact that both fluxes have a convective and diffusive component.

Figure 5.11 shows the relationship between axial spreading and the ratio of gravity to viscous forces. The curves for the lateral component of spreading appear to have the same trends as the axial curves and are not shown in Figure 5.11. In the beginning stages of each of these simulations, Figure 5.11 shows a plateau resulting from the fact that gravity forces must take a moment to overcome the viscous forces, and sufficient mass must accumulate at the leading edge ($\partial h/\partial x$ at the leading edge must be sufficiently high) for the contact-line to propagate.

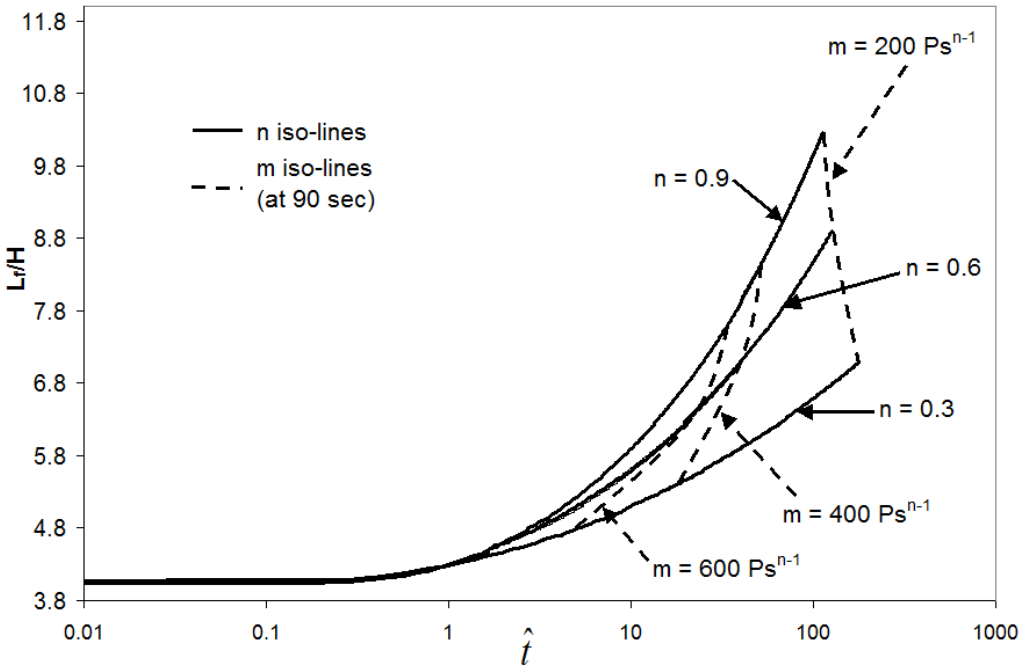

Figure 5.11. Non-dimensional parameter study of 3-D numerical power-law model, showing the dependence of axial spreading on the ratio of gravity to viscous forces. This figure relates axial spreading to the ratio of gravity to non-Newtonian viscous parameters, which allows for the isolation of certain parameters during analysis. Note: $L_{front}/H \equiv$ ratio of axial spreading to characteristic height; $m \equiv$ consistency index [=] Ps^{n-1}; $n \equiv$ shear-thinning index; $t' \equiv$ ratio of gravity to viscous terms.

As seen in the 2-D numerical model, the relationship between the axial propagation and the ratio, $\hat{t}$, is constant for any consistency index along the shear-thinning iso-lines. By following a single *n* iso-line, one is able to eliminate a single variable from the analysis. For example, at a specific value of *m*, *n* and α, the fluid will spread up to a certain point: $t = t_1$ along the *n* iso-line. As *t* increases, axial spreading will follow that same iso-line regardless of *m*. Therefore, if given a specific *n* value, and a desired axial spreading, L_f, one could deduce how changes to *m* or α would impact axial spreading characteristics. It is also worth noting that the slope of a given curve can be used to find the instantaneous velocity of the moving contact line (Eq.(5.39)), which could be used to draw the same conclusions as above, but for the relationship between the inclination angle, rheological properties, and the velocity of the moving contact line.

$$\frac{\partial \hat{L}}{\partial \hat{t}} = \frac{m^{1/n}}{(\rho g \sin\alpha)^{1/n}} \left(\frac{1}{H}\right)^{\frac{1}{n}+1} V_f \qquad (5.39)$$

Influence of Power-law Parameters of Spreading Rate

The following parameter analysis examines how the change in velocity of the traveling front depends upon the power-law rheological parameters. I define a change-of-rate indicator, ζ, which represents the relative deviation of L_{front} vs t, from a completely linear (i.e. constant velocity) relationship

$$\xi = \frac{(A_{L_f} - A_s)}{A_s} \qquad (5.40)$$

where A_{L_f} is the area under the L_{front} vs t curve, and A_s is the area under the same curve assuming that it is a straight line (i.e. constant velocity). For example, if the velocity of the spreading front is more constant, then the change-of-rate indicator approaches zero.

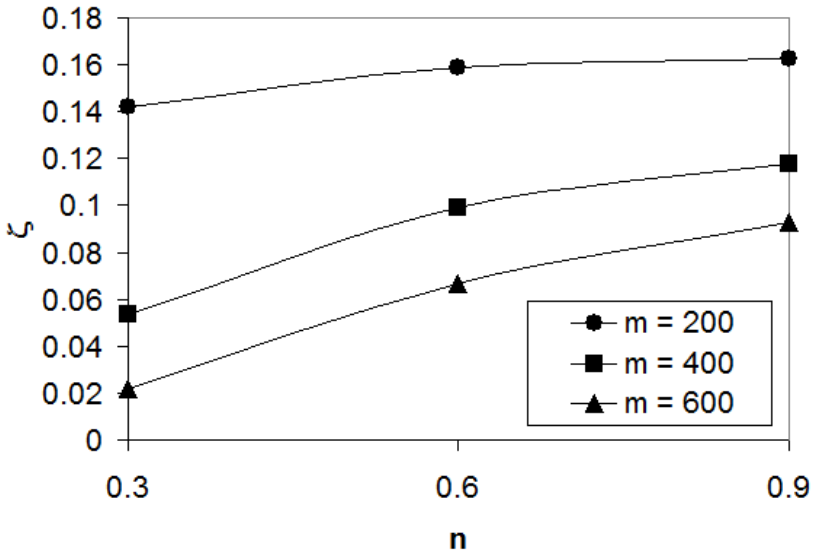

Figure 5.12. The effect of the shear-thinning index, n and the consistency index, m (Ps^{n-1}) on the change-of-rate indicator, ζ. This figure shows that as m increases and n decreases, axial spreading rate of the contact line approaches steady-state.

The parameter is larger if velocity is not constant. Figure 5.12 shows that both the consistency index and the shear-thinning index influence the acceleration and deceleration of the spreading front. According to Figure 5.12, minimizing the shear-thinning index would make the axial spreading profile more linear with respect to time (constant velocity), except for in cases where the consistency index is very low. In addition, increasing the consistency index would have the same effect of creating a more constant spreading velocity. These trends are in agreement with the ones found using the 2-D numerical model. *It should be noted that for all other factors kept equal, the change-of-rate indicator for a 3-D model would be higher than the 2-D model.*

Influence of Marginal Changes to Power-law Parameters on Axial Spreading

A percent change sensitivity analysis of the power-law parameters was conducted to determine the influence of small changes to *n* and *m* at different baseline values of *n* and *m*. This kind of sensitivity analysis could be used to predict how small changes to the power-law parameters, from things like delusion or temperature changes, will impact axial spreading for a given time. While it may appear from Figure 5.9 that small changes to the shear-thinning index will result in predictable behavior, a closer look reveals that the spreading response to these slight changes is actually quite complicated.

I define percent sensitivity of axial spreading, to percent changes in a power-law parameters, as Eq. (5.41), where $L_{front,\,original}$ is the value of L_{front} at 90 sec of spreading for a given power-law parameter (i.e. *n* or *m*), and $L_{front,\,cange}$ is the value of L_{front} at 90 sec of spreading after making a 10% change to the power-law parameter.

$$\frac{L_{front,\,change} - L_{front,\,original}}{L_{front,\,original}} \cdot 100\% \qquad (5.41)$$

The original values for L_{front} are presented in the axial spreading data in Figure 5.9 and 5.10. Figure 5.13 shows percent sensitivity of axial spreading to changes in the shear-thinning index. A gel with a large value of *m* and *n ~ 0.6* is most sensitive to small changes in *n.*

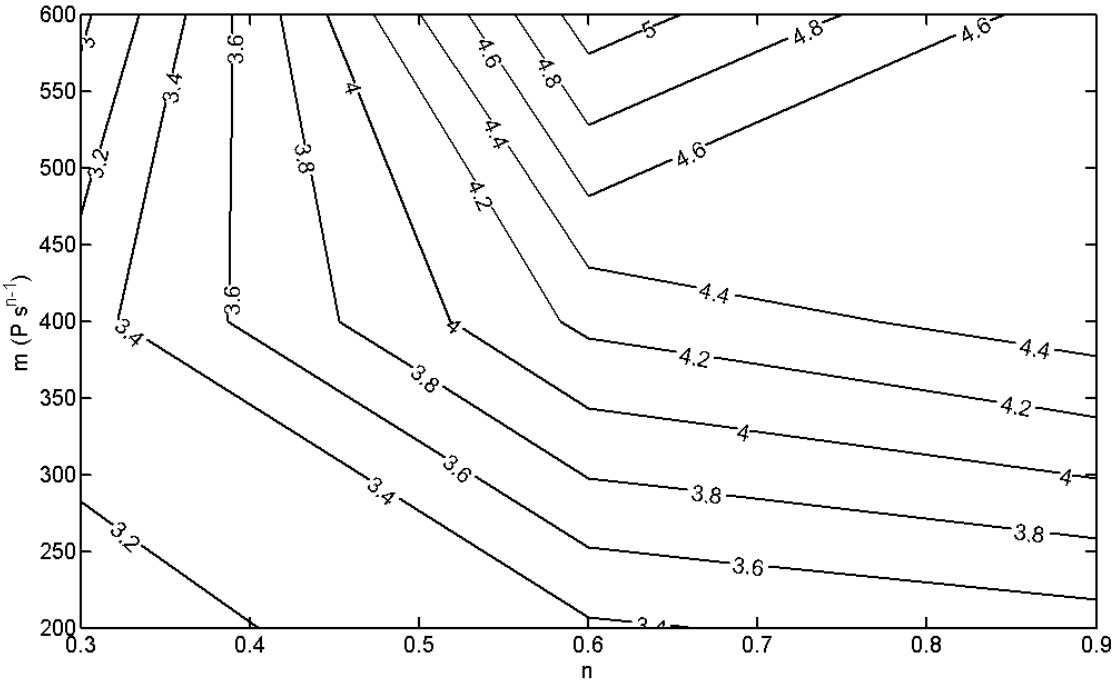

Figure 5.13. Contour lines showing percent (%) sensitivity of axial spreading (L_{front} (*t = 90sec*)) to 10% increase in *n*. This figure shows highest sensitivity at: *m~ 600 Ps*$^{n-1}$ and *n ~ 0.6*. Note: *m* ≡ consistency index [=] *Ps*$^{n-1}$; *n* ≡ shear-thinning index.

Figure 5.14 shows percent sensitivity of axial spreading to changes in the consistency index. Figure 5.14 shows that making 10% changes to *m* will result in the most drastic changes to axial spreading at lower values of *n* and *m*.

Figure 5.15 shows contour lines of percent changes to axial spreading after making 10% changes to *n (increase)* and *m (decrease)*. The contour lines show that the most evident increase in axial spreading occurred when changing *m* and *n* at mid ranges.

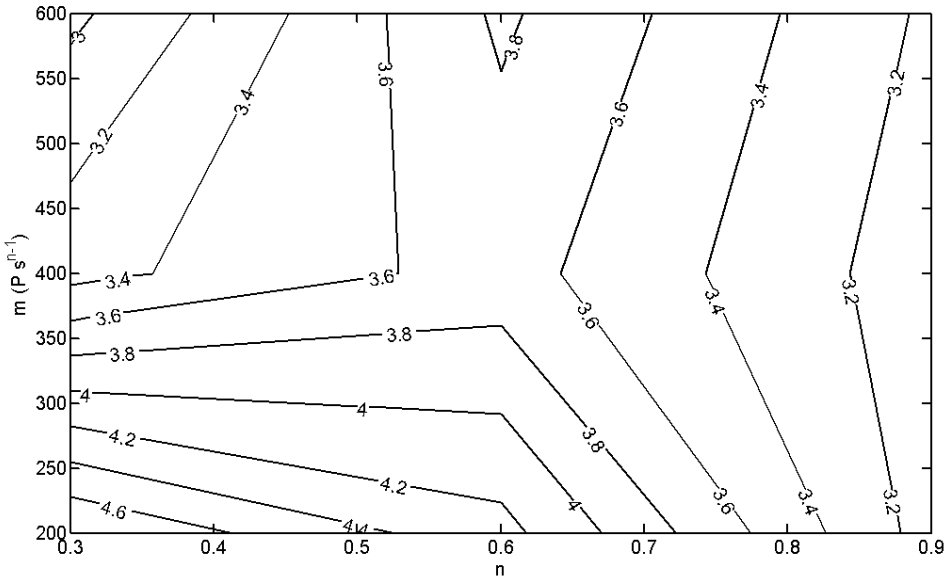

Figure 5.14. Contour lines showing percent (%) sensitivity of axial spreading ($L_{front}(t = 90sec)$) to 10% decrease in *m*. This figure shows highest sensitivity at: $m \sim 200\ Ps^{n-1}$ and $n \sim 0.3$. Note: *m* ≡ consistency index [=] Ps^{n-1}; *n* ≡ shear-thinning index.

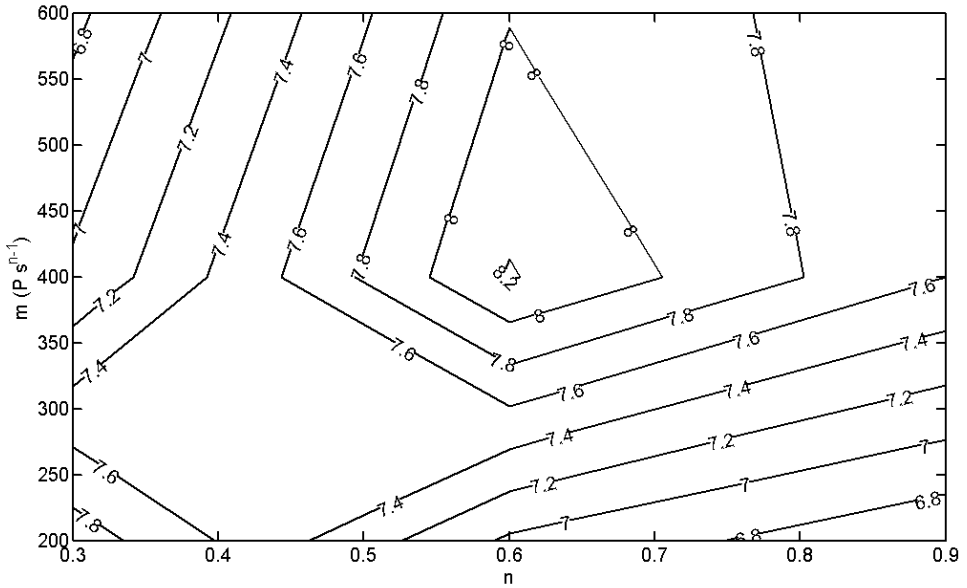

Figure 5.15. Contour lines showing percent (%) sensitivity of axial spreading ($L_{front}(t = 90sec)$) to 10% decrease in *m* and increase in *n*. This figure shows highest sensitivity at: $m \sim 400\ Ps^{n-1}$ and $n \sim 0.6$. Note: *m* ≡ consistency index [=] Ps^{n-1}; *n* ≡ shear-thinning index.

Discussion

2-D vs. 3-D numerical power-law model compared with experiment

Gravity-induced spreading simulated using the 3-D numerical model showed acceptable agreement with experiment. As hypothesized, it is a substantial improvement over the 2-D numerical model. The main area of concern is the fact that the 3-D numerical model seems to consistently have a greater initial velocity, but agrees well with the experiment at later times. Another point worth considering is the fact that the 3-D numerical model consistently overestimates spreading in the lateral direction. Both of these shortcomings could be a result of several factors, such as surface tension or an inadequate modeling of rheological parameters, that must be investigated in future work and will be further discussed later in the chapter.

Experimenting with different initial conditions

I compared numerical simulations using an approximate and an experimental (real) initial condition. Because the experimental initial condition might have drastic curvature at the spreading front, incorporating this geometry is challenging in terms of acquisition and computational efficiency. Nevertheless, neglecting the slope of the free surface at the leading edge has been found to directly contribute to inconsistencies between the computational model and experiment. The evolution equation is a function of the fluid's physical properties, but the evolution of the free surface is actually driven by the slopes at the free surface. Therefore, as the center of mass moves towards the leading edge, the slope of the free surface at the leading edge becomes steep enough to move the contact line. The time it takes for the center of mass to move to the leading edge and propagate the contact line is a source of error, referred to as the "waiting

time solution [52].” This phenomenon was observed for all nine simulations that used an approximate initial condition. Therefore, the second hypothesis is accepted.

When using a more accurate initial topography, a good time adaptation algorithm is recommended because the initial time step might need to be greatly reduced to facilitate convergence of Newton’s method. The time adaptation technique described in this document was straight foreword to implement and effective.

Starting simulation at t = 60 seconds

A direct comparison between the model and experimental spreading reveals that the computational model has an initial burst of velocity, which is not seen in the experiment. In order to rule out the shape of the initial condition as the primary cause of this inconsistency, I compared the two spreading profiles after setting the initial condition to be at: t = 60 seconds.

Figure 5.16 shows the spreading characteristics of a 3-D power-law model computing a 2.7% HEC gel, with initial conditions at different intervals of time. Previous data has compared to computations conducted using an initial topography obtained at the instant when the plunger broke contact with the gel, shows as the dashed line (same data as in Figure 5.6). This data is now being compared with a simulation that considered the initial condition at t = 60 seconds, shown as a solid line. Both plots show an overestimation of axial spreading at the onset, and improved comparison at later times. As a result, the lubrication approximation can be ruled out as a possible cause of the differences between model and experiment, and other factors such as the constitutive equation should be investigated.

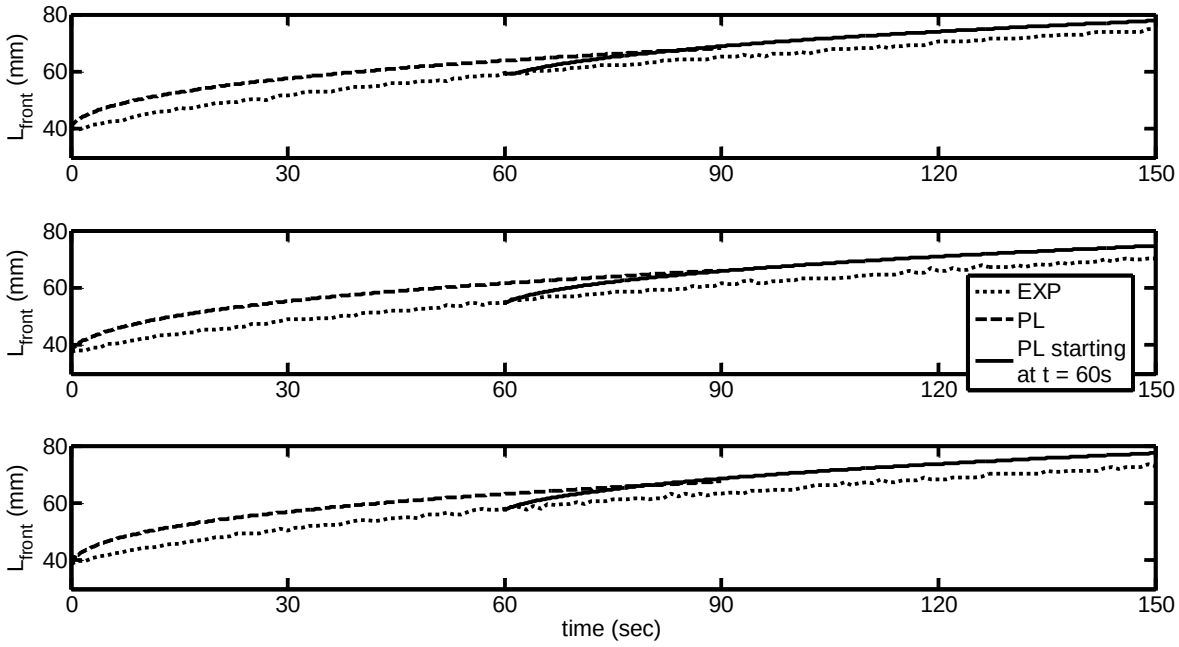

Figure 5.16. Original power-law model (dashed) vs. experiment (dotted) axial spreading data (seen in Figure 5.6) for a 2.7% HEC gel, compared with power-law model with initial condition starting at t = 60 seconds (solid). Starting with an initial condition at t = 60 seconds does not prevent the model overestimation of axial spreading at onset.

Sensitivity Analysis

In this study, I conducted a parameter study and sensitivity analysis to attempt to understand the relationship between the shear-thinning index, consistency index, and axial spreading characteristics. An in-depth understanding of these parameters and their influence on spreading can be a valuable tool for designing and optimizing a microbicide gel for maximum effectiveness.

It is straightforward to assume a direct link between both rheological parameters and axial spreading. I presented a sensitivity analysis showing that both the consistency index and the shear-thinning index have a direct impact on a spreading characteristics. For a microbicide design application, one would need to consider the fact that: *as the shear-thinning index*

decreases, the axial distance the fluid would spread in a given time will decrease. Also, as the consistency index decreases, the axial distance the fluid spreading in a given time would increase. Therefore, it appears that both parameters have an influence on spreading, but further analysis was conducted to determine the weight of each parameters contribution.

All the experimental and numerical data presented in this dissertation was limited to a single angle of inclination ($\alpha = 30°$). I presented a non-dimensional parameter analysis that introduces the relationship between axial spreading and the ratio of gravity to viscous forces.

An inconsistency between the compared experimental and theoretical data is the fact that there is an acceleration of the moving front in the numerical simulations, which is not seen in the experiment. In fact, experimental data shows minimal acceleration and deceleration during the experiment, for all three HEC concentrations. The parameter analysis presented in this document shows that the rate of axial spreading is directly a function of the power-law parameters. I conclude that the *velocity of the moving front becomes steady as the consistency index increases and the shear-thinning index decreases*. For a microbicide application, it might be desirable to use gels with constant velocity spreading characteristics. This would make approximating their spreading behavior very straightforward.

A study that investigates the sensitivity of axial spreading to marginal changes of the power-law parameters was completed to approximate how factors such as dilution would impact the gels expected spreading characteristics. This study concluded that *a gel's axial spreading behavior is most sensitive to 10% increase in n at large values of m and n ~ 0.6.* In addition, *a gel's axial spreading behavior is most sensitive to 10% decrease in m for very shear-thinning fluids at low values of m.* Finally, *a gel at approximately mid range (n ~ 0.6 and m ~ 400) would be most sensitive to simultaneous 10% changes of both n (increase) and m (decrease).* For a

microbicide application, research needs to be done to determine how diluting polymeric gels will influence power-law parameters. Once completed, this analysis can serve two purposes: (1) act as guide for approximate values necessary for fluids needed to spread in a specific way, and (2) forecast of how a given fluid might behave once it is introduced into an environment where it might be diluted by fluids in its surroundings. Given the limited rheological data presented in Chapter 2, 3.0% HEC would be most sensitive to simultaneous 10% changes in both *m* and *n.* Otherwise, none of the gels tested in this study would be expected to have an extreme sensitivity to changes in *n* or *m*.

This sensitivity analysis is done in the absence of surface tension; therefore we are able to isolate the effects of rheological properties on spreading characteristics. Because the current model will eventually be incorporated into a master model that accounts for shearing and squeezing forces, the inclusion of surface tension seems irrelevant. Nevertheless, in Chapter 7 I provide a detailed discussion of the possible impacts of including surface tension into the power-law numerical model.

Discussion of the evolution of flow for a numerical model:

For a Newtonian fluid, the evolution of the numerical height is strictly a function of the gradient of the free surface. Because the simulation has no sense of momentum (the calculations at each time step are only a function of the immediate surface topography), the driving factor for the flow is a function of the surface topography at the immediate time step. At the beginning of the simulation, the gradients of the free surface can be relatively high; therefore the maximum shear rate at those locations, and within the bolus, would also be high. As the free surface becomes smoother, the shear rate within the fluid also decreases causing the rate of spreading to

subside. This is seen in the L_{front} vs. t profile of the Newtonian numerical simulation. When considering a fluid with pseudoplastic rheological characteristics, as the free surface becomes smoother and the maximum shear rate within the bolus decreases, the apparent viscosity of the fluid would increase. This would further add to the deceleration of the spreading evolution.

The range of expected shear rates in a spreading bolus depend on the topography of the free surface and the shear-thinning index. Table 5.1 reports the maximum shear rate within a fluid for a typical simulation.

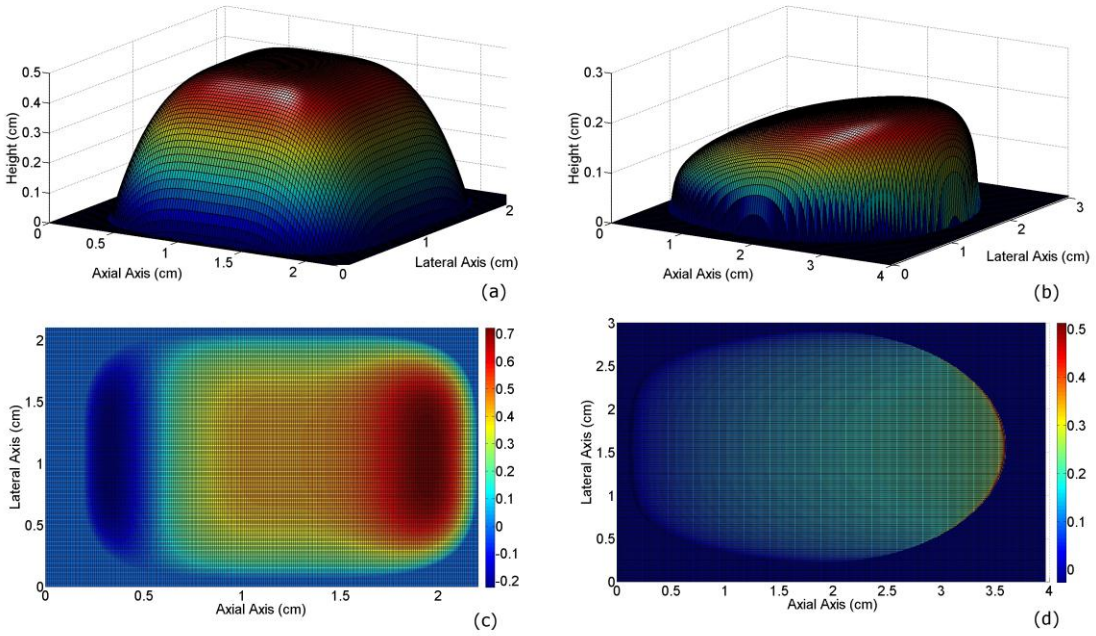

Figure 5.17. Visualization of shear rate within the spreading bolus. (a) Initial condition of the free surface topography. (b) The free surface after spreading for 90 seconds. (c) and (d) the shear rates, at z = 0.001 *cm*, (color bar - 1/s, where RED = max and BLUE = min) of the topographies in Figures a. & b., respectively. Input Parameters: $\alpha = 30°$, $n = 1$ (Newtonian), $m = 500$ P s^{n-1}. This figure shows that the highest shear rates are seen at the leading edge, near the spreading surface, and for this simulations are below ~ 1/s.

For these simulations, the upper bound for a possible shear rate within the fluid is approximately *1/s*. The lower bound could vary; therefore it is unclear whether accounting for a Newtonian plateau will prove to be advantageous.

When determining the power-law rheological parameters, *n* and *m* for a given HEC concentration, I fit to a larger range of the controlled shear rate ($\dot{\gamma} = [0.01,100]\ 1/s$) even though the numerical simulation might never encounter such high values. This results in a model that is not limited by the inclination angle, because a steeper angle would clearly increase the shear rate.

n	Time (sec)	$\gamma_{max}\|_{z = 0.001\ cm}$ (1/s)	$\gamma_{max}\|_{z = 0.4\ cm}$ (1/s)
1	0	0.72	0.1
	90	0.51	---
0.5	0	0.48	0.01
	90	0.09	---
0.1	0	0.10	10^{-9}
	90	2.6e-5	---

Table 5.1. Expected ranges of shear rate for a spreading bolus evaluated at a different time, hear-thinning index, and elevation along the *z-axis* (the fluid depth). Input Parameters: $\alpha = 30°$, *m* = 500 P s^{n-1}, *n = 1*.

Future Work

There are several improvements that could add to the accuracy and effectiveness of this numerical model:

1. Incorporating a constitutive equation that fits to the rheological data more closely (Chapter 6).
2. Accounting for the elastic storage of energy in the fluid.
3. Accounting for surface tension in the evolution equation.
4. Loosening the no-slip boundary condition – There is always the question of the influence of fluid-structure interaction on spreading. In most fluid mechanics

applications, analyzed on a macro scale, implementing the no-slip boundary condition is standard practice. Nevertheless, preliminary experiments and other literature [78] suggest that changing the spreading surface can drastically alter spreading characteristics. In Chapter 7, I will present some background for this complex issue, and possibly the importance of accounting for slip in the future.

5. An important note to consider is the fact that using the lubrication approximation becomes more justified at later times than for the initial time frame. If one considers the maximum height and length to be the characteristic values, the conditions:

   $H/L<<1$ and $\frac{\rho H^2}{\mu T}<<1$ become more accurate for later time points because the maximum height will decrease, and the maximum length and time will increase. This might be one of the explanations for why the theory matches the experiment better as time progresses. Nevertheless, this would be the last approximation that I would recommend for someone to reconsider because without it the math would become almost unmanageable and it is probably not contributing to a large amount of error when compared with the other approximations in this list.

Before investing time and effort into any of these endeavors, it is important to isolate a single factor that might result in the biggest improvement to the theoretical model. This concept is also not trivial. As I will show in the next chapter, implementing a different constitutive equation could either improve or worsen the model's agreement with the experiment, depending on how the equation's parameters are obtained.

Conclusions

In this chapter, I presented a numerical simulation of a finite bolus of power-law fluid spreading down an incline. The numerical simulation shows convergence to a single solution, as the spatial mesh is made finer. Also, the numerical solution shows good agreement with a similarity solution that was confirmed to satisfy the power-law evolution equation. This satisfied the engineering goal of the first sub-objective and the second overall objective of this work.

I used my computational simulation to determine the advantages of accounting for lateral slumping and an initial condition that more accurately resembles the experiment. I confirmed my first hypothesis that a 3-D numerical model does improve agreement with experiment over a 2-D numerical model, and my second hypothesis that incorporating a more accurate initial condition does result in better agreement with the experiment.

Finally, I completed the remaining engineering goals and sub-objectives of Objective 3, by completing a unique power-law parameter and parameter sensitivity analysis, which is directly applicable to developing and testing future microbicide delivery vehicle candidates.

While I am certainly not the first person to model the free surface spreading of power-law fluid, as far as I know this is the first numerical solution for the evolution of the free surface of a spreading power-law fluid. While others have documented this preliminary parameter analysis for Hershel-Bulkley fluid, and have done some simulations without a yield stress, the parameter and sensitivity analysis in this work is extensive and can be directly applied to microbicides. Moreover, the governing equations are solved using a numerical technique which is confirmed to conserve mass and agree with a similarity solution, and is an excellent framework for experimenting with other constitutive equations and boundary conditions.

Chapter 6 THE ELLIS MODEL

Introduction

Achieving our group's long-term goal means developing a microbicide delivery vehicle with desired spreading characteristics. To do this it is necessary to develop a math model that can account for non-Newtonian viscous forces. This chapter will address the second overall objective: to develop a numerical model of a non-Newtonian fluid spreading, in 3-dimensions, due to gravity.

Significance and Chapter Goals

A technique was outlined in Chapter 5 that resulted in a 3-D power law numerical model capable of simulating shear-thinning flow. A drawback of the evolution equation was the use of a constitutive equation that did not account for Newtonian plateaus in the rheological data (refer to Chapter 2).

OBJECTIVE 4: Incorporate the Ellis constitutive equation into the 3-D numerical model developed in Chapter 4.

The hypothesis of this objective is that, because the Ellis model considers the Newtonian plateaus in the rheological data, its spreading results will match the experiment closer than the power-law model.

> **Sub-Objective 4.1: Derive an evolution equation, in 3-D, using the Ellis constitutive equation and solve it using the numerical method developed in Objective 2.**

The engineering goals of this sub-objective are to derive an evolution equation with Ellis parameters that includes axial and lateral fluxes, and solve it numerically, to be used in later sub-objectives.

Sub-Objective 4.2: Perform numerical simulation for 2.4%, 2.7% and 3.0% HEC gels using the 3-D power-law and Ellis code (using exact IC) with rheological parameters obtained by fitting to the viscometric data, and compare the spreading characteristics of each simulation with its experimental counterpart.

The hypothesis of this sub-objective is that the Ellis code will match the experimental spreading characteristics better than the power-law code.

The engineering goal is to run the simulations and determine if it is more beneficial to perform computational simulations of HEC spreading using the Ellis constitutive equation.

Sub-Objective 4.3: Perform a rigorous Ellis parameter sensitivity analysis and document the impact of rheological parameters and axial spreading.

The engineering goal of this aim is to perform a parameter study of the Ellis numerical model and provide a framework for predicting how changes to the three Ellis parameters would impact axial spreading, which could be useful for numerous applications in addition to microbicides.

This work includes several novel contributions to advance the field of microbicide development and free surface fluid dynamics. As far as I know, this thesis contains the original derivation of the free surface evolution equation of an Ellis fluid. As a result, this is also an original numerical solution of this equation. Using the numerical solution, I will show how the

Ellis parameters influence axial spreading, which is useful for any application in addition to microbicide development.

Review of Relevant Literature

For a review of relevant literature discussing Ellis rheology and using the Ellis constitutive equation in spreading models please refer to the introductions of Chapters 2 and 4, respectively.

Methods

Evolution Equation for a Free Surface Flow

The mathematical model presented in this chapter simulates a gel coating the vaginal epithelium as a finite bolus of a Ellis fluid spreading down an incline. The fluid is analyzed using the conservation of linear momentum combined with the Ellis constitutive equation, which is an improvement over the power-law because it accounts for the Newtonian plateau observed for HEC fluids at low shear rates.

Implementing a similar approach as for the Newtonian (Chapter 4) and power-law (Chapter 5) models, I start by solving the conservation of linear momentum (Eq. (6.1)) where $\tilde{v}$ and $\tilde{g}$ are the velocity and gravity vectors respectively, $\tilde{\tau}$ is the shear stress tensor, p is the pressure and ρ is the density. The analysis presented in this chapter deviates from the Newtonian model after the Ellis constitutive equation is introduced, particularly because writing out the tensor invariants results in a function of two tangent vectors.

$$\frac{d\tilde{v}}{dt} + (\tilde{v} \cdot \nabla)\tilde{v} = -\frac{1}{\rho}\nabla p + \frac{1}{\rho}\nabla \cdot \tilde{\tilde{\tau}} + \tilde{g} \qquad (6.1)$$

The velocity vector $\tilde{v}$ is broken down into its Cartesian coordinates: *u*, *v*, *w* in the *x*, *y*, *z* directions respectively. The same assumptions are made as in Chapter 4:

1. Thin-film Approximation (Appendix A1)
2. No slip at the sliding surface
    a. Boundary Condition *1: u(z = 0) = v(z = 0) = 0*
3. The free surface of the gel is exposed to ambient air at pressure p_o.
    a. Boundary Condition 2: at $z = h(x,y,t) \rightarrow \tau_{zx} = \tau_{zy} = 0$
    b. Boundary Condition 3: at $z = h(x,y,t) \rightarrow p = p_o$

After incorporating the thin-film approximation, and keeping only the relevant stress components, the momentum equation (Eq. (6.1)) is reduced to three governing equations of motion where α is the angle of the ramp with respect to the horizontal (Figure 5.1).

$$\text{x-direction: } 0 = -\frac{dp}{dx} + \frac{d\tau_{xz}}{dz} + \rho g \sin\alpha \qquad (6.2)$$

$$\text{y-direction: } 0 = -\frac{dp}{dy} + \frac{d\tau_{yz}}{dz} \qquad (6.3)$$

$$\text{z-direction: } 0 = -\frac{dp}{dz} - \rho g \cos\alpha \qquad (6.4)$$

The pressure term is derived using Eq. (6.4) and Boundary Condition 3.b, where p_o is the pressure at the free surface and gets cancelled out during integration.

$$p = [\rho g \cos\alpha][h(x,y,t) - z] + p_o \qquad (6.5)$$

In this chapter the fluid will be modeled using the 3-D Ellis constitutive Equation that relates the viscosity to the second invariant of the stress tensor, $\text{II}_\tau = \sqrt{\tau_{xz}^2 + \tau_{yz}^2}$:

$$\frac{1}{\eta} = \frac{1}{\eta_0}\left(1 + \left|\frac{\text{II}_\tau}{\tau_{1/2}}\right|^{\lambda-1}\right) \qquad (6.6)\ [88]$$

In Eq. (6.6), η_0 is the zero shear rate viscosity, λ is the measure of shear-thinning behavior, and $\tau_{1/2}$ is the stress at which the apparent viscosity has dropped to half its zero value. The relevant components of the stress tensor are presented in Eq. (6.7) and (6.8).

$$\tau_{xz} = \eta(\text{II}_\tau)\frac{\partial u}{\partial z} \qquad (6.7)$$

$$\tau_{yz} = \eta(\text{II}_\tau)\frac{\partial v}{\partial z} \qquad (6.8)$$

The equations for the relevant stress components are derived using Eq. (6.2) and (6.3) along with Boundary Condition 3.b, to express stress as a function of *h(x,y,t)*, which will be presented simply as *h*. Constant T_1 and T_2 are also introduced and will be used in subsequent expressions.

$$\tau_{xz} = (\rho g \cos\alpha)\left(\frac{\partial h}{\partial x} - \tan\alpha\right)(z-h) = T_1(z-h) \qquad (6.9)$$

$$\tau_{yz} = \left(\rho g \frac{\partial h}{\partial y}\cos\alpha\right)(z-h) = T_2(z-h) \qquad (6.10)$$

Plugging Eq. (6.9) and (6.10) into Eq. (6.7) and (6.8) results in two simultaneous equations that require algebraic manipulation to solve for an expression for the relevant shear rates: $\frac{\partial u}{\partial z}$ and $\frac{\partial v}{\partial z}$. Integrating each shear rate with respect to *z*, and using the no-slip boundary condition, results in an expression for velocity in the axial and lateral directions.

$$u = \frac{T_1}{2\eta_o}\left[\frac{1}{2}z^2 - hz + \left(\frac{\sqrt{A}}{\tau_{1/2}}\right)^{\lambda-1}\left(\frac{1}{\lambda+1}\right)\left((z-h)^{\lambda+1} - (-h)^{\lambda+1}\right)\right] \tag{6.11}$$

Only velocity in the axial direction is presented here (Eq. (6.11)), where $A = T_1^2 + T_2^2$. The expression for lateral velocity is identical, but with T_1 replaced with T_2. Integrating the velocities in the axial and lateral directions, using Eq. (6.12), I find the mass flow rate per unit width (Eq. (6.13) and (6.14)).

$$q_x = \int_0^{h(x.y.t)} u(x,y,t)\,dz \qquad\qquad q_y = \int_0^{h(x.y.t)} v(x,y,t)\,dz \tag{6.12}$$

$$q_x = -\left(\frac{\rho g\cos\alpha}{2\eta_0}\right)\left(\frac{\partial h}{\partial x} - \tan\alpha\right)\left[\frac{h^3}{3} + \left(\frac{\rho g\cos\alpha}{\tau_{1/2}}\right)^{\lambda-1}\left(\frac{1}{\lambda+2}\right)\left\{\left(\frac{\partial h}{\partial x} - \tan\alpha\right)^2 + \left(\frac{\partial h}{\partial y}\right)^2\right\}^{\frac{\lambda-1}{2}} h^{\lambda+2}\right] \tag{6.13}$$

$$q_x = -\left(\frac{\rho g\cos\alpha}{2\eta_0}\right)\left(\frac{\partial h}{\partial y}\right)\left[\frac{h^3}{3} + \left(\frac{\rho g\cos\alpha}{\tau_{1/2}}\right)^{\lambda-1}\left(\frac{1}{\lambda+2}\right)\left\{\left(\frac{\partial h}{\partial x} - \tan\alpha\right)^2 + \left(\frac{\partial h}{\partial y}\right)^2\right\}^{\frac{\lambda-1}{2}} h^{\lambda+2}\right] \tag{6.14}$$

Plugging Eq. (6.13) and (6.14) into the conservation of mass (Eq. (6.15)), I arrive at the evolution equation for an Ellis fluid that will be solved numerically for *h(x,y,t)*.

$$\frac{dh(x,y,t)}{dt} + \frac{dq_x}{dx} + \frac{dq_y}{dy} = 0 \tag{6.15}$$

Numerical solution of the Ellis evolution equation

Eq. (6.15) was solved using the numerical techniques outlines in Chapter 4 and 5, and was discretized according to Eq. (6.16),

$$\frac{dh(x,y,t)}{dt} + \mathrm{T}\left(\frac{q_{(x)k+M/2} - q_{(x)k-M/2}}{\Delta x} + \frac{q_{(y)k+1/2} - q_{(y)k-1/2}}{\Delta y} \right) = 0 \qquad (6.16)$$

where $\mathrm{T} = -\dfrac{\rho g \cos\alpha}{2\eta_o}$. The spreading domain was divided into *N* points along the axial direction and *M* points along the lateral direction (Figure 5.2). Each flux term was discretized about the half-node using central difference approximations, and just as for the power-law model, each axial flux contained a $\partial h/\partial y$ term, and each lateral flux contained a $\partial h/\partial x$ term (defined as perpendicular derivatives in this document). In an effort to satisfy the conservation of mass, the "perpendicular derivative" terms were discretized according to the strategy described in Chapter 5.

$$q_{K+M/2} = \mathrm{T}\left(\frac{h_{K+M} - h_k}{\Delta x} - \tan\alpha \right) \left[\frac{(h_K^3 + h_{K+M}^3)}{6} + B\left\{ \left(\frac{h_{K+M} - h_k}{\Delta x} - \tan\alpha \right)^2 + \left(\frac{h_{K+M+1} - h_{K+M-1}}{2\Delta y} \right)^2 \right\}^{\frac{\lambda-1}{2}} \left(\frac{1}{2} h_K^{\lambda+2} + \frac{1}{2} h_{K+M}^{\lambda+2} \right) \right] \qquad (6.17)$$

$$q_{K-M/2} = \mathrm{T}\left(\frac{h_k - h_{K-M}}{\Delta x} - \tan\alpha \right) \left[\frac{(h_K^3 + h_{K-M}^3)}{6} + B\left\{ \left(\frac{h_k - h_{K-M}}{\Delta x} - \tan\alpha \right)^2 + \left(\frac{h_{K+1} - h_{K-1}}{2\Delta y} \right)^2 \right\}^{\frac{\lambda-1}{2}} \left(\frac{1}{2} h_K^{\lambda+2} + \frac{1}{2} h_{K-M}^{\lambda+2} \right) \right] \qquad (6.18)$$

$$q_{K+1/2} = \mathrm{T}\left(\frac{h_{K+1} - h_K}{\Delta y} \right) \left[\frac{(h_K^3 + h_{K+1}^3)}{6} + B\left\{ \left(\frac{h_{K+1+M} - h_{K+1-M}}{2\Delta x} - \tan\alpha \right)^2 + \left(\frac{h_{K+1} - h_K}{\Delta y} \right)^2 \right\}^{\frac{\lambda-1}{2}} \left(\frac{1}{2} h_K^{\lambda+2} + \frac{1}{2} h_{K+1}^{\lambda+2} \right) \right] \qquad (6.19)$$

$$q_{K-1/2} = \mathrm{T}\left(\frac{h_K - h_{K-1}}{\Delta y} \right) \left[\frac{(h_K^3 + h_{K-1}^3)}{6} + B\left\{ \left(\frac{h_{K+M} - h_{K-M}}{2\Delta x} - \tan\alpha \right)^2 + \left(\frac{h_{K+1} - h_K}{\Delta y} \right)^2 \right\}^{\frac{\lambda-1}{2}} \left(\frac{1}{2} h_K^{\lambda+2} + \frac{1}{2} h_{K-1}^{\lambda+2} \right) \right] \qquad (6.20)$$

Applying Eq. (6.16) to every point on the numerical domain will result in TOT non-linear equations with TOT unknowns. The non-linear system was solved using Newton's method set to converge as the first norm of the height changes falls below 10^{-9}. Each iteration of Newton's

method solved a linear system of equations using the P-BiCG method, set to converge as the second norm of the residuals fell below 10^{-6}. In the event that either Newton's method or the P-BiCG method did not converge within 10 and 100 interaction, respectively, a time adaptation was completed, which is described in detail in Chapter 4.

Mesh Convergence Study

A mesh convergence study, identical to the one described in Chapter 4, was completed for the Ellis numerical code. In order to verify that the Ellis parameters would not interfere with the convergence of the numerical method, the study used typical parameters that might be encountered in a microbicide application.

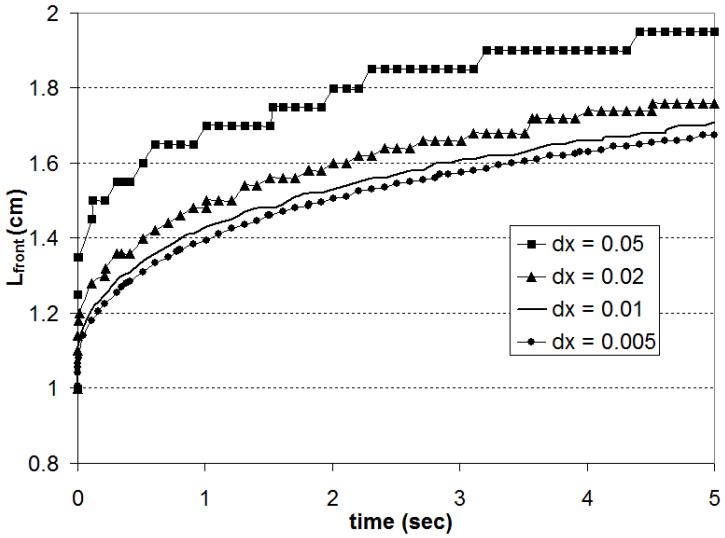

Figure 6.1. Convergence of Axial Spreading (L_{front}) as a function of time, for varying *dx* (*dy* kept constant). This figure shows axial spreading convergence with decreasing mesh size for each time point of the simulation. Input Parameters: ($\alpha = 30°$, dy = 0.01, Δt – adapted, $m = 707.11$ Ps^{n-1}, $n = 0.5$ $\varepsilon_{NEWT} = 10^{-9}$, $\varepsilon_{BiCG} = 10^{-6}$)

This convergence study is identical to the one performed for the Newtonian and power-law numerical models, and the results also appear to be similar. In fact, the Newtonian code showed that convergence in the lateral direction is similar to the axial direction. I assumed that because

the Ellis code showed clear convergence in the axial direction, almost identical to the Newtonian code, it would show the same convergence in the lateral direction.

The Ellis numerical model is showing order, just like the Newtonian and power-law models. The solution of axial spreading seems to converge to a specific solution, as the mesh in the axial direction is made finer. Just like for the power-law model, for the remainder of this chapter I perform all simulations using $dx = dy = 0.01$, which provided results with acceptable accuracy (within 1mm of finer mesh sizes), without a substantial burden on computational performance.

Validating the Numerical Solution

An advantage of the power-law numerical model was that comparing it with a known Newtonian solution easily validates it. The Ellis constitutive equation has common parameters with the power-law constitutive equation, but there is no straightforward way of matching the Ellis parameters to the power-law model in order to validate the computation. The Ellis code conserved volume throughout the simulation with 0.001%, regardless of the duration of spreading, which is a good way of confirming that numerical error is not accumulating. One option for validating the actual numerical solution is to derive an analytical solution to Eq. (6.15) that can be used to compare the free surface of both solutions.

Derivation of the Similarity Solution

To simplify the original evolution equation, I neglect any diffusive spreading and assumed: $\tan \alpha >> (\partial h/\partial x)$, as is seen for a very steep inclination angle or smooth topography. Note that because I neglect diffusive spreading, this becomes a 2-D problem with all spreading occurring in the axial direction. The original evolution equation (Eq. (6.15)) is simplified to:

$$\frac{\partial h}{\partial t}+\frac{\rho g\sin\alpha}{2\eta_o}\left[h^2+\left(\frac{\rho g\sin\alpha}{\tau_{1/2}}\right)^{\lambda+1}h^{\lambda+1}\right]\frac{\partial h}{\partial x}=0 \tag{6.21}$$

Eq. (6.21) takes the form of a non-linear advection equation, which can be solved by setting the characteristic equation to:

$$\frac{\partial x}{\partial t}=\frac{\rho g\sin\alpha}{2\eta_o}\left[h^2+\left(\frac{\rho g\sin\alpha}{\tau_{1/2}}\right)^{\lambda+1}h^{\lambda+1}\right] \tag{6.22}$$

This method for solving these types of equations was originally introduced by Huppert [55] for a Newtonian fluid. The solution of Eq. (6.22) is *x(t)*, where *h(x(t),t)* is a constant that is restricted to a characteristic curve. After integrating Eq. (6.22), it become evident that it is not possible to explicitly solve for *h(x,t)*. Therefore, I used Newton's method to solve for *h* at discrete points along the axial axis, at a given time. The convergence criteria for each solution of Newton's method is when the first norm of the residuals falls below 10^{-15}.

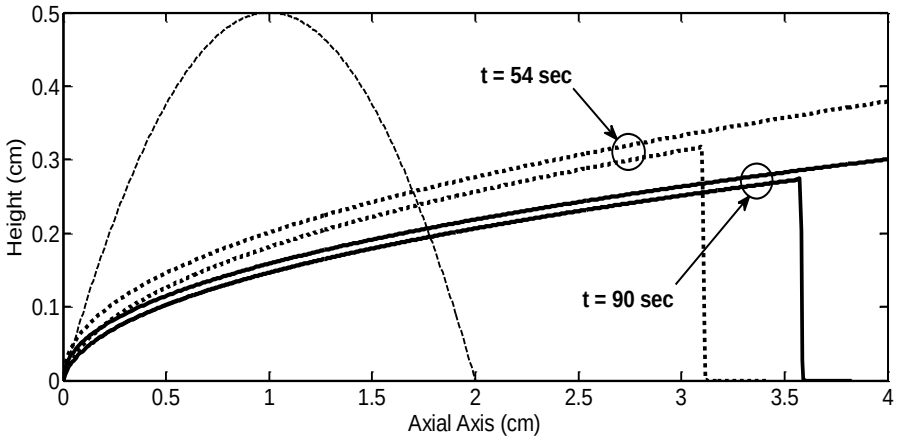

Figure 6.2. Comparison of height profile, at 54 sec (dashed) and 90 sec (solid) of spreading, obtained from the Ellis numerical model and Ellis similarity solution. Agreement between the numerical and similarity solutions is improved at as $t\to\infty$. Input parameters for both solutions: $\alpha=1.55rad$, $\eta_o=1000\,P$, $\tau_{1/2}=600\,Dyne/cm^2$, $\lambda=1.5$.

Because the 3-D numerical model will result in a singularity if it is computed at $\alpha = \pi/2$, some diffusive elements contributed to spreading. Nevertheless, after 15 seconds of spreading, the numerical solution seems to agree with the similarity solution within approximately 0.5*mm*, and this agreement is improving as spreading time increases, as can be seen for the comparison at 25 *sec* of spreading. This result is encouraging because the analytical solution becomes more accurate as: $t \rightarrow \infty$, and the diffusive components of the numerical solution are minimized.

Results

Each numerical simulation was carried out on the ITTC computing cluster at the University of Kansas. For 90 seconds of spreading, the 3-D Ellis simulations required approximately 120 hours of CPU time. The Ellis constitutive equation incorporated into the numerical model results in surface evolution topographies similar to the Newtonian and power-law models. As with the other models, the spreading characteristics of the Ellis model are strongly dependent on the rheological parameters: η_o, $\tau_{1/2}$, and λ.

Comparison of how fitting rheology technique impacts the numerical solution when compared with experiment

As was explained in Chapter 2, there were several rheometry options for obtaining the Ellis rheological parameters from fitting to the HEC data. Simulations ran with parameters obtained from using each rheometry technique would result in, sometimes, drastic changes to the axial spreading characteristics. Therefore, I present data for the spreading characteristics obtained from using each fitting technique: T1 – T4. Table 6.1 shows sample data for a 2.7%HEC gel along with a short explanation of each rheometry technique.

Rheometry Technique	Description	η_o (Poise)	$\tau_{1/2}$ (Dyne/cm^2)	λ	R^2
T1	Least-squares fitted to the residuals	1813.00	151.40	2.045	0.9950
T2	Least-squares fitted to the log of the residuals	1370.50	331.70	2.700	0.9888
T3	Relationship between power-law and Ellis (Eq. (2.6))	1370.50	61.41	1.800	0.8320
T4	Fitted with shear rate vs. stress form of the Ellis equation (Eq. (2.4))	1590.00	174.01	2.461	0.9925

Table 6.1. Summary of rheometry techniques and their values for a 2.7% HEC gel.

Figure 6.3 shows a comparison of the spreading simulations when using different input parameters, obtained from different strategies for obtaining rheological data. Each plot contains experimental spreading data to determine which rheology technique results in a more accurate simulation.

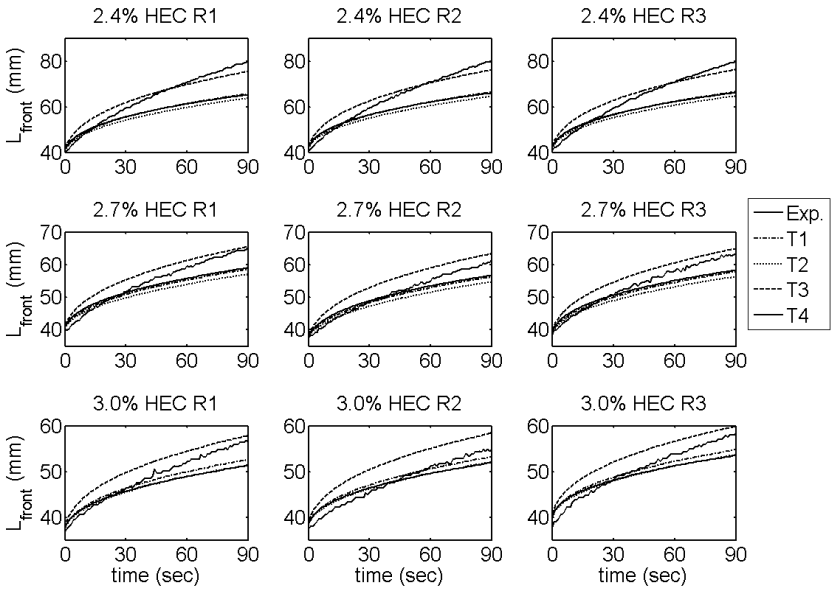

Figure 6.3. Comparison of axial spreading (L_{front}) of 9 experimental runs (3 runs of 2.4%, 2.7%, and 3.0% HEC concentration), and 9 numerical simulations, each using different Ellis data, that used the corresponding experimental initial condition obtained in Chapter 3. The T3 technique produces best agreement with experiment.

It appears that technique's: T1, T2, and T4, spreading solution underestimates the experimental data, especially for fluids with a lower HEC concentration. The rheology technique: T3, slightly overestimates experimental spreading for 2.7 and 3.0 % HEC concentrations, while underestimating spreading at later times for 2.4% HEC gels. In all cases, regardless of the technique, the initial spreading rate of the numerical simulations is larger than the experiment.

The 3-D power-law and Ellis numerical models compared with Experiment

Figure 6.4 presents comparisons of the spreading characteristics of: the 3-D Ellis numerical model, 3-D power-law numerical model, and the experiment. The Ellis model is showing similar spreading traits to the power-law model. In both cases, the velocity of the leading edge appears to reach a plateau at a similar point in the spreading process, although the Ellis model is in slightly better agreement with experiment.

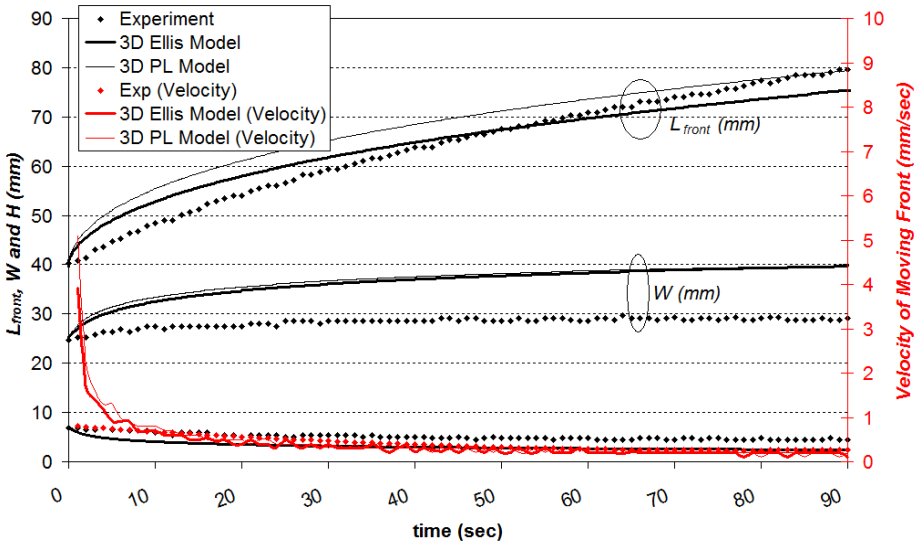

Figure 6.4. Sample spreading characteristics (black) and the axial velocity of the moving front (red) for a sample 2.4% HEC R1 with experimental IC. **Black (Left axis):** Axial (L_{front}) and lateral (W) spreading as a function of time for 3-D power-law and Ellis models, and experiment. **Red (Right axis):** Velocity of the moving front as a function of time for 3-D power-law and Ellis models, and experiment. There is not a noticeable difference between the two models.

For both the Ellis and power-law models, lateral spreading characteristics appear to be practically identical and both overestimate the lateral spreading observed in the experiment. The experiment shows slight lateral spreading at the beginning of the spreading process, and quickly approaches a plateau. Both numerical models also appear to be approaching a plateau, but at 90 seconds of spreading, there is approximately a 1*cm* difference between the theory and the experiment.

Figure 6.5 shows a comparison of the power-law and Ellis models with all 9 experiments. When considering a T3 rheology technique, the Ellis model slightly improves agreement with experiment when compared to the power-law model. In all cases, the comparison of the power-law and Ellis model shows that the final rate of spreading is practically identical, but the Ellis simulations show a slight decrease in the initial spreading rate, which results in a closer fit to experiment at later times.

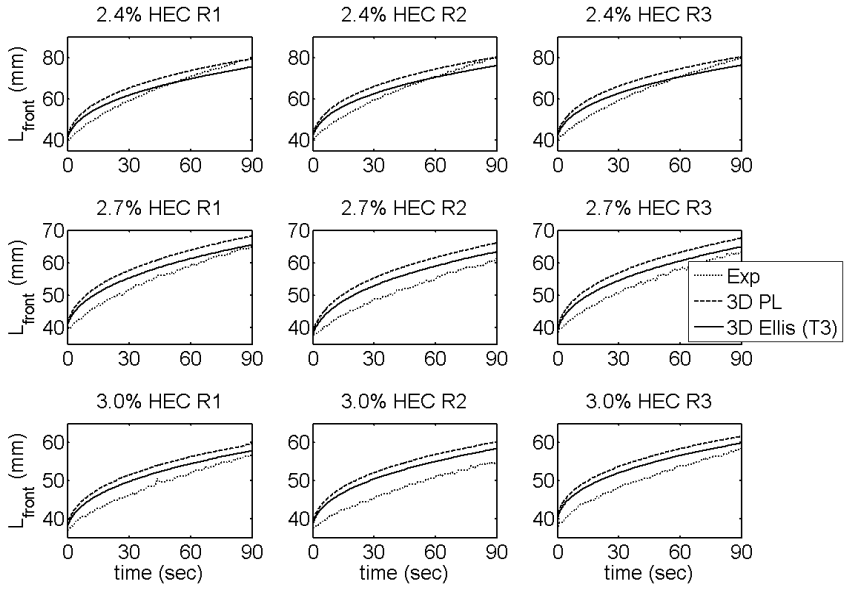

Figure 6.5 Comparison of axial spreading between the 3-D Ellis model and power-law model for 9 experimental runs. All nine runs show a slight improvement in the comparison with experiment for the Ellis model. Shown, with each row of plots at different scales, is the: experiment (dot), 3-D numerical power-law model (solid), 3-D numerical Ellis model (dashed) with T3 technique for obtaining rheology values.

Parameter study of the Ellis rheological parameters

A detailed sensitivity analysis of the Ellis parameters gives insight into the complex relationship between the three parameters of the model and spreading characteristics. The simulations shown in Figures 6.6 and 6.7 present a parameter study of the Ellis parameters, and their influence on axial spreading. Each simulation was completed using an initial condition identical to the one used for the power-law sensitivity analysis (Chapter 5). L_{front} of the initial condition was 2*cm*, and each simulation was computed for 40 seconds of spreading.

Figure 6.6 shows that the highest values of axial spreading, for a 40 second simulation, occur at lowest values of all three Ellis parameters.

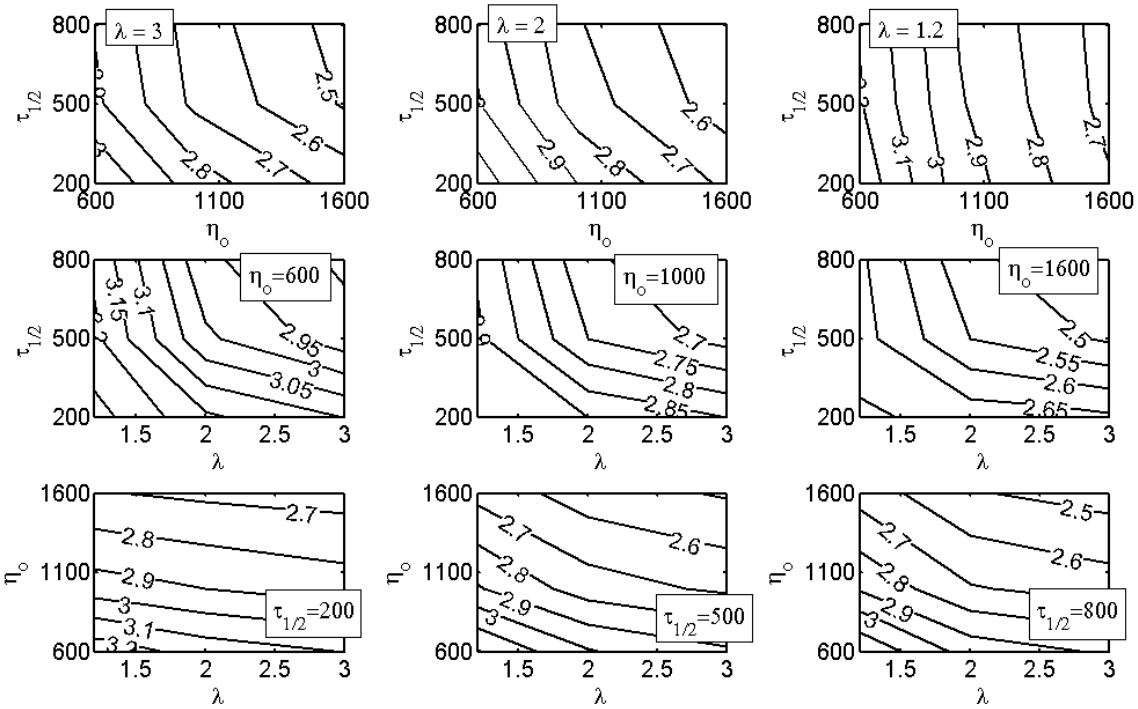

Figure 6.6. Contours show axial spreading (L_{front}) at 40 seconds for different parameter values. The **first row** plots show contours of L_{front} over a range of $\tau_{1/2}$ and η_0, at different values of λ. The **second row** plots show contours of L_{front} over a range of $\tau_{1/2}$ and λ, at different values of η_0. The **third row** plots show contours of L_{front} over a range of η_0 and λ, at different values of $\tau_{1/2}$. The contours in each plot are created using 9 data points, and interpolated using a built in MATLAB algorithm. Note: $\eta_o \equiv$ zero shear Newtonian viscosity plateau [=] Poise; $\tau_{1/2} \equiv \tau$ (1/2 η_o) [=] Dyne/cm^2; $\lambda \equiv$ measure of shear-thinning behavior.

The first row of Figure 6.6 shows that as λ becomes smaller (i.e. less shear-thinning), the contour plots become more linear and vertical for a relationship between $\tau_{1/2}$ and $\eta_{o,}$ indicating that changes in $\tau_{1/2}$ have little impact at low λ. The contour lines within the plot of $\tau_{1/2}$ vs. λ, appear to be practically unchanged for different values of η_o, indicating that η_o impacts axial spreading, but does not change overall dependence of axial spreading to $\tau_{1/2}$ and λ as η_o changes. Finally, as $\tau_{1/2}$ decreases, the contour plots for a η_o vs. λ relationship become more horizontal, suggesting that spreading becomes more independent of λ as $\tau_{1/2}$ decreases.

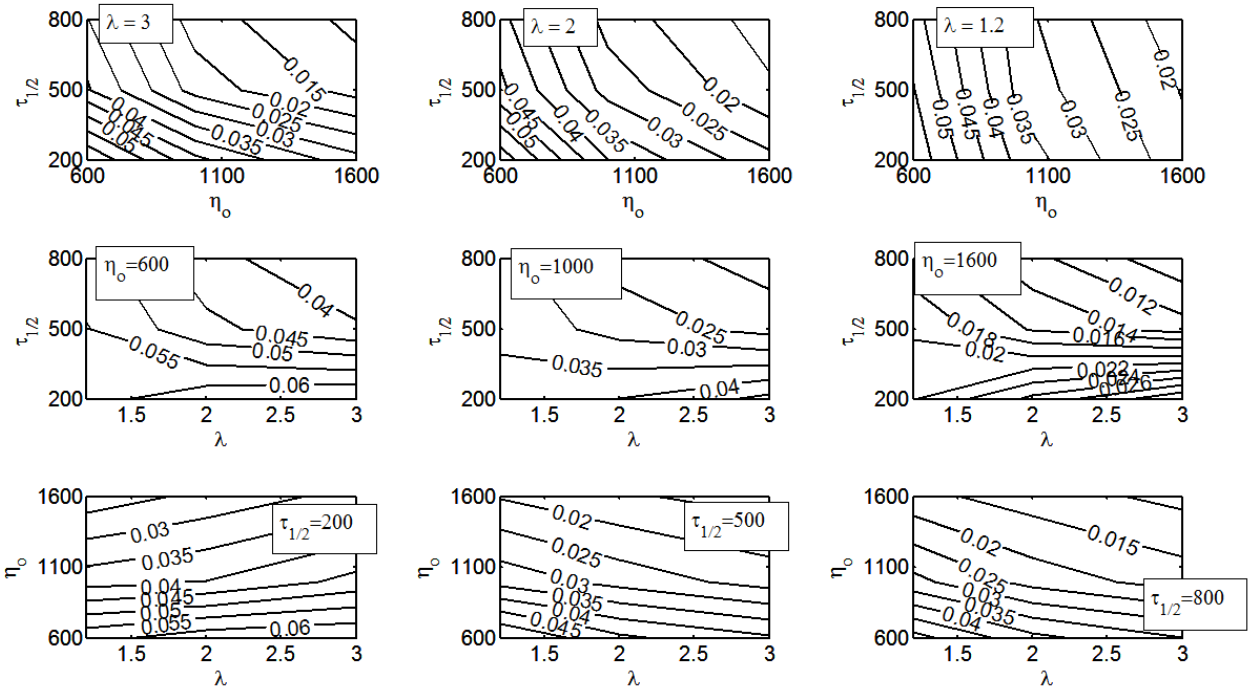

Figure 6.7. Contours show rate-of-change indicator at 40 seconds for different parameter values. The **first row** plots show contours of L_{front} over a range of $\tau_{1/2}$ and η_0, at different values of λ. The **second row** plots show contours of L_{front} over a range of $\tau_{1/2}$ and λ, at different values of η_0. The **third row** plots show contours of L_{front} over a range of η_0 and λ, at different values of $\tau_{1/2}$. The contours in each plot are created using 9 data points, and interpolated using a built in MATLAB algorithm. Note: η_o ≡ zero shear Newtonian viscosity plateau [=] Poise; $\tau_{1/2} \equiv \tau$ (1/2 η_o) [=] Dyne/cm^2; λ ≡ measure of shear-thinning behavior.

An important parameter to consider, when investigating the Ellis variables impact on spreading, is variation in the velocity of the leading edge. The data presented in Figure 6.7 computes the change-of-rate indicator, ζ, which represents the relative deviation of L_{front} vs t, from a completely linear (i.e. constant velocity) relationship.

Figure 6.7 shows that the lowest values of the curvature factor, implying constant velocity of the leading front for a 40 second simulation, occur at higher values of all three Ellis parameters. The first row of Figure 6.7 shows that as λ becomes smaller, the contour plots become more linear and vertical for a relationship between $\tau_{1/2}$ and η_o, indicating that at lower values of λ the rate of spreading becomes independent of $\tau_{1/2}$. The second row of Figure 6.7 shows that at higher values of η_o, the change-of-rate indicator will be smaller for a given simulation meaning the rate of spreading will stay more constant, but the impact of other variables cannot be excluded. Also, regardless of η_o, the contour lines become horizontal at higher values of λ, and smaller values of $\tau_{1/2}$, indicating that in that specific region the change-of-rate indicator is independent of λ.

Discussion and Conclusions

In this chapter I present the derivation and numerical solution of the evolution of the free surface of an Ellis fluid being perturbed by gravity. As the spatial mesh is made finer, the numerical solution converges to a single solution. Comparing the shape of the free surface with a similarity solution also validated the numerical solution. In Chapter 2, I considered 4 techniques for fitting the Ellis constitutive equation with the rheology data, and I present the results from using each technique in numerical simulations.

Different techniques for fitting to the rheological data

It appears that the rheological parameters obtained from using the fitting technique, T3, results in the best axial spreading agreement with experiment. For most of the other rheology techniques the spreading characteristics appear to be consistently underestimating the spreading in the axial direction, and especially underestimating the velocity of the leading edge for approximately the final 40 seconds of spreading. For that reason, it appears that the T3 technique, which obtains it's rheological parameters from their relationship to the power-law parameters and a measured low-shear rate viscosity, is the optimal choice for modeling gravity-induced spreading of HEC gels, and will be the data being discussed for the remainder of this chapter.

Comparing Ellis, power-law and experimental spreading characteristics

At the beginning of spreading, both models overshoot axial spreading rate when compared with experiment, but the Ellis model is a slight improvement over the power-law. As a result, the Ellis model slightly underestimates axial spreading at the later stages of the experiment, which could be interpreted as a more accurate estimate of the entire 90-second spreading process.

For both models, lateral spreading seems to considerably overestimate the experiment, and I can conclusively declare that switching to the Ellis constitutive equation possess no advantage in this respect. Possible solutions to this problem are discussed in Chapter 7 and might be implemented in future work.

The Ellis model provides an improvement over the power-law model, when comparing axial spreading with experiment. Nevertheless, this improvement comes from using rheology technique (T3) obtained from using a fitting strategy that yielded the worst R^2 values, implying

that either the constitutive equation is incomplete or some other driving factor is unaccounted for.

The result of my original hypothesis, that the Ellis constitutive equation would improve the theoretical agreement with experiment, remains inconclusive. It appears that the technique for obtaining the Ellis input parameters could dictate the efficacy of the computational model for predicting free surface HEC flow. Here I concluded that a T3 rheology technique does consistently show an improvement over the power-law model, for HEC gels, when considering flow in the axial direction. For a microbicide application, the prediction of the Ellis model could be a sufficient tool for performing in depth sensitivity analysis to predict the behavior of HEC flow after application. Nevertheless, considering a 3-parameter model, such as the Ellis, does not currently pose a clear advantage over the less complicated, 2-parameter, power-law model, which allows me to conclude that *when modeling HEC gels in the concentrations considered for microbicide application, accounting for the low-shear rate Newtonian viscosity does not improve the numerical models agreement with experiment*.

In order to improve the agreement between computational simulation and experiment, future work would need to incorporate one of the following improvements: (1) a different constitutive equation that accounts for the gel's elastic behavior, (2) surface tension, which might lessen the lateral slumping, (3) account for slip at the fluid-solid interface. This will be discussed in further detail in Chapter 7.

Ellis Model Parameters Study

Thorough parameter analyses of the Ellis model can provide insight into the complex interrelationship between the parameters themselves, and their impact on spreading characteristics. An understanding of this relationship can be useful for optimizing or predicting

the behavior of any fluid with a rheological relationship that fits well with an Ellis constitutive equation. Regardless of whether this may be useful for microbicide development, this kind of parameter analysis can be useful for understanding the role each parameter plays to contribute to a specific spreading profile.

The primary conclusion reached from the parameter analysis was that *decreasing each parameter will result in an increase in axial spreading*. Furthermore, *increasing each parameter will cause the spreading rate of the traveling front to remain more constant*. This is an important conclusion, but is somewhat oversimplified, as it does not explain the contribution of each variable or whether these conclusions are applicable to each scenario.

The parameter study was also useful for recognizing the fact that under certain conditions, changes to one Ellis parameter over another could cause minimal changes to axial spreading, but in another scenario changes to that parameter might considerably impact spreading characteristics. The contour plots for axial spreading indicated that as λ approaches unity, axial spreading appears to become independent of $\tau_{1/2}$. Moreover, the contour lines are getting steeper, implying that this spreading is becoming more dependent on η_o. This conclusions makes sense because as λ approaches unity, the fluid assumes a more Newtonian behavior, therefore most of the dependence of flow lies on the low-shear rate viscosity, which will not drastically change throughout the simulation. Also, at low values of $\tau_{1/2}$, the level of non-Newtonian behavior (λ) does not really matter; therefore axial spreading is mostly dictated by the value of η_o. For any application where it is of interest to know how changes to the Ellis parameters could impact spreading characteristics, Figure 6.6 could be used as a preliminary guide for making these estimations.

Figure 6.8 summarizes these results and presents a conceptual graphic intended to be a reference of how Ellis parameters impact spreading characteristics. As a fluid's properties approach the origin, axial spreading is increased and the rate of the spreading front will have lots of variation during the spreading process. By identifying where a given fluid lies on this plot, it is possible to predict how external factors, such as dilution, might impact spreading, but obviously the first step would need to be an understanding of how delusion impacts the Ellis rheological parameters. Assuming that a relationship between delusion and the Ellis properties are known, after identifying where a given gel might lie in Figure 6.8, one might be able to narrow down the gels behavior to 2 of the 3 parameters.

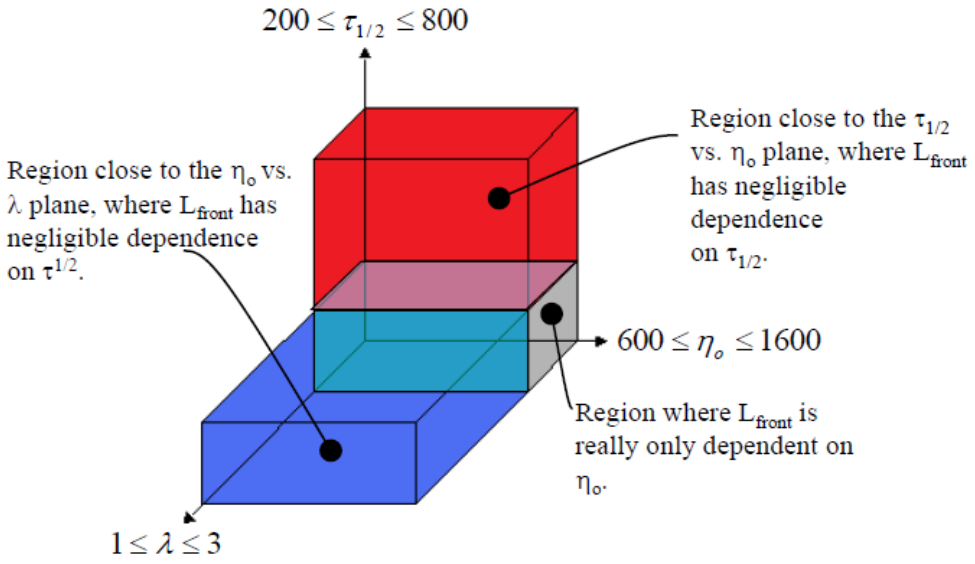

Figure 6.8. A preliminary interpretation of the Ellis rheological parameters and their impact on axial spreading. This figure is intended to give a guideline for predicting how changing a single parameter might influence spreading characteristics for a give fluid.

The contour plots of velocity changes show lines becoming vertical as λ approaches unity, suggesting that in this range the rate of axial spreading is independent of $\tau_{1/2}$. The second row of plots in Figure 6.7 simply reinforces the fact that the rate of spreading of the leading edge

becomes more constant as each of the three parameters increases. Even though the variation of the rate of spreading of the leading edge seems to increase as $\tau_{1/2}$ becomes smaller, its dependence on $\tau_{1/2}$ decrease. Furthermore, this dependence almost seems to become reversed as $\tau_{1/2}$ becomes very small. The nearly horizontal contours shown in the η_o vs. λ plots, for different values of $\tau_{1/2}$, reinforce that: for smaller values of η_o, the variation in the rate of axial spreading becomes independent of λ, regardless of $\tau_{1/2}$. Furthermore, at higher values of η_o, the relationship between η_o and λ becomes very dependant on $\tau_{1/2}$. In fact, if a constant rate of spreading were required, for smaller values of $\tau_{1/2}$, an increase to λ would require a corresponding increase to η_o to remain on the same contour line. The relationship at higher values of $\tau_{1/2}$ is completely reversed, whereas an increase to λ would require a corresponding decrease to η_o to remain on the same contour line.

Future Work

At this point, it is unclear if using this model for simulating HEC fluid is optimal. Improvement similar to the ones suggested for the power-law model, with the exception of the one proposing to change the constitutive equation, would also undoubtedly improve this models agreement with experiment. Nevertheless, because this model did not improve its agreement with experiment over the power-law model, I would not recommend perusing it further for simulating HEC fluids within 2.4-3.0% concentration. Nevertheless, if a potential fluid did have a strong dependence on the low-shear rate viscosity, in order to properly use the parameter analysis in this study, it is important to first find the relationship between solute concentrations and rheological parameters. For a microbicide application, such as the one presented in this document, the solute would clearly be HEC and its concentration could change after application.

Conclusions

In this chapter, I presented a novel numerical simulation of a finite bolus of Ellis fluid spreading down an incline. The numerical simulation shows convergence to a single solution, as the spatial mesh is made finer. Also, the numerical solution shows good agreement with a similarity solution that was confirmed to satisfy the Ellis evolution equation. This satisfied the engineering goal of the first sub-objective and the second overall objective of this work. As far as I know, this is the first derivation and numerical solution governing the free surface of an Ellis fluid spreading due to gravity.

Comparing the Ellis and power-law numerical models with the experiment, I address the hypothesis of Sub-Objective 4.2 by concluding that accounting for the low-shear rate viscosity, for the HEC gels considered in this study, does not improve agreement between theory and experiment. Consequently, *I would not recommend using the Ellis model for the simulation of HEC fluids being considered in this study.*

Finally, to satisfy Sub-Objective 4.3, I conduct an Ellis parameter study to determine the influence each parameter on spreading and spreading rate. This analysis can be applicable to any field of study interested in the spreading of fluids that are well represented using the Ellis constitutive equation. This might include other candidates for microbicidal gels that were not considered in this study, such as methylcellulose gels or HEC gels at higher concentration.

Chapter 7 Discussion and Application

The overall objective of this work was to develop a microbicide delivery vehicle that is capable of acting as a reliable pharmaceutical delivery medium and barrier to the vaginal epithelium. Our research group believes that a reliable numerical model that simulates the spreading of a potential vehicle can be used to predict the efficacy of a specific fluid and a tool for conducting efficient and cost effective sensitivity analysis of the fluid's rheological parameters, in order to optimize the fluid's spreading and coating characteristics. In addition, a bench top experimental apparatus and software that is capable of providing spreading characteristics in a domain that closely resembles *in vivo* conditions can be used as a validation for the numerical model and as another tool for predicting a fluid's spreading behavior after application.

To arrive at a "Master Model" of the fluid spreading in a virtual environment of a female's lower reproductive track, a complete numerical simulation must account for gravity, shearing and squeezing perturbation forces. In addition, because a potential vehicle will likely be a cellulose-based polymeric fluid, a crucial aspect of a reliable model would be to capture the vehicle's rheological properties, which would dictate the fluid's behavior resulting from internal stresses. Also, as I will discuss in more detail in the "Future Work" section, while accounting for each perturbation force it is important to consider the interaction between the fluid-solid interfaces. Simply implementing the no-slip boundary condition might be acceptable for models compared with flow experiments conducted on Plexiglas surfaces, but would oversimplify the gel spreading on biological epithelial tissue, which is coated in other ambient fluids. This

ambient fluid could not only change the gels composition, but might drastically undermine the no-slip boundary condition.

General Conclusions

The work presented in this document was restricted to free surface flows of non-Newtonian fluids. To satisfy the first overall objective of this work, and the first objective of this dissertation, in Chapter 3 I presented an apparatus, image analysis software and procedure for conducting environmentally controlled spreading experiments, and obtaining the fluid's spreading characteristics and surface topography. To satisfy the second overall objective of this work, in Chapters 4, 5, and 6 I presented numerical models simulating the free surface, gravity-induced flow of Newtonian and non-Newtonian fluids using different constitutive equations, and compared the results with experiments.

Hypothesis: 3-D model will improve agreement with experiment over 2-D model - Confirmed

The power-law and Ellis models were reasonably effective for predicting the axial spreading of HEC gels, especially when using 3-D modeling. In fact, *2-D numerical modeling noticeably overestimated axial spreading, when compared with experiment, and the 3-D model greatly improved that overestimation*.

Both the power-law and Ellis models were somewhat unsuccessful at modeling lateral spreading. Experimental data showed that gels would typically slump in the lateral direction for approximately the first 30 sec of spreading and then maintain a somewhat constant width for the remainder of the experiment. The computational simulations, regardless of the constitutive equation, showed that typically lateral spreading was approaching a plateau after 60 seconds.

Therefore, during the 90 second simulation, the computational spreading characteristics would overestimate the experiment by approximately 5*mm*.

<u>Hypothesis:</u> Incorporating local surface gradients into the numerical initial condition will result in better agreement with experiment, when compared with an initial condition that only includes bulk dimensions - Confirmed

Using the power-law numerical model, I tested if accounting for local surface gradients on the free surface of the initial condition would improve the numerical model's estimation of experiential spreading at later times. Surprisingly, using a numerical initial condition that matched the free surface of the experiment did not improve agreement between model and experiment, when compared with an initial condition that was a 4^{th} order approximation (Eq. (5.38)) of the experiment's topography (matching only the maximum height, length and width). In fact, using an approximate initial condition slightly improved agreement with experiment. Nevertheless, because the 3-D power-law model slightly overestimates axial spreading, using an approximate initial condition caused this overestimation to be inhibited because of a "waiting time" solution [52]. It took time for the center of gravity to advance to the leading edge and move the contact line; therefore the overall movement of the contact line was delayed when compared with a computation that used a real initial condition. Therefore, *I conclude that incorporating an accurate topography of the experimental initial condition is a critical model consideration, when comparing model with experiment.* Because the evolution of the free surface is mostly governed by the derivatives of the height variable, the values of this variable being input into the initial condition must be consistent with the experiment, with which the numerical model is being compared to.

<u>Hypothesis:</u> Accounting for the low-shear rate Newtonian viscosity by using the Ellis constitutive equation would improve agreement with experiment over the power-law constitutive equation – Inconclusive and conditional

Both models approximated the experimental axial spreading within 1 *cm* for the entire 90 *sec* simulation. For *both the power-law and Ellis models, the initial spreading velocity of the fluid was noticeably greater than experiment, although the Ellis model did show a slight improvement over the power-law when using a T3 technique for obtaining rheological parameters.*

A serious limitation of the Ellis model is the fact that there are several ways of fitting to the rheological data, and each technique results in different values of the Ellis parameters leading to different model behavior. In addition, the fact that the Ellis model did not provide considerable improvements of the power-law model allows me to conclude that *the low-shear rate Newtonian viscosity is not a driving parameter for the gels considered in this document*. Therefore, I would not recommend using the Ellis model to simulate the gels being considered in this study, but it might be necessary for a gel with a larger low-shear rate Newtonian plateau. An important implication of this conclusion is that for 2.4-3.0% HEC gels, η_0 is not critical and can be left out of the parameter analysis.

Application

Only conducting gravity-induced analysis is obviously oversimplifying the true nature of the problem. Therefore, even sensitivity analysis of the numerical models presented in this document are useful for getting an idea of how specific rheological parameters influence spreading characteristics, but cannot be directly extrapolated to a vaginal drug delivery

application. Nevertheless, before assembling a complete "Master Model", it is useful to isolate a single perturbation variable, as is being done in this document. This type of study can clearly allude to the validity of the constitutive equation because the nature of this type of flow is easier to model experimentally, and allows for direct comparisons between theory and experiment.

To give an idea of how a parameter analysis could be used, I present a practical example of using the presented data for optimizing a potential delivery vehicle, when considering only free surface flow. This can be combined with models that account for other perturbation forces to get a more accurate relationship between gel physiochemical property values and coating characteristics. In this discussion, the example is only intended as proof of concept. Here I show how to identify sample target values for n and m depending on some general anatomical parameters, desired spreading time, and inclination angle. Assuming that the gel only needed to cover approximately 3 *cm* in 90 sec, at $\alpha = 30°$, a gel with an n = 0.3-0.6 and m = 350-600 Ps^{n-1} would be the target rheological values (from Fig. 5.9). If in a patient specific scenario, the target distance is increased to 5 *cm*, a gel with an n = 0.8-1 and $m \sim 200$ Ps^{n-1} would be the target rheological values. Parameter analysis to accommodate larger domains would need to be computed for longer times, or at steeper inclination angles, or both. As discussed in Chapter 5, specific ways of looking at non-dimensional data, as presented in Figure 5.11, can be used to approximate how changes to inclination angle or spreading time would influence a gel with specific physiochemical properties. Moreover, the numerical code presented in this document, combined with other models accounting for different perturbation forces, can be used to conduct a full mapping of vaginal coverage length, inclination angle, and tissue elastic properties and their target rheological parameter values.

The zero-shear rate parameter, η_0, included into the Ellis model will increase axial spreading as its value is decreased. Nevertheless, this work does not find η_0 to be a critical parameter for the HEC concentration range considered. It is possible that this parameter must be considered for different concentrations of HEC or other solutes.

Part of the reason for why it is important to conduct detailed percent sensitivity analyses is because once the fluid is introduced to a vaginal environment; its rheological characteristics could change due to dilution resulting from high humidity and surrounding fluid, and temperature changes. If only considering gravity, the analysis in Chapters 5 and 6 can give a framework of how small changes to the fluid's composition might impact spreading characteristics. In future work, a parallel study is necessary to document how changes to a solute's concentration will influence changes to *n* and *m*. The sensitivity analysis conducted in Chapter 5 showed that if dilution caused a 10% increase to *n* and decrease to *m*, axial spreading can change by up to 8.2%, on a 30° incline. If a gels chemical composition change was to impact a single power-law parameter, the influence on axial spreading would be reduced. Also, the impact of delusion is dependent on the original concentration of the gel. Axial spreading is most drastically changed for power-law fluids with original *m* and *n* values of 400 Ps^{n-1} and 0.6, respectively. Changes to axial spreading for gels starting with other original power-law values were between 6.8% and 8.0%, within the ranges of *m* and *n* presented in Chapter 5. Future work should focus on changes to axial spreading for fluids within a larger range of original power-law values and at different inclination angles.

Suggested Improvements to the Numerical Model

It might appear as if the overestimation of spreading in the lateral direction, and spreading rate in the axial direction at the onset of spreading, is a direct result of the fact that surface tension was neglected. Therefore, it is possible that accounting for increased tension at the free surface would limit spreading in the lateral direction and possibly decrease the initial outburst at the start of the simulation. While this is a valid hypothesis, which should be investigated in future work, it's important to avoid devoting time and effort to a strategy that might not result in drastic or even noticeable improvements. In fact, the Bond number (ratio of gravity forces to surface tension) for a typical flow discussed in this dissertation is much greater than 1 (typical values for this dissertation are 38-220), which would suggest that the original decision to neglect surface tension is reinforced. On the other hand, in the side view profile of the experiments and topographical measurements (Figure 3.9) we see that the fluid develops a capillary ridge, which would imply that the effect of surface tension might not be negligible after all.

One might point out that correcting the 3-D model to predict less slumping in the lateral direction would effectively cause more mass to propagate in the axial direction, causing yet another inconsistency with experiment. This is not necessarily true because: (1) the decrease in maximum height of the numerical model overestimates the experiment by approximately 2-3 *mm* suggesting that improving the overestimated lateral spreading could also improve agreement in terms of maximum height, and (2) the shape of the cross-section of the fluid along the lateral plane could be noticeably different after improving lateral overestimation.

Discussion of surface tension

Bin Hu (University of Kansas, Mechanical Engineering) has been investigating the impact of surface tension on microbicidal gels. He found that it can result in instabilities at the moving contact line ("fingering") and that surface tension can directly impact spreading characteristics. Incorporating surface tension into future numerical models is possible, but first analysis of the flow vectors might give insight into whether this update would improve the models agreement with experiment.

Gratton *et al.* [74] introduced a method for incorporating surface tension effects into the evolution equation. Making the following replacements to the flux terms (Eq. (7.1 & 7.2)):

$$\frac{\partial h}{\partial x} \rightarrow \frac{\partial h}{\partial x} - \left(\frac{\gamma}{\rho g \cos \alpha} \right) \frac{\partial}{\partial x} \left(\frac{\partial^2 h}{\partial x^2} + \frac{\partial^2 h}{\partial y^2} \right) \tag{7.1}$$

$$\frac{\partial h}{\partial y} \rightarrow \frac{\partial h}{\partial y} - \left(\frac{\gamma}{\rho g \cos \alpha} \right) \frac{\partial}{\partial y} \left(\frac{\partial^2 h}{\partial x^2} + \frac{\partial^2 h}{\partial y^2} \right) \tag{7.2}$$

where γ is the surface tension (units), results in a modified evolution equation that incorporated surface tension as a driving factor. Figure 7.1 shows the flow rate per unit width vectors for a free surface, with and without surface tension. These plots were made by incorporating Eq. (7.1) and (7.2) into the power-law flux terms and evaluating them for a generic topography (Figure 7.1a). The model that does not incorporate surface tension seems to have a very dominating axial flow along its center, and then starts to diffuse outward at the edges. In addition, the flow at the trailing edge seems to be going in the opposite direction from the flow at the leading edge. It makes sense that this would happen at the initial stages of spreading, and it is seen in the experiments also. For the model that solves for surface tension, there also seems to be

dominating axial flow along the center, but it gets shorter at the leading edge than it is within the bulk of the fluid.

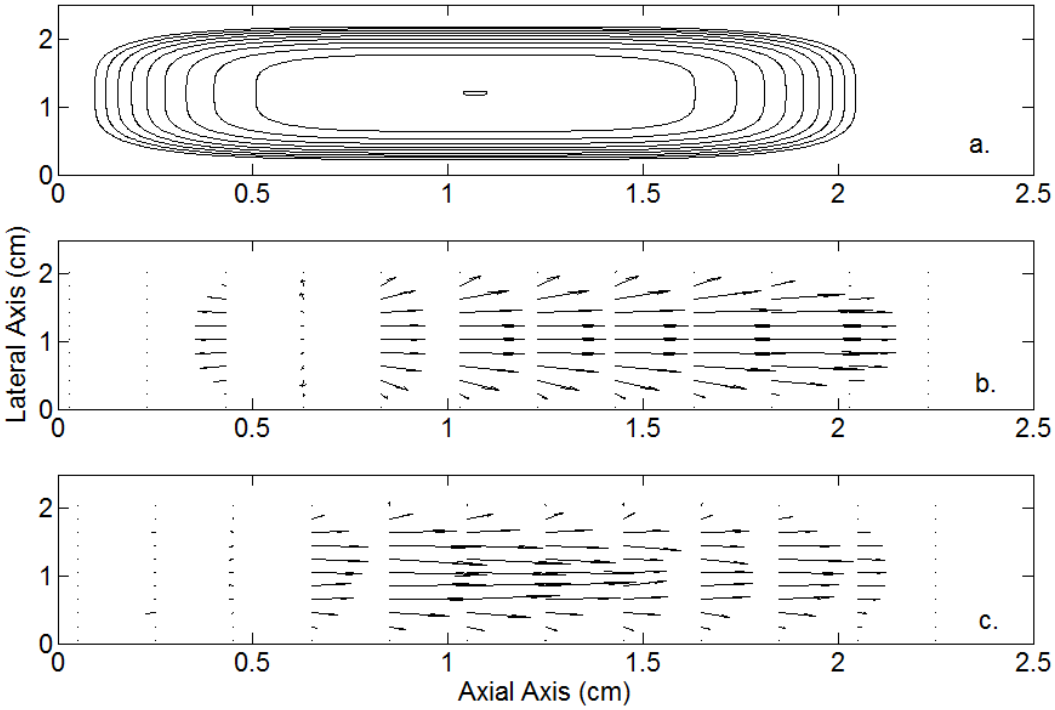

Figure 7.1. Comparison of flow rate per unit width for a simulation with and without surface tension. (a) Contours of free surface (b) flow rate per unit width vectors without surface tension (c) flow rate per unit width vectors with surface tension: $\gamma = 40$ (units).

Visco-elastic representation of the fluid

I hypothesize that a more likely culprit for most inconsistencies between the model and experiments is the constitutive equation. I suspect that only accounting for the gels pseudoplastic behavior is insufficient. Therefore, I would suggest exploring other constitutive relationships that account for the fluid's elastic component, and factors such as relaxation. This is by no means a trivial task, and it could result in a considerable burden on computation, even if an evolution equation can be explicitly written.

Constitutive models that account for a fluid's viscoelastic behavior could be an important improvement on the current numerical simulations. An example of such a model is the Maxwell

constitutive equation. This can account for the relaxing internal stress in response to strain, and the constant internal stresses resulting from elongation.

$$\tilde{\tilde{\tau}} + \lambda \frac{\partial \tilde{\tilde{\tau}}}{\partial t} = \eta_0 \left(2\tilde{\tilde{D}} \right) \qquad (7.1) \ [88]$$

Where, λ is the relaxation time in sec, and η_0 is a function which accounts for the viscous and elastic components of a Maxwell element. Eq. (7.1) is a first order ODE, and incorporating it into the evolution equation is more difficult than the power-law and Ellis equations.

Incorporating a yield stress

Most of the discussion, the entire derivation, and numerical solution in this section was originally presented by Kieweg [3]. In this document, I reintroduce some of the issues that I consider relevant and show some original data of parameter analysis of a Herschel-Bulkley model.

Even though the current placebo is a shear-thinning fluid with some elastic properties, a reasonable assumption for future microbicide candidates is that the delivery vehicle will contain some sort of yield. After coating the inner lumen, some type of internal stress would be necessary to retain the gel under the continued influence of gravity, squeezing and shear forces.

An in-depth literature background on mathematical modeling of fluids that exhibit a yield stress is presented in Chapter 4. The goal of this discussion is to introduce how a yield stress would be incorporated into the master model, while still considering shear-thinning behavior.

A fluid which exhibits both shear-thinning and yield stress behavior can be modeled by a Herschel-Bulkley constitutive equation [65]:

$$\tau_{xz} = \tau_o + m\left|\frac{\partial u}{\partial z}\right|^{n-1}\frac{\partial u}{\partial z} \qquad \text{for } \tau_{xz} > \tau_o \tag{7.4}$$

$$\frac{\partial u}{\partial z} = 0 \qquad \text{for } \tau_{xz} \le \tau_o \tag{7.5}$$

Eq. (7.4) and (7.5) are written in 2-D according to the coordinate system defined in the power-law section in Chapter 5, where, τ_o is the yield stress and all other terms are consistent with the power-law model. The velocity gradient is zero in the fluid region between the yield surface, $z = h_0(x,t)$, and the free surface, $z = h\ (x,t)$. The shear stress at the yield surface is $\tau_0 = \tau_{zx}\big|_{z=h_0}$. This yields an expression for the yield surface:

$$h_0(x,t) = h(x,t) - \frac{\tau_0}{\left|\rho g\left(\sin\alpha - \cos\alpha\frac{\partial h}{\partial x}\right)\right|} \tag{7.6}$$

Using the same procedure as for the power-law formulation, we arrive at the following evolution equation for a Herschel-Bulkley fluid:

$$\frac{\partial h}{\partial t} + \left(\frac{\rho g}{m}\right)^{1/n}\left(\frac{n}{1+2n}\right)\left(\frac{1}{1+n}\right)\frac{\partial}{\partial x}[S] = 0 \tag{7.7}$$

where,

$$S = |B|^{\frac{1}{n}-1}(B)\left[h - \frac{\tau_o}{\rho g B}\right]^{\frac{1}{n}+1}\left[(1+n)h + \frac{(n)\tau_o}{\rho g B}\right] \tag{7.8}$$

and

$$B = \sin\alpha - \cos\alpha\frac{\partial h}{\partial x} \tag{7.9}$$

The evolution equation (Eq. (7.7)) has the following constraint [66, 69] for flow to occur:

$$h_o(x,t) = h(x,t) - \frac{\tau_o}{\rho g|B|} > 0 \tag{7.10}$$

This also requires that B is greater than zero. The cross-section of a spreading bolus of a Herschel-Bulkley fluid has two regions: (i) the yielding region – where the stress within the material has exceeded the fluid's yield stress and is flowing ($\partial u/\partial z \neq 0$), and (ii) a region that is approximated as pseudo-plug flow ($\partial u/\partial z \approx 0$). In Eq. (7.10), h_o physically represents the height of the yield surface, meaning that only the fluid below h_o is undergoing shear.

Similar Herschel-Bulkley evolution equations for 1-D or 2-D spreading on relatively steep slopes were solved using self-similar solutions [91], numerical methods [92], and asymptotic solutions [67, 72]. Kieweg *et al.* [3] has developed a 2-D numerical simulation of a Hershel-Bulkley fluid spreading down an incline. Numerically, The flow constraint (Eq. (7.10)) was imposed onto the flux term in the evolution equation using a numerical step function, Λ:

$$q = \left(\frac{\rho g}{m}\right)^{1/n}\left(\frac{n}{1+2n}\right)\left(\frac{1}{1+n}\right)\frac{\partial}{\partial x}[S]\cdot\Lambda\left(h(x,t) - \frac{\tau_o}{\rho g(B)}\right) \tag{7.11}$$

where, $\Lambda(x) = 1/2 + (1/2)\tanh(x/\delta)$ is a numerical Heaviside function and δ specifies the transition range (set to $\delta = 10^{-6}$). This function is similar to the one used by Balmforth *et al.* [28] to dictate if the flux at a given point is greater than zero.

Figure 7.2 shows example numerical results for the spreading of a Herschel-Bulkley fluid. As in the power-law results, the gradient of the free surface between the nose and the front must reach a critical value before the contact line begins to move. This is clearly presented in Figure 7.2 by the fact that L_{front} does not start moving for approximately the first 2 sec, while L_{nose} moves closer to the contact line.

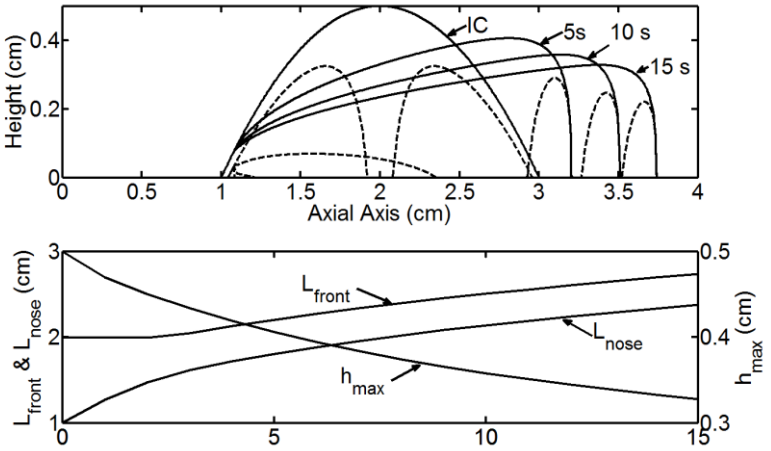

Figure 7.2. Numerical results of the evolution of the free surface of a Herschel-Bulkley fluid. (TOP) The evolution of the free surface (solid) and the yield surface (dashed) at *t = 0, 5, 10* and *15* sec. (BOTTOM) Axial spreading of the nose and front, and height vs time. Input Parameters:$\alpha = \pi/6,\ \tau_0 = 39.2\ dynes/cm^2, m = 500\ Ps^{n-1}, n = 0.8$

Sensitivity analysis of the Hershel-Bulkley numerical model showed that yield stress had a large influence on spreading characteristics, as expected. Figure 7.2 shows the non-dimensional spreading length as a function of a non-dimensional reference thickness (Eq. (7.12)). The h_c' is a ratio of yield stress to gravity terms, and thus a measure of plasticity.

$$h_c' = \frac{\tau_o}{\rho g}\frac{1}{H} \tag{7.12}$$

Where, H is the characteristic height of the bolus and t' represents the non-dimensional ratio of gravity to viscous terms at a given time.

$$t' = \frac{t}{\left(\dfrac{m}{\rho g H \sin\alpha}\right)^{1/n}} \tag{7.13}$$

In all cases, increasing the plasticity will result in a decrease of the spreading distance. Additionally, the spreading length is more sensitive to plasticity as the consistency index is decreased.

For a constant yield stress, varying the power-law parameters had the same effect for the Herschel-Bulkley fluid as for the power-law fluid: as the shear-thinning index increased or the consistency index decreased, the fluid spread further. Huang and Garcia's analysis [72] with asymptotic solutions included the influence of shear-thinning on viscoplastic mud flow, evaluated at two yield stress values. For both of the yield conditions, it was found that a Bingham fluid ($n = 1$) spread more than the shear-thinning fluid ($n = 0.6$). Our results match those, and expand for variations in m and inclination angle. Specifically, with our numerical model we can further examine the effect of the ratio of gravity to viscous terms, over a range of yield stresses.

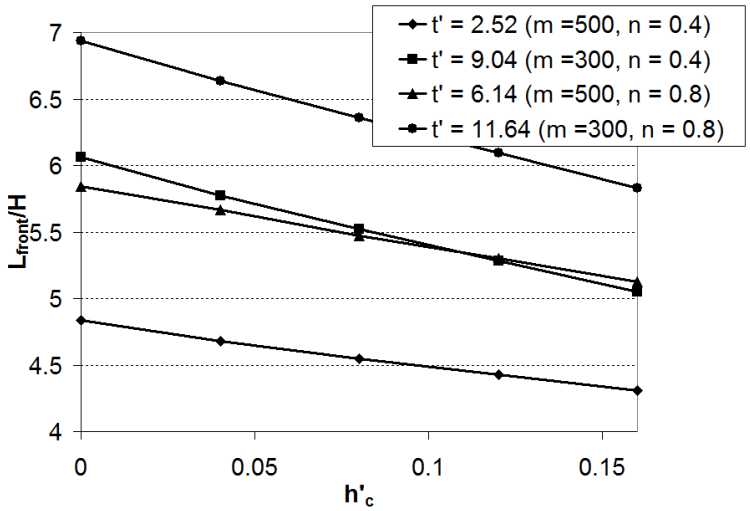

Figure 7.3. Numerical results of a Hershel-Bulkley fluid and sensitivity analysis showing the effects of m, n and τ_o on spreading. Input Parameters: $t_{final} = 15$ *sec*, $\alpha = \pi/6$, $H = 0.5$ *cm*. (Extension of data presented in [3], but computed for different rheological values and angle of inclination, α) Note: $L_{front}/H \equiv$ ratio of axial spreading to characteristic height; $m \equiv$ consistency index [=] Ps^{n-1}; $n \equiv$ shear-thinning index; $h_c' \equiv$ ratio of yield stress to gravity terms; $t' \equiv$ ratio of gravity to viscous terms.

As Figure 7.3 indicates, the h_c' value was a predictor of spreading distance. However, the ranking of the ratio of gravity to viscous terms (the non-dimensional time term) was not a

predictor of spreading distance, and the ranking was dependent on plasticity. Our sensitivity study showed an effect of pseudo-plasticity on the impact of yield stress. Figure 7.3 shows that, for this time frame, the effect of changing yield stress (i.e. the slope of the line) is the same for both $n = 0.4$ and $n = 0.8$ when considering a fixed m value. These observations may be limited to the short time frame, and this particular inclination angle.

Figure 7.4 presents the spreading results as a function of the non-dimensional time (Eq. (7.13)), as was done for the power-law solution. The top and bottom edges of the parallelogram region in Figure 7.4 indicate iso-lines for constant n. As the arrow indicates in the figure, the constant n lines shift down as the yield stress increases. The slope of the line (and thus the spreading of the fluid) depends on the yield stress, but not the level of shear-thinning.

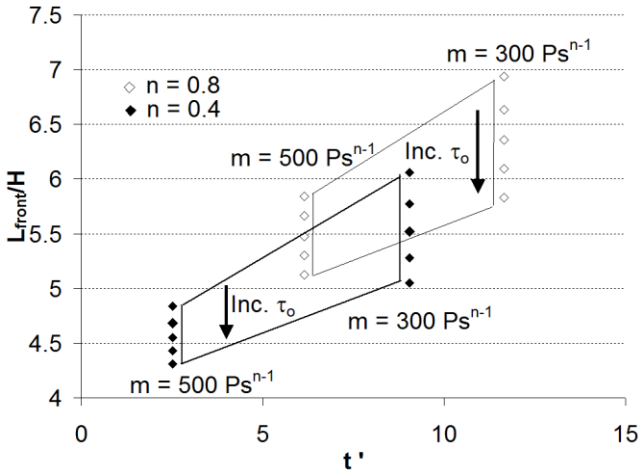

Figure 7.4. Herschel-Bulkley numerical results as a function of non-dimensional time. Input Parameters:, $t_{final} = 15$ *sec*, $\alpha = \pi/6$, $H = 0.5$ *cm*. Note: $m[=]Ps^{n-1}$ (Plot obtained from [3]). Note: $L_{front}/H \equiv$ ratio of axial spreading to characteristic height; $m \equiv$ consistency index [=] Ps^{n-1}; $n \equiv$ shear-thinning index; $t' \equiv$ ratio of gravity to viscous terms; $\tau_0 \equiv$ yield stress [=] dynes/cm^2.

As another demonstration of the trade-offs between yield stress, viscous resistance, and gravity, Figure 7.5 indicates that as the yield stress increases, the ratio of gravity to viscous terms (the non-dimensional time) required for the fluid to start flowing increases.

In conclusion, this work shows that future implementation of yield stress into the 3-D numerical analysis is feasible. Moreover, the sensitivity analysis gives a better understanding of the yield stresses impact of spreading, and what we might expect from incorporating it.

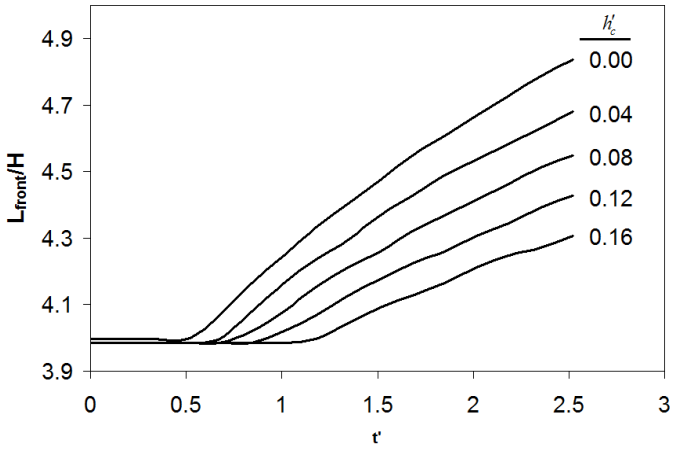

Figure 7.5. Numerical results of a Hershel-Bulkley fluid and sensitivity analysis showing the effects of *m*, *n* and τ_o on spreading. Axial spreading is decreased at higher values of yield stress. Input Parameters: $t_{final} = 15s$, $\alpha = \pi/6$, $H = 0.5cm$, $m = 500\,P\,s^{n-1}$, $n = 0.4$. Note: $L_{front}/H \equiv$ ratio of axial spreading to characteristic height; *t'* is a ratio of gravity to viscous terms; $h_c' \equiv$ ratio of yield stress to gravity terms.

Future Work

Incorporating shearing and squeezing into the evolution equation

Sunil Karri (University of Kansas, Mechanical Engineering) is currently working on a numerical model that simulates the squeezing perturbation force of the anterior and posterior epithelium. It is perhaps the most influential perturbation force and must be considered in any type of master model.

Once a constitutive equation is finalized, by perfecting the free surface model, the simulation can be upgraded to incorporate both gravity and squeezing perturbation forces. A scenario modeled by Yin and Kumar [93] includes the elastohydrodynamic interactions that arise

from flow between flexible walls. Figure 7.6 shows a scenario of a fluid entrapped between a flexible wall and a rigid surface. The pressure exerted on the gel by the posterior epithelium is mathematically incorporated in Eq. (7.14) through the free surface pressure term.

$$p(x) = E_{p\varepsilon} D(x) \delta^{-1} \qquad (7.14)$$

A project at the KU Biofluids laboratory is currently underway to determine a typical modulus of elasticity for the vaginal epithelium, to be used as input into the 2-D numerical power-law model.

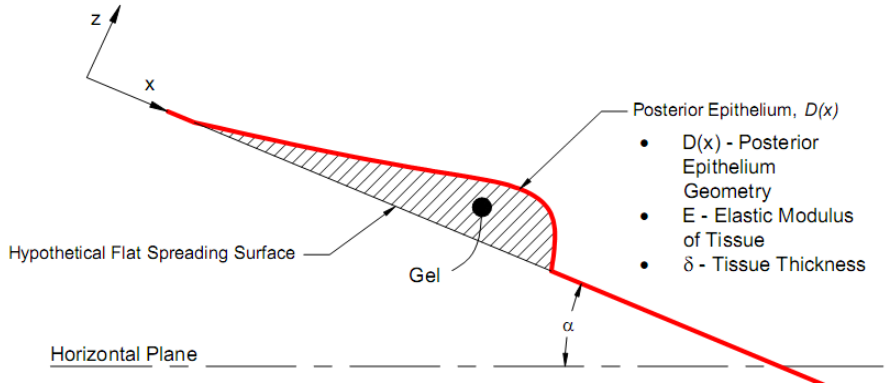

Figure 7.6 Squeezing spreading scenario.

Accounting for fluid-solid contact interaction

As the fluid is introduced to the vaginal lumen, and is free to spread, one factor that must be considered is the fact that the spreading surface could considerably alter spreading characteristics. Preliminary experimental analysis has shown that conducting gravity-induced, free surface spreading experiments on a glass surface will result in considerably inconsistent spreading profiles of the same fluid, when compared to spreading on a plexiglass surface. Future work will require repeating these experiments on a bovine epithelium surface and ultimately accounting for the thin substrate of mucus that would separate the gel from the epithelial spreading surface. Mathematical analysis of this problem would be very complicated, but simply

incorporating a slip length could roughly model this phenomenon. An important direction for this research is to investigate ways to relax the no-slip boundary condition, which is the focus of the following discussion.

Contact Angle – A contact angle θ is the angle that a drop of fluid makes when in contact with another surface (Figure 7.7). For simplicity I will consider this drop to be some liquid in contact with a solid, all within some gas.

The forces of the surface molecules, within a unit area, of the liquid will depend on the medium with which the unit area is in contact with. The surface of the liquid in contact with the solid will undergo a tensile contraction of different magnitude than the surface of the liquid in contact with the surrounding gas.

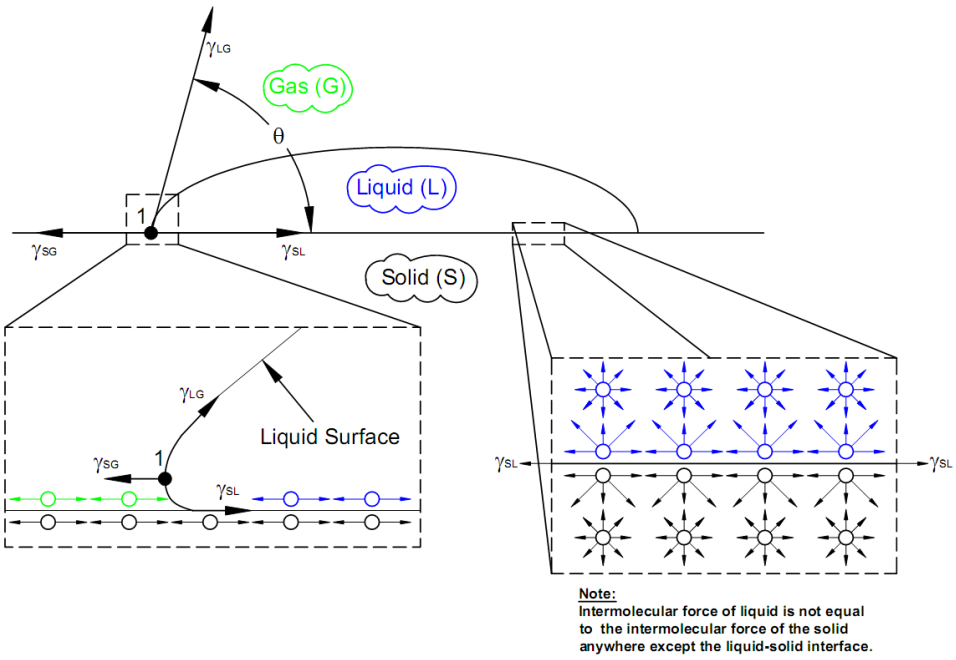

Figure 7.7 Graphical Representation of Contact Angle

Figure 7.7 shows a liquid drop resting on a solid, all immersed in some gas with all three mediums in equilibrium. Assume point 1 is a molecule on the edge of the liquid drop. Note that

the interface forces γ_{LG}, γ_{SL} and γ_{SG} will be the magnitude of the 3 different forces acting on point 1 (Figure 7.7). With that considered, in order for point 1 to be static all the forces should cancel out. As can be seen from Figure 7.7, all the forces will cancel out (be in equilibrium) when the drop adopts a specific shape, characterized by the contact angle, θ, which represents a force balance between the molecular forces at the gas-fluid-solid interface:

$$\sum F_x = 0 \Rightarrow \gamma_{LG} \cos\theta = \gamma_{SG} - \gamma_{SL} \tag{7.15}$$

Young equation can be used to describe the "wetting" of a liquid on a specific solid by using the contact angle.

cos θ = 1 $\Rightarrow$ Drop spreads completely over entire solid surface (complete wetting)

-1 < cos θ < 1 $\Rightarrow$ Drop partially spreads over the solid surface (partial wetting)

cos θ = -1 $\Rightarrow$ The drop is curled up into a sphere and is making minimal contact with the solid (Un-wetted)

Slip Length – When a fluid is propagating along a solid, it is normally assumed that the fluid at the fluid-solid interface is not moving. This corresponds to a no-slip boundary condition (Figure 7.8 a), which most researchers tend to implement for macro-scale flows (fluid thickness > 20 molecular diameters) [94]. Nevertheless, depending on the wetting properties of the fluid/solid interface, some fluids will tend to slip during propagation (Figure 7.8 b). This "slip" velocity is proportional to the distance that the velocity profile would project into the solid before the front of the profile would intersect with the back, b (Figure 7.9).

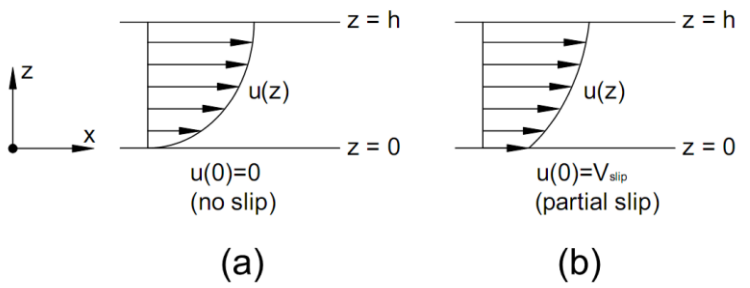

Figure 7.8 Velocity Profiles for no-slip (a) and partial-slip (b) Boundary Conditions

For a partial slip scenario, the slip velocity in the axial direction of spreading, u_s, is quantified using Eq. (7.16).

$$u_s = b\frac{\partial u}{\partial z} \tag{7.16}$$

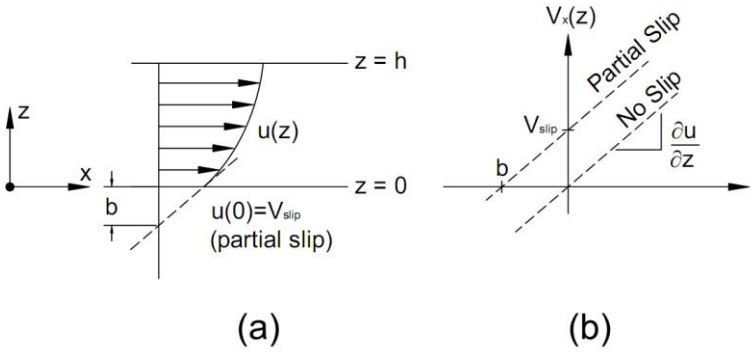

Figure 7.9 Derivation and Graphical Representation of Slip Length

Relating Contact Angle to Slip Length – It should be noted that the very act of measuring the contact angle is theoretical. The angle will vary with resolution and most importantly the zoom with which it is observed. The more a drop corner is zoomed in on the larger the angle will appear.

Many researchers have tried to relate some kind of contact angle measurement to slip length because of the intuitive relation they must have with one another. It should be noted that

because of the sensitivity of both of these parameters, any kind of modeling showing the relationship between slip length and contact angle undergoes warranted criticism because of the unrealistic assumption it makes that: the surface of interface is completely flat with no grooves. Obviously this is inapplicable to the physical world and especially to any macro-scale observation. The real problem is the fact that this assumption provides erroneous results when finding the contact angle because surface roughness might contribute to how much the drop spreads. Combined with the limitations of the contact angle, the slip length relation would produce a colossal error. Consequently, modeling the slip length by measuring the contact angle is probably not a reliable option for improving the current numerical model.

While these methods cannot be applied to the physical world, their findings are still very important because they show a relation between wettability and slip length. They prove that they are not independent of each other and that at very low wettability, the no-slip assumption should be re-considered, maybe even for macro-scale analysis.

Determining Slip Length without Using Contact Angle - While the methods presented in this section also fall victim to the no-groove surface assumption, the resulting error of this assumption is cut in half because it is no longer considered for the drop when measuring contact angle.

In a paper by J. Baudry and E. Charlaix [95], it was shown that the no-slip boundary condition might not be valid when considering fluid flow in contact with hydrophobic surfaces, even for a macro-scale. Using a surface force apparatus, they observed the hydrodynamic force between a solid sphere and a plane immersed in glycerol (Figure 7.10). When the sphere was oscillated at a specific frequency and amplitude, the immersed glycerol provided a damping to the oscillation. Analysis with a no-slip boundary condition showed a relation of the damping

with the distance of separation D. Assuming that D and b were related, combined with the assumption that $b << D$ showed that the slip length b was equal to the distance of separation D when the relation: $6\pi R^2 \eta / A = 0$, where all the values in the relation are physically measurable: A = damping coefficient, R is the radius of the sphere and η is the viscosity of the fluid, which is averaged for a non-Newtonian fluid (within the relevant shear region). They also verified their results by showing that a situation in which the no-slip boundary condition was expected, a value of $b = 0$ was obtained.

This analysis might be directly applicable to this research because it is an opportunity to determine the slip length without having to measure any kind of contact angle, the limitations of which are described above. We could even perform this analysis on an already available rheometer (AR 2000), because it is capable of checking the damping resulting from oscillating a fluid and the distance of separation between two surfaces.

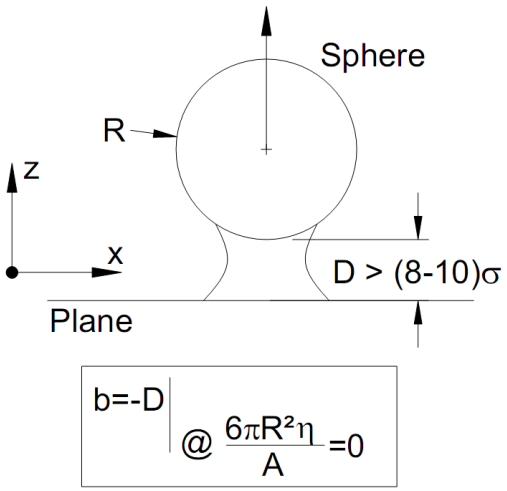

Figure 7.10 Relation of Slip Length to Distance of Separation

Mucus-Gel Interaction: When considering the application of micribicide research, we need to not only be able to use boundary conditions for gel-solid interaction, but also for gel-body fluid interaction. In order to model this interaction correctly, a crucial step is to determine how the gel intermingles with any kind of fluids it might come into contact with in the vaginal lumen. If it is found that the gel completely mixes with a fluid, rheological properties will be gathered of the gel-vaginal fluid mixture, and standard rheological analysis of that mixture will be performed with the gel in contact with the solid epithelium. If we are to determine that the gel is immiscible with any form of the vaginal fluid, and then gel-vaginal fluid surface properties will be determined using the methods described above and analysis will be carried out as two immiscible fluids in contact with each other.

An immiscibility assumption can be justified by determining the inner interaction potentials, *W*, of each fluid. Israelachvili [96] suggests that if the interaction potentials of each fluid are very different from each other, than the fluids can be considered immiscible.

The methods for determining *W* for each fluid will not be discussed because it is purely theoretical, and as will be described below more practical approaches can be employed.

In practice, the methods used to determine if a gel will mix with the fluid it interacts with will be employed using techniques similar to the ones described by Anthony R. Geonnotti *et al* (2005) [97]. This work describes an approach of putting gels in contact with vaginal fluid (and semen) for specific periods of time and measuring the change in viscosities of both layers as a function of time, and then using that to qualify the miscibility of the two fluids.

Experiments with Epithelium Tissue Spreading Surface

Having a bench top experimental apparatus that is capable of controlling temperature and humidity, along with a software that will provide spreading characteristics and topography as a function of time, allows us to expand the experimental work that has been completed by conducting spreading tests on bovine epithelial tissue. The instrument is designed in such a way, that a cut of tissue could easily be incorporated into the spreading surface.

These types of test will truly allow us to assess the impact of fluid-structure interaction in the *in vivo* domain. Overall they would be valuable to conclude if the "no slip" boundary condition is suitable for spreading on biological tissue.

Final Conclusions and Remarks

Aside from a microbicide application, the novel work presented in this dissertation presents: (1) an instrument and technique for conducting gravity-induced flow experiments, (2) a numerical solution of the power-law evolution equation, (3) a sensitivity analysis of the power-law rheological parameters, (4) a derivation of the Ellis evolution equation, and (5) a numerical solution of the Ellis evolution equation along with an original parameter study and sensitivity analysis.

This work is a foundation for the final "master model." Once all the other perturbation forces are included, a working numerical simulation will be useful for parameter studies, sensitivity analyses and a tool for reverse engineering rheological parameters that will be necessary for the fluid to serve a specific function. Consequently, it is important to conduct parallel work to determine relationships between cellulose concentration and rheological parameters.

Final *in vivo* analysis will reveal the efficacy of the numerical model by validating it with an experimental model. This will result in collaboration with pharmaceutical developers to complete an affective microbicidal gel that could have enormous impact on the millions of people affected by HIV.

Appendix A- The Lubrication Approximation

The proof for the lubrication approximation is written for a free-surface, 2D flow, scenario in which the direction of axial spreading is in the *x*-direction, and the decrease in the height of the free surface is along the (-*z*). I define the velocity vector as: $\tilde{u} = u\hat{i} + w\hat{k}$.

In the equation of motion, for a steady flow (Eq. (A.1)), the terms on the left side can be neglected under the assumption of several properties of the flow.

$$\partial\tilde{u}/\partial t + (\tilde{u}\cdot\nabla)\tilde{u} = -(1/\rho)\nabla\tilde{p} + (\mu/\rho)\nabla^2\tilde{u} + \tilde{g} \qquad \text{(A.1)}$$

A straightforward way of neglecting the inertial terms is to recognize that if the Reynolds number is very small (Eq. (A.2)), the viscous terms must dominate with respect to the inertial terms. Therefore, the inertial terms $(\tilde{u}\cdot\nabla)\tilde{u}$ are assumed to be zero.

$$\left(\frac{\rho UL}{\mu}\right) << 1 \qquad \text{(A.2)}$$

This is an effective strategy for simplifying the momentum equation to set the left side equal to zero, but only for a steady flow. Nevertheless, for a flow that is very viscous, but is not necessarily steady, another strategy can be used to show that the terms on the left side of Eq. (A.1) can be approximated as zero.

One way to prove that I can neglect the left side of Eq. (A.1) is to non-dimensionalize it according to the following scaling laws:

$$t = T\,t' \qquad \text{(A.3)}$$

$$x = L\,x' \qquad \text{(A.4)}$$

$$z = H\,z' \qquad \text{(A.5)}$$

$$u = Uu' \tag{A.6}$$

$$w = U(H/L)w' \tag{A.7}$$

$$p = P\,p' \tag{A.8}$$

Where, *T*, *L*, *H*, *U*, and *P* are the characteristics time, length, height, axial velocity, and pressure respectively.

After normalizing the momentum equation, and only considering motion in the axial direction, I arrive at:

$$\frac{U}{T}\frac{\partial u'}{\partial t'} + \frac{U^2}{L}\left(u'\frac{\partial u'}{\partial x'} + w'\frac{\partial u'}{\partial z'}\right) = -\frac{P}{\rho L}\frac{\partial p'}{\partial x'} + \frac{\mu U}{\rho H^2}\left(\frac{H^2}{L^2}\frac{\partial^2 u'}{\partial x'^2} + \frac{\partial^2 w'}{\partial z'^2}\right) + g\cdot\hat{i} \tag{A.8}$$

This equation can be re-written as:

$$\frac{\rho H^2}{\mu T}\frac{\partial u'}{\partial t'} + \frac{\rho UH}{\mu}\frac{H}{L}\left(u'\frac{\partial u'}{\partial x'} + w'\frac{\partial u'}{\partial z'}\right) = -\frac{H^2 P}{\mu UL}\frac{\partial p'}{\partial x'} + \left(\frac{H^2}{L^2}\frac{\partial^2 u'}{\partial x'^2} + \frac{\partial^2 w'}{\partial z'^2}\right) + \frac{\rho H^2}{\mu U}g\cdot\hat{i} \tag{A.9}$$

Recognizing that I am analyzing a thin-film, especially as time progresses, and several other characteristics that are relevant to the nature of the problem discussed in this dissertation, I arrive at the following three assumptions:

$$H/L << 1 \tag{A.11}$$

$$\frac{\rho UH}{\mu} = O(1) \text{ Or Smaller} \tag{A.12}$$

$$\frac{\rho H^2}{\mu T} << 1 \tag{A.13}$$

Eq. (A.11) is valid for all phases of the simulation, but becomes more valid as the free surface becomes smoother. For the application presented in this document, the typical value for Eq. (A.13) is about 0.002, and as time progresses the numerator decreases as the denominator grows.

After omitting terms on the order of H/L and $\rho H^2/\mu T$, and converting Eq. (A.9) back into dimensional form, the entire left side of the equation of motion can be set to zero.

These are the rules behind the lubrication approximation and are the restrictions of the simulation presented in this document. For example, running the presented simulations for a different liquid like water would completely undermine the condition set in Eq. (A.13), and its values could become much greater than unity.

Appendix B - Additional Experiments

In order to investigate how the process of making the gel would impact the final product, and its spreading and rheological properties, I made 3 batches of a 2.7% HEC gel. Each batch underwent rheological and spreading testing, in triplicate.

The procedure for making each batch was identical, and is described in Chapter 2. The protocols for rheological and spreading experiments are outlined in Chapter 2 and 3, respectively. Table B1 shows power-law parameter values obtained by fitting to the average rheological data, for each of 3 batches of 2.7% HEC gels. Rheology data is fit to the power-law constitutive equation using the Nelder-Mead simplex search method, as described in Chapter 2.

2.7% HEC BATCH	***m* (Ps^{n-1})**	***n***	**R^2**
1	343.3896	0.5543	0.9793
2	336.2361	0.5736	0.9796
3	304.7081	0.5719	0.9807
mean ± S.D.	328.11±20.58	0.5666±0.0110	---

Table B1. Power-law parameters for 2.7% HEC gels. Note: $m \equiv$ consistency index; $n \equiv$ shear-thinning index; R^2 represents the goodness of fit.

The high standard deviation of the consistency index between different batches is due to two general sources of error: (1) error associated with making the gel, and (2) error associated with testing the gel. When making the gel, there are several steps in the protocol that could contribute to inconsistencies in overall rheology between batches. The most impactful is the amount of water that is evaporated during the mixing process, and the amount of solute (HEC) that does not get mixed into the solvent (water). After pouring HEC into the stirring water, some is always left on the delivery paper and unintentionally poured on the stirring rod. During rheology testing, the gel must be trimmed off the testing geometry, which is a source of error

between tests. Mixing HEC on a pharmaceutical assembly line could eliminate most of these errors, which I suspect would noticeably lower the deviation between batches.

The differences in spreading physiognomies seen between batches are generally on the order of millimeters. Table B2 shows the changes in length, width, and height over 180 seconds of spreading, for 3 batches of 2.7% HEC gels.

2.7% HEC BATCH	**ΔL**	**ΔW**	**Δh**
1	38.07±0.77 *mm* (2.02%)	4.44±0.57 *mm* (12.84%)	3.18±0.30*mm* (9.43%)
2	41.89±2.59 *mm* (6.18%)	4.22±1.00 *mm* (23.70%)	3.47±0.27*mm* (7.78%)
3	46.29±2.42 *mm* (5.23%)	4.21±1.38 *mm* (32.78%)	4.12±0.63*mm* (15.29%)

Table B2. Spreading data for 3 batches of 2.7% HEC gels. ΔL and ΔW represent total axial and lateral spreading, in 180 sec, respectively. Δh represents the change in height. **Note: Each cell presents the: Mean ± Standard Deviation (Coefficient of Variation).**

The average values, expected of a typical 2.7% HEC gel, of the spreading physiognomies are found using Eq. (B.1) and (B.2), where $w_i = 1/\sigma^2$.

$$M = \frac{\sum w_i M_i}{\sum w_i} \tag{B.1}$$

$$S.D. = \frac{1}{\sqrt{\sum w_i}} \tag{B.2}$$

Therefore, the weighted averages are:

- ΔL_{avg} = 39.05±0.71 *mm*
- ΔW_{avg}= 4.37±0.47 *mm*
- Δh_{avg} = 3.41±0.19 *mm*

The weighted values show less variation than in Table B2, and are the best estimate of 2.7% HEC spreading behavior, found experimentally at a 30° incline.

Bibliography

1. Silver Spring, M., *The Microbicide Development Strategy*, 2006, MDS Working Groups Alliance for Microbicide Development.
2. Kieweg, S.L., A.R. Geonnotti, and D.F. Katz, *Gravity-induced coating flows of vaginal gel formulations: in vitro experimental analysis.* J Pharm Sci, 2004. **93**(12): p. 2941-52.
3. Kieweg, S.L., *Mechanical analysis of vaginal gels intended for microbicide application*, in *Department of Biomedical Engineering*2005, Duke University.
4. Kieweg, S.L., T.P. Witelski, and D.F. Katz., *Free-surface coating flows of non-Newtonian vaginal gels: numerical and experimental simulations of gravity-induced flow.*, in *ASME Summer Bioengineering Conference*2006: Amelia Island, FL.
5. UNAIDS, *AIDS epidemic update: December 2009*, 2009, WHO Library Cataloguing-in-Publication Data.
6. Lederman, M.M., R.E. Offord, and O. Hartley, *Microbicides and other topical strategies to prevent vaginal transmission of HIV.* Nat Rev Immunol, 2006. **6**(5): p. 371-82.
7. Stone, A., *Microbicides: a new approach to preventing HIV and other sexually transmitted infections.* Nat Rev Drug Discov, 2002. **1**(12): p. 977-85.
8. Nuttall, J., et al., *The future of HIV prevention: prospects for an effective anti-HIV microbicide.* Infect Dis Clin North Am, 2007. **21**(1): p. 219-39.
9. Cutler, B. and J. Justman, *Vaginal microbicides and the prevention of HIV transmission.* Lancet Infect Dis, 2008. **8**(11): p. 685-97.
10. Shattock, R. and S. Solomon, *Microbicides--aids to safer sex.* Lancet, 2004. **363**(9414): p. 1002-3.
11. das Neves, J., et al., *Vaginal microbicides: the importance of effective distribution, retention and coating of the mucosa.* AIDS, 2008. **22**(7): p. 908-9.
12. Pretorius, E.S., et al., *Magnetic resonance imaging to determine the distribution of a vaginal gel: before, during, and after both simulated and real intercourse.* Contraception, 2002. **66**(6): p. 443-51.
13. Barnhart, K.T., et al., *Spermicides containing nonoxynol-9 placed in the vaginal canal migrate to the upper female reproductive tract.* Fertility and Sterility, 2001. **76**(3): p. O45.
14. Ramjee, G., et al., *Microbicides 2006 conference.* AIDS Res Ther, 2006. **3**: p. 25.
15. Ramjee, G., A. Kamali, and S. McCormack, *The last decade of microbicide clinical trials in Africa: from hypothesis to facts.* AIDS, 2010. **24 Suppl 4**: p. S40-9.
16. Tien, D., et al., *In vitro and in vivo characterization of a potential universal placebo designed for use in vaginal microbicide clinical trials.* AIDS Res Hum Retroviruses, 2005. **21**(10): p. 845-53.
17. Osullivan, A.C., *Cellulose: the structure slowly unravels.* Cellulose, 1997. **4**(3): p. 173-207.
18. Day, M. and R.C. Fay, *Chemistry*1995, Englewood Cliffs: Prentice-Hall Inc.
19. Evmenenko, G., et al., *Structural reorganization in films of cellulose derivatives in the presence of colloidal particles.* Polymer, 2004. **45**(18): p. 6269-6273.
20. Myers, T.G., *Application of non-Newtonian models to thin film flow.* Physical Review E, 2005. **72**(6).

21. Andrews, G.P. and D.S. Jones, *Rheological characterization of bioadhesive binary polymeric systems designed as platforms for drug delivery implants.* Biomacromolecules, 2006. **7**(3): p. 899-906.
22. Andrews, G.P., et al., *Characterization of the Rheological, Mucoadhesive, and Drug Release Properties of Highly Structured Gel Platforms for Intravaginal Drug Delivery.* Biomacromolecules, 2009. **10**(9): p. 2427-2435.
23. Andrews, G.P., S.P. Gorman, and D.S. Jones, *Rheological characterisation of primary and binary interactive bioadhesive gels composed of cellulose derivatives designed as ophthalmic viscosurgical devices.* Biomaterials, 2005. **26**(5): p. 571-580.
24. Bird, B.R., R.C. Armstrong, and O. Hassager, *Dynamics of Polymeric Liquids*. 2 ed. Vol. 1. 1987: A Weiley-Interscience Publication.
25. Matsuhis, S. and R.B. Bird, *Analytical and numerical solutions for laminar flow of non-Newtonian Ellis fluid.* AICHE Journal, 1965. **11**(4): p. 588.
26. Kieweg, S.L. and D.F. Katz, *Squeezing flows of vaginal gel formulations relevant to microbicide drug delivery.* Journal of Biomechanical Engineering-Transactions of the ASME, 2006. **128**(4): p. 540-553.
27. Kvalseth, T.O., *Cautionary note about R2.* American Statistician, 1985. **39**(4): p. 279-285.
28. Balmforth, N.J., et al., *Viscoplastic flow over an inclined surface.* Journal of Non-Newtonian Fluid Mechanics, 2006. **139**(1-2): p. 103-127.
29. Balmforth, N., et al., *Visco-plastic models of isothermal lava domes.* Journal of Fluid Mechanics, 2000. **403**: p. 37-65.
30. Schwartz, L.W. and R.R. Eley, *Flow of architectural coatings on complex surfaces; theory and experiment.* Journal of Engineering Mathematics, 2002. **43**(2-4): p. 153-171.
31. Diez, J., et al., *Unstable spreading of a fluid filament on a vertical plane: Experiments and simulations.* Physica D: Nonlinear Phenomena, 2005. **209**(1-4): p. 49-61.
32. Gonzalez, A.G., et al., *Spreading of a thin two-dimensional strip of fluid on a vertical plane: Experiments and modeling.* Physical Review E, 2004. **70**(2): p. -.
33. Dukler, A.E. and O.P. Bergelin, *Characteristics of flow - in falling liquid films.* Chemical Engineering Progress, 1952. **48**(11): p. 557-563.
34. Ambrosini, W., N. Forgione, and F. Oriolo, *Statistical characteristics of a water film falling down a flat plate at different inclinations and temperatures.* International Journal of Multiphase Flow, 2002. **28**(9): p. 1521-1540.
35. Roy, R.P. and S. Jain, *A study of thin water film flow down an inclined plate without and with countercurrent air flow.* Experiments in Fluids, 1989. **7**(5): p. 318-328.
36. Liu, J. and J.P. Gollub, *Solitary wave dynamics of film flows.* Physics of Fluids, 1994. **6**(5): p. 1702-1712.
37. Liu, J., J.D. Paul, and J.P. Gollub, *Measurements of the primary instabilities of film flows.* Journal of Fluid Mechanics, 1993. **250**: p. 69-101.
38. Liu, J., J.B. Schneider, and J.P. Gollub, *3-Dimensional instabilities of film flows.* Physics of Fluids, 1995. **7**(1): p. 55-67.
39. Zaitsev, D.V., O.A. Kabov, and A.R. Evseev, *Measurement of locally heated liquid film thickness by a double-fiber optical probe.* Experiments in Fluids, 2003. **34**(6): p. 748-754.

40. Lel, V., et al., *Local thickness and wave velocity measurement of wavy films with a chromatic confocal imaging method and a fluorescence intensity technique.* Experiments in Fluids, 2005. **39**(5): p. 856-864.
41. Zhou, D.W., T. Gambaryan-Roisman, and P. Stephan, *Measurement of water falling film thickness to flat plate using confocal chromatic sensoring technique.* Experimental Thermal and Fluid Science, 2009. **33**(2): p. 273-283.
42. Thomas, L., et al., *Measurement of the slope of an unsteady liquid surface along a line by an anamorphic schlieren system.* Measurement Science & Technology, 1996. **7**(8): p. 1134-1139.
43. Lan, H., et al., *Developing Laminar Gravity-Driven Thin Liquid Film Flow Down an Inclined Plane.* Journal of Fluids Engineering, 2010. **132**(8): p. 081301.
44. Johnson, M.F.G., R.A. Schluter, and S.G. Bankoff, *Fluorescent imaging system for global measurement of liquid film thickness and dynamic contact angle in free surface flows.* Review of Scientific Instruments, 1997. **68**(11): p. 4097-4102.
45. Johnson, M.F.G., et al., *Experimental study of rivulet formation on an inclined plate by fluorescent imaging.* Journal of Fluid Mechanics, 1999. **394**: p. 339-354.
46. Cochard, S. and C. Ancey, *Tracking the free surface of time-dependent flows: image processing for the dam-break problem.* Experiments in Fluids, 2008. **44**(1): p. 59-71.
47. Cochard, S. and C. Ancey, *Experimental investigation of the spreading of viscoplastic fluids on inclined planes.* Journal of Non-Newtonian Fluid Mechanics, 2009. **158**(1-3): p. 73-84.
48. Piau, J.M. and K. Debiane, *Consistometers rheometry of power-law viscous fluids.* Journal of Non-Newtonian Fluid Mechanics, 2005. **127**(2-3): p. 213-224.
49. Witelski, T.P. and M. Bowen, *ADI schemes for higher-order nonlinear diffusion equations.* Applied Numerical Mathematics, 2003. **45**(2-3): p. 331-351.
50. Acheson, D.J., *Elementary fluid dynamics*1990: Oxford University Press. 397.
51. Ashmore, J., et al., *Coating flows of non-Newtonian fluids: weakly and strongly elastic limits.* Journal of Engineering Mathematics, 2008. **60**(1): p. 17-41.
52. Gratton, J., F. Minotti, and S.M. Mahajan, *Theory of creeping gravity currents of a non-Newtonian liquid.* Physical Review E, 1999. **60**(6): p. 6960-6967.
53. Craster, R.V. and O.K. Matar, *Dynamics and stability of thin liquid films.* Reviews of Modern Physics, 2009. **81**(3): p. 1131-1198.
54. Ancey, C., *Plasticity and geophysical flows: A review.* Journal of Non-Newtonian Fluid Mechanics, 2007. **142**(1-3): p. 4-35.
55. Huppert, H.E., *Flow and instability of a viscous current down a slope.* Nature, 1982. **300**(5891): p. 427-429.
56. Kondic, L. and J. Diez, *Pattern formation in the flow of thin films down an incline: Constant flux configuration.* Physics of Fluids, 2001. **13**(11): p. 3168-3184.
57. Kondic, L. and J. Diez, *Flow of thin films on patterned surfaces: Controlling the instability.* Physical Review E, 2002. **65**(4).
58. Kondic, L., *Instabilities in gravity driven flow of thin fluid films.* Siam Review, 2003. **45**(1): p. 95-115.
59. Fulton, S.R., P.E. Ciesielski, and W.H. Schubert, *Multigrid methods for elliptic problems - A review.* Monthly Weather Review, 1986. **114**(5): p. 943-959.

60. Dendy, J.E., *Alternating direction methods for nonlinear time-dependent problems.* Siam Journal on Numerical Analysis, 1977. **14**(2): p. 313-326.
61. Harlow, F.H. and J.E. Welch, *Numerical calculation of time-dependent viscous incompressible flow of fluid with free surface.* Physics of Fluids, 1965. **8**(12): p. 2182-&.
62. Diez, J.A. and L. Kondic, *Computing three-dimensional thin film flows including contact lines.* Journal of Computational Physics, 2002. **183**(1): p. 274-306.
63. D.F., M.K.W.a.M., *Numerical Solution of Partial Differential Equation*. 2 ed2005: Cambridge University Press.
64. Chapra, S.C. and R.P. Canale, *Numerical Methods for Engineers*. 5th ed 2006: McGraw Hill.
65. Bird, B.R., G.G. Dai, and B.J. Yarusso, *The rheology and flow of viscoplastic materials.* Reviews in Chemical Engineering, 1982. **1**(1): p. 1-70.
66. Mei, C.C. and M. Yuhi, *Slow dow of a Bingham fluid in a shallow channel of finite width.* Journal of Fluid Mechanics, 2001. **431**: p. 135-159.
67. Balmforth, N.J. and R.V. Craster, *A consistent thin-layer theory for Bingham plastics.* Journal of Non-Newtonian Fluid Mechanics, 1999. **84**(1): p. 65-81.
68. Balmforth, N.J., R.V. Craster, and R. Sassi, *Shallow viscoplastic flow on an inclined plane.* Journal of Fluid Mechanics, 2002. **470**: p. 1-29.
69. Liu, K.F. and C.C. Mei, *Slow spreading of a sheet of Bingham fluid on an incline plane.* Journal of Fluid Mechanics, 1989. **207**: p. 505-529.
70. Liu, K.F. and C.C. Mei, *Approximate equations for the slow spreading of a thin sheet of Bingham plastic fluid.* Physics of Fluids a-Fluid Dynamics, 1990. **2**(1): p. 30-36.
71. Sutalo, I.D., A. Bui, and M. Rudman, *The flow of non-Newtonian fluids down inclines.* Journal of Non-Newtonian Fluid Mechanics, 2006. **136**(1): p. 64-75.
72. Huang, X. and M.H. Garcia, *A Herschel-Bulkley model for mud flow down a slope.* Journal of Fluid Mechanics, 1998. **374**: p. 305-333.
73. Perazzo, C.A. and J. Gratton, *Steady and traveling flows of a power-law liquid over an incline.* Journal of Non-Newtonian Fluid Mechanics, 2004. **118**(1): p. 57-64.
74. Perazzo, C.A. and J. Gratton, *Thin film of non-Newtonian fluid on an incline.* Physical Review E, 2003. **67**(1).
75. Nguetchue, S.N.N. and E. Momoniat, *Axisymmetric spreading of a thin power-law fluid under gravity on a horizontal plane.* Nonlinear Dynamics, 2008. **52**(4): p. 361-366.
76. Gorodtsov, V.A., *Spreading of a film of nonlinearly viscous liquid over a horizontal smooth solid surface* Journal of Engineering Physics and Thermophysics, 1988. **57**(2): p. 879-884.
77. Pascal, H., *Gravity flow of a non-Newtonian fluid sheet on an inclined plane.* International Journal of Engineering Science, 1991. **29**(10): p. 1307-1313.
78. Haeri, S. and S.H. Hashemabadi, *Three dimensional CFD simulation and experimental study of power law fluid spreading on inclined plates.* International Communications in Heat and Mass Transfer, 2008. **35**(8): p. 1041-1047.
79. Spiers, R.P., C.V. Subbaraman, and W.L. Wilkinson, *Free coating of non-Newtonian liquids onto a vertical surface.* Chemical Engineering Science, 1975. **30**(4): p. 379-395.
80. Weidner, D.E. and L.W. Schwartz, *Contact-line motion of shear-thinning liquids.* Physics of Fluids, 1994. **6**(11): p. 3535-3538.

81. Steller, R.T., *Generalized slit flow of an Ellis fluid.* Polymer Engineering and Science, 2001. **41**(11): p. 1859-1870.
82. Dembo, R.S., S.C. Eisenstat, and T. Steihaug, *Inexact Newton Methods.* SIAM Journal on Numerical Analysis, 1982. **19**(2): p. 400-408.
83. Richard, B., et al., *Templates for the Solution of Linear Systems: Building Blocks for Iterative Methods, 2nd Edition*. 2 ed1994: SIAM.
84. Nachtigal, N.M., S.C. Reddy, and L.N. Trefethen, *How fast are nonsymmetric matrix iterations.* SIAM Journal on Matrix Analysis and Applications, 1992. **13**(3): p. 778-795.
85. Dussan, E.B. and S.H. Davis, *Stability in systems with moving contact lines.* Journal of Fluid Mechanics, 1986. **173**: p. 115-130.
86. Wang, X.D., X.F. Peng, and D.Z. Lee, *Dynamic wetting and stress singularity on contact line.* Science in China Series E-Technological Sciences, 2003. **46**(4): p. 407-417.
87. Bertozzi, A.L., *The Mathematics of Moving Contact Lines in Thin Liquid Films.* Notices of the American Mathematical Society, 1998. **45**(6).
88. Macosko, C.W., *Rheology: principles, measurements, and applications*1994: WILEY-VCH.
89. Gorodtsov, V.A., *Spreading of a film of nonlinearly viscous liquid over a horizontal smooth solid surface* Journal of Engineering Physics and Thermophysics, 1990. **57**(2): p. 879-884.
90. Betelu, S.I. and M.A. Fontelos, *Capillarity driven spreading of power-law fluids.* Applied Mathematics Letters, 2003. **16**(8): p. 1315-1320.
91. Coussot, P. and S. Proust, *Slow, unconfined spreading of a mudflow.* Journal of Geophysical Research-Solid Earth, 1996. **101**(B11): p. 25217-25229.
92. Wilson, S.D.R. and S.L. Burgess, *The steady, spreading flow of a rivulet of mud.* Journal of Non-Newtonian Fluid Mechanics, 1998. **79**(1): p. 77-85.
93. Yin, X.Y. and S. Kumar, *Lubrication flow between a cavity and a flexible wall.* Physics of Fluids, 2005. **17**(6).
94. Barrat, J.L. and L. Bocquet, *Large slip effect at a nonwetting fluid-solid interface.* Physical Review Letters, 1999. **82**(23): p. 4671-4674.
95. Baudry, J., et al., *Experimental Evidence for a Large Slip Effect at a Nonwetting Fluid−Solid Interface.* Langmuir, 2001. **17**(17): p. 5232-5236.
96. Israelachvili, J.N., *Intermolecular and Surface Forces*1985-2004: Academic Press.
97. Geonnotti, A.R., J.J. Peters, and D.F. Katz, *Erosion of microbicide formulation coating layers: Effects of contact and shearing with vaginal fluid or semen.* Journal of Pharmaceutical Sciences, 2005. **94**(8): p. 1705-1712.